NASA Contractor Report 3630

Jet Array Impingement Flow Distributions and Heat Transfer Characteristics

Effects of Initial Crossflow and Nonuniform Array Geometry

L. W. Florschuetz, D. E. Metzger,
C. C. Su, Y. Isoda, and H. H. Tseng

GRANT NSG-3075
NOVEMBER 1982

NASA Contractor Report 3630

Jet Array Impingement Flow Distributions and Heat Transfer Characteristics

Effects of Initial Crossflow and Nonuniform Array Geometry

L. W. Florschuetz, D. E. Metzger,
C. C. Su, Y. Isoda, and H. H. Tseng
Arizona State University
Tempe, Arizona

Prepared for
Lewis Research Center
under Grant NSG-3075

NASA
National Aeronautics
and Space Administration

Scientific and Technical
Information Branch

1982

CONTENTS

CONTENTS (Cont'd)

NOMENCLATURE

A_o = total jet hole area

A_o^* = ratio of jet hole area to opposing impingement surface area (open area ratio), $\pi/[4(x_n/d)(y_n/d)]$

b = local thickness of jet plate at jet hole location

B = dimensionless quantity defined following Eq. (4.6)

C = dimensionless quantity defined following Eq. (4.6)

C_D = jet plate discharge coefficient

c_p = constant pressure specific heat

d = jet hole diameter

D_h = hydraulic diameter

E_k, F_k = coefficients defined following Eq. (9.4)

f = friction coefficient defined as $2\tau_w\rho/G_c^2$

G_c = crossflow mass velocity based on channel cross-sectional area

$\tilde{G}_c$ = G_c normalized by channel exit mass velocity, $G_c/[(m_c + m_j)/(z \cdot w)]$

G_j = jet mass velocity based on jet hole area

G_j^* = superficial jet mass velocity based on jet plate area

h = heat transfer coefficient at impingement surface defined by Eq. (5.1)

L = streamwise length of jet plate and impingement surface (Figs. 3.1, 4.5, and 8.1)

L_e = initial crossflow development (entrance) length upstream of jet array

L_k = streamwise length of region k of nonuniform jet array (Fig. 8.1)

$\bar{L}_k$ = L_k/L

m_c = initial crossflow rate

m_j = total jet flow rate

M = initial crossflow-to-total jet flow ratio, m_c/m_j

N_c = number of spanwise rows of holes in streamwise direction

N_s = number of jet holes across span of heat transfer test surface

N_s' = number of jet holes across span of channel

Nu = Nusselt number, hd/k

P = channel pressure

P_o = jet plenum pressure

q = heat flux at impingement surface

Q_n = heat rate at surface of test plate segment n in initial crossflow channel

R = ideal gas constant

Re_c = crossflow (channel) Reynolds number, $G_c(2z)/\mu$

Re_j = jet Reynolds number, $G_j d/\mu$

Re_j^* = superficial jet Reynolds number, $G_j^* d/\mu$

St = Stanton number, $h/c_p\bar{G}_j$

T_{aw} = adiabatic wall temperature

T_c = characteristic temperature of initial crossflow (pp. 53-55 and 63-64)

T_j = characteristic temperature of jet flow (pp. 53-55)

T_f = characteristic injection temperature for film cooling

T_m = characteristic mainstream temperature for film cooling

T_o = jet plenum air temperature

T_o^c = initial crossflow plenum air temperature

T_s = heat transfer surface temperature

w = width (span) of channel

x = streamwise location along jet plate or impingement surface (Figs. 3.1., 4.5, and 8.1)

$\tilde{x}$ = x/L

$\tilde{x}'$ = $\tilde{x} - (1/2)(x_n/L)$

x_n = streamwise jet hole spacing

y_n = spanwise jet hole spacing

z = channel height (jet exit plane-to-impingement surface spacing)

Greek

η = dimensionless adiabatic wall temperature defined by Eq. (5.3) for jet array impingement with initial crossflow; and by Eq. (5.2) for film cooling.

ξ = function defined by Eq. (4.2)

γ = ratio of specific heats

μ = dynamic viscosity

ρ = fluid density

τ_w = channel wall shear stress

Subscripts and Superscripts

bp = refers to ''break point'' value of G_c/G_j (p. 25)

k,1,2 = refer to uniform geometry region of nonuniform array; k = 1 for upstream region; k = 2 for downstream region

$(\overline{\ })$ = overbar refers to mean value over jet plate

$(\ )^n$ = superscript n refers to value at n^{th} spanwise row of holes ($n = 1,2,\ldots,N_c$)

NOMENCLATURE

A_o = total jet hole area

A_o^* = ratio of jet hole area to opposing impingement surface area (open area ratio), $\pi/[4(x_n/d)(y_n/d)]$

b = local thickness of jet plate at jet hole location

B = dimensionless quantity defined following Eq. (4.6)

C = dimensionless quantity defined following Eq. (4.6)

C_D = jet plate discharge coefficient

c_p = constant pressure specific heat

d = jet hole diameter

D_h = hydraulic diameter

E_k, F_k = coefficients defined following Eq. (9.4)

f = friction coefficient defined as $2\tau_w\rho/G_c^2$

G_c = crossflow mass velocity based on channel cross-sectional area

$\tilde{G}_c$ = G_c normalized by channel exit mass velocity, $G_c/[(m_c + m_j)/(z \cdot w)]$

G_j = jet mass velocity based on jet hole area

G_j^* = superficial jet mass velocity based on jet plate area

h = heat transfer coefficient at impingement surface defined by Eq. (5.1)

L = streamwise length of jet plate and impingement surface (Figs. 3.1, 4.5, and 8.1)

L_e = initial crossflow development (entrance) length upstream of jet array

L_k = streamwise length of region k of nonuniform jet array (Fig. 8.1)

$\tilde{L}_k$ = L_k/L

m_c = initial crossflow rate

m_j = total jet flow rate

M = initial crossflow-to-total jet flow ratio, m_c/m_j

N_c = number of spanwise rows of holes in streamwise direction

N_s = number of jet holes across span of heat transfer test surface

N_s' = number of jet holes across span of channel

Nu = Nusselt number, hd/k

P = channel pressure

P_o = jet plenum pressure

q = heat flux at impingement surface

Q_n = heat rate at surface of test plate segment n in initial crossflow channel

R = ideal gas constant

Re_c = crossflow (channel) Reynolds number, $G_c(2z)/\mu$

Re_j = jet Reynolds number, $G_j d/\mu$

Re_j^* = superficial jet Reynolds number, $G_j^* d/\mu$

St = Stanton number, $h/c_p\bar{G}_j$

T_{aw} = adiabatic wall temperature

T_c = characteristic temperature of initial crossflow (pp. 53-55 and 63-64)

T_j = characteristic temperature of jet flow (pp. 53-55)

T_f = characteristic injection temperature for film cooling

T_m = characteristic mainstream temperature for film cooling

T_o = jet plenum air temperature

T_o^c = initial crossflow plenum air temperature

T_s = heat transfer surface temperature

w = width (span) of channel

x = streamwise location along jet plate or impingement surface (Figs. 3.1., 4.5, and 8.1)

$\tilde{x}$ = x/L

$\tilde{x}'$ = $\tilde{x} - (1/2)(x_n/L)$

x_n = streamwise jet hole spacing

y_n = spanwise jet hole spacing

z = channel height (jet exit plane-to-impingement surface spacing)

Greek

η = dimensionless adiabatic wall temperature defined by Eq. (5.3) for jet array impingement with initial crossflow; and by Eq. (5.2) for film cooling.

ξ = function defined by Eq. (4.2)

γ = ratio of specific heats

μ = dynamic viscosity

ρ = fluid density

τ_w = channel wall shear stress

Subscripts and Superscripts

bp = refers to ''break point'' value of G_c/G_j (p. 25)

k,1,2 = refer to uniform geometry region of nonuniform array; k = 1 for upstream region; k = 2 for downstream region

$(\overline{\ })$ = overbar refers to mean value over jet plate

$(\ )^n$ = superscript n refers to value at n^{th} spanwise row of holes ($n = 1,2,\ldots,N_c$)

SUMMARY

The work reported herein is divided into two major parts, each of which represents an extension of work completed in earlier phases of an overall investigation. The overall investigation was directed toward the determination of flow distributions and heat transfer characteristics for two-dimensional arrays of circular air jets impinging on a surface parallel to the jet orifice plate. The configurations considered were intended to model those of interest in current and contemplated gas turbine airfoil midchord cooling applications. The geometry of the airfoil applications considered dictates that all of the jet flow, after impingement, exit in the chordwise (i.e., streamwise) direction toward the trailing edge. The accumulated flow from upstream jet rows in the array acts as a crossflow to downstream rows. In some cooling schemes an initial crossflow arising from air used to cool the leading edge approaches the midchord jet array. The temperature of this initial crossflow air can be several hundred degrees higher than the cooling air introduced to the jet array.

The early work in the study dealt with arrays of uniform geometries not subject to an initial crossflow. These arrays had streamwise hole spacings of 5, 10, and 15 hole diameters, spanwise hole spacings of 4, 6, and 8 diameters, and jet exit plane-to-impingement surface spacings (channel heights) of 1, 2, and 3 hole diameters, with 10 spanwise rows of holes. Spanwise averaged heat transfer coefficients, resolved in the streamwise direction, were measured and correlated in terms of individual spanwise row jet and crossflow velocities, and in terms of the geometric parameters. These results were reported in detail in two previously published NASA reports.

In Part I of the present report, experimental results for the effects of an initial crossflow on both flow distributions and heat transfer characteristics for a number of the prior uniform array geometries are presented. Heat transfer coefficients and adiabatic wall temperatures resolved to one streamwise hole spacing were determined for ratios of the initial crossflow-to-total jet flow rate ranging from zero to unity. The adiabatic wall temperatures depend on the relative flow rates and relative characteristic temperatures of both the jet air and the initial crossflow air, as well as on the geometric

parameters. Both Nusselt number profiles and dimensionless adiabatic wall temperature (''effectiveness'') profiles are presented and discussed as a function of the flow and geometric parameters. For some conditions ''effectiveness'' profiles cover nearly the entire range between zero and unity, and Nusselt numbers at upstream rows are reduced significantly compared with zero initial crossflow values, even for initial crossflow-to-total jet flow ratios as small as 0.2. Special test results which show a significant reduction of jet orifice discharge coefficients owing to the effect of a confined crossflow are presented, along with a flow distribution model which incorporates those effects.

In Part II, experimental results for the effects of nonuniform array geometries on flow distributions and heat transfer characteristics for noninitial crossflow configurations are presented. The nonuniform arrays are comprised of two different regions each of which has a uniform geometry. Either hole spacing or hole diameter has a different value in the two regions. The previously developed flow distribution model for uniform arrays is extended to nonuniform arrays and validated by comparison with the measured flow distributions. The validated flow distribution model is then employed to compare the nonuniform array streamwise resolved heat transfer coefficient data with the previously reported uniform array data and with the previously developed correlation based on the uniform array data. It was found that the uniform array results can, in general, serve as a satisfactory basis from which to predict heat transfer coefficients at individual rows of nonuniform arrays. However, significant differences were observed in some cases over the first one or two rows downstream of the geometric transition line of the nonuniform array. For practical purposes the ''entrance'' or ''adjustment'' length for a downstream region could be considered as requiring from zero to at most two jet rows, depending on the particular case.

1. INTRODUCTION

The cooling of gas turbine engine components has become established as an important aspect of turbine engine design. The most common cooling schemes involve the use of air cooling, where a portion of the compressor discharge is diverted around the combustor to be used directly as a heat exchange medium. In this way the temperatures and temperature gradients of components exposed to the hot gas stream can be reduced, thereby extending service life at a given performance level.

Modern high performance engines use 20 percent or more of the compressor discharge flow for cooling purposes. The design of such engines requires great care so that the performance improvement to be derived from operating at higher temperatures is not more than offset by the cycle and aerodynamic penalties associated with compressing and using the cooling air. In order to do rational and confident design, the designer must have access to detailed accurate information on the flow and heat transfer characteristics of cooling schemes in use or under consideration.

The most critical areas in the engine from the viewpoint of thermal exposure are the first-stage airfoils, both stator vanes and turbine blades. The stationary first stage vanes, situated immediately downstream of the burner experience the highest gas temperatures, including ''hot streaks'' of several hundred degrees above the mean temperature associated with combustor pattern nonuniformities. The first stage blades, although experiencing lower relative velocities and a rotational averaging of the combustor pattern, are subject to the additional complications and stresses of rotation.

For both these airfoil sets, the external heat load around the airfoil surface is very nonuniform. The situation depicted in Fig. 1.1 is typical. The leading edge region experiences very high external heat transfer coefficients. These decrease quickly but usually grow again in the midchord region, particularly on the suction side of the airfoil.

The large external heat loads require an internal cooling scheme with high heat transfer coefficients between the cooling air and inner surface of the airfoil. An impingement cooled arrangement is often the choice because of the high heat transfer coefficients possible and the capability of placing

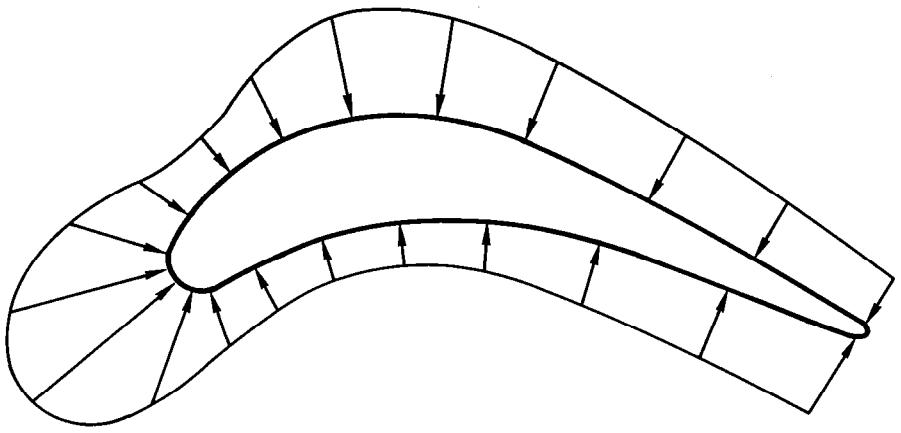

Fig. 1.1 Example of airfoil external heat load distribution.

jets in patterns dictated by the external thermal loading. This flexibility in jet placement can be advantageous not only in the chordwise direction, but also in the spanwise direction to reflect, for example, the burner pattern in the radial direction. Fig. 1.2 shows a typical midspan arrangement of jets. Note that the jets are constrained to exit in the chordwise direction, so the accumulated jet flow from upstream rows acts as a crossflow to downstream jet rows in the array. The drop-off in external load behind the leading edge eliminates the need for new cooling jets in this region and the leading edge coolant flows around to become a separate, or initial, crossflow to the midchord jet array. Alternate types of arrangements, for example Fig. 1.3, do not include the presence of an initial crossflow approaching the midchord jet array.

Despite the complications involved in fabricating airfoils with inserts to provide a jet plenum, the jet array remains an attractive cooling scheme for the midchord region for the reasons stated above. It is potentially a much better match to the spanwise and chordwise distribution of external heat loads than a multipass spanwise cooling flow arrangement. These multipass designs are often subject to either overcooling or undercooling problems in the turn regions at the airfoil root and tip.

Over the past several years, Arizona State University (ASU) has engaged in an extensive NASA sponsored study of the flow and heat transfer characteristics of two-dimensional jet arrays of the type depicted in the midchord

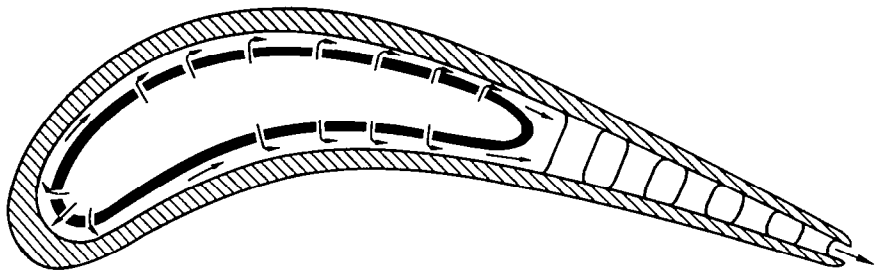

Fig. 1.2 Impingement cooled airfoil – midchord jet arrays subject to initial crossflow.

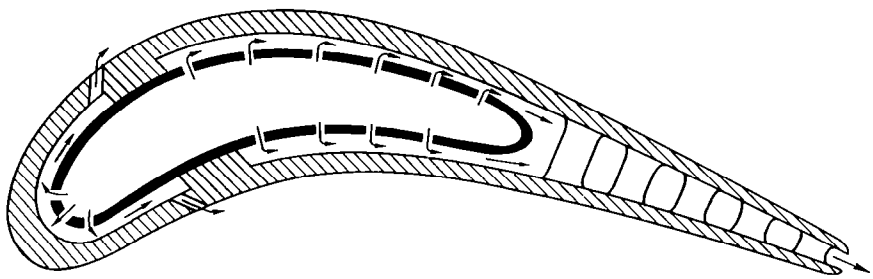

Fig. 1.3 Impingement cooled airfoil – midchord arrays not subject to initial crossflow.

regions of Figs. 1.2 and 1.3. The early work in this study was directed at modeling uniform arrays in cases where an initial crossflow is not present [1,2]. It should be recognized, however, that crossflow is always present downstream of the first row, whether or not a separate initial crossflow is imposed. The geometry of the airfoil application dictates that all of the jet flow will exit in the chordwise direction toward the trailing edge. This fact has stimulated much of the prior work on the effects of crossflow on confined jets, as typified by References [1–11].

More recently, the ASU study was expanded to consider the effects of initial crossflow, including the effect of an initial crossflow temperature which is elevated above the jet temperature. The latter condition is of considerable importance. The designer is often faced with an initial crossflow temperature which is substantially above the jet flow because of heat pickup in the leading edge region. Confident design can be achieved only if the designer knows the proper effective coolant temperatures and heat transfer coefficients to use in the region where the initial crossflow

penetrates into the jet array. To date, there is virtually no information in the literature to help the designer answer these questions.

Part I of this report presents the results of the ASU study intended to respond to this need. Experimental results are included for both flow distributions and heat transfer characteristics for uniform rectangular arrays of circular jet orifices with initial crossflow. These are intended to model the types of midchord cooling arrangements illustrated schematically in Fig. 1.2. For flow distributions emphasis is placed on the parametric effect of the initial crossflow rate. A theoretically based flow distribution model is also presented and compared with the results of the measurements. For heat transfer characteristics emphasis is placed on effects of both flow rate and temperature of the initial crossflow relative to the jet flow. Results are presented for a range of three primary geometric parameters: chordwise and spanwise jet hole spacings, and jet exit plane-to-impingement surface heights each considered relative to hole diameter.

One of the major results of the earlier work of the study was the determination of spanwise averaged, chordwise resolved heat transfer coefficients for uniformly spaced inline and staggered arrays in noninitial crossflow configurations modeling midchord arrays similar to those in Fig. 1.3 [1,8]. Nusselt numbers resolved to one chordwise hole spacing were correlated in terms of the individual spanwise row jet Reynolds number, the crossflow-to-jet mass velocity ratio, and the three primary geometric parameters noted above [2,11]. It is emphasized that all of these previously reported results in the noninitial crossflow configuration were restricted to cases where all aspects of the array geometry were uniform; i.e., uniform spanwise and chordwise hole spacings, hole diameters, and jet exit plane-to-impingement surface spacing. The correlation based on these results is, however, in a form which permits its direct application locally (i.e., row by row) to nonuniform array geometries, assuming only that the row-by-row jet flow distribution for the nonuniform array is known. It is also possible for the chordwise resolved Nusselt number data from the uniform array tests to be applied locally to nonuniform arrays. The use of nonuniform arrays provides the designer with additional flexibility in tailoring array geometry and corresponding coolant heat transfer coefficients to meet the specific local cooling requirements

imposed by the external hot gas flow. An important question which arises, therefore, is what confidence can the designer place in the local application to nonuniform arrays of uniform array heat transfer data and/or correlations based on such data?

Part II of this report addresses this question. Experimental results for both flow distributions and heat transfer coefficients for nonuniform arrays are presented. A previously developed flow distribution model for uniform arrays is extended to nonuniform arrays and validated by comparison with the experimental results. The validated flow distribution model is then employed to compare the nonuniform array heat transfer data with the previously reported uniform array data and correlation. The nonuniform arrays are composed of two uniform but different array patterns in the upstream and downstream regions of the array, respectively. In each nonuniform array only one geometric parameter takes a different value in each of the two regions, with all other parameters remaining constant. The parameters which were varied in this way were the hole spacings and the hole diameter. To facilitate comparisons the patterns used in each region matched previously tested uniform array patterns.

PART I - EFFECTS OF INITIAL CROSSFLOW

2. INTRODUCTORY REMARKS (PART I)

The jet arrays tested in the initial crossflow configuration had uniform, rectangular inline hole patterns with streamwise and spanwise hole spacings, expressed in jet hole diameters (x_n/d, y_n/d), of (5,4), (5,8), (10,4), and (10,8). Each array had ten spanwise rows of holes. The jet plate-to-impingement surface spacings (z/d) were 1, 2, and 3 hole diameters. The (5,4) configuration with z/d = 3 was also tested in a staggered hole pattern. Most tests were conducted with a nominal mean jet Reynolds number ($\overline{Re}_j$) of 10^4. The ratio of initial crossflow rate to total jet flow rate (m_c/m_j) was set at nominal values of 0.2, 0.5, and 1.0 for each geometry with a reference test at zero initial crossflow also included. The basic experimental facility as utilized for both flow distribution and heat transfer tests is described in Section 3.

A primary objective of Section 4 is to report and characterize the experimentally determined streamwise distributions of the jet flow, emphasizing the parametric effect of the initial crossflow. During the course of the tests significant inconsistencies arose for some cases with larger initial crossflows, when experimental mass balances failed to adequately check. By means of special tests it was found that these inconsistencies were due to crossflow effects on the discharge coefficients of the jet holes. Additional special tests were conducted to account for these effects. An additional objective of Section 4 is, therefore, to report experimental results for the effect of a confined crossflow on the discharge coefficients of jet orifices. A final objective is to present a relatively simple predictive model for the flow distributions, which, in its general form, includes effects of initial crossflow, variable discharge coefficients, and crossflow channel wall shear. Predictions based on the model are compared with the experimentally determined flow distributions.

Section 5 deals with the heat transfer characteristics for the jet arrays with an initial crossflow. Since the characteristic initial crossflow temperature may differ from the characteristic jet temperature, the problem is introduced from the perspective of a three-temperature problem, the most well-known example of which is film cooling. Spanwise averaged heat transfer

coefficients and adiabatic wall temperatures at the impingement surface, resolved to one streamwise hole spacing in the streamwise direction, were experimentally determined. The adiabatic wall temperatures depend on the relative flow rates and the characteristic temperatures of the jet air and the initial crossflow air, as well as on the geometric parameters. Both Nusselt number profiles and dimensionless adiabatic wall temperature (''effectiveness values'') profiles are presented and discussed as a function of the flow and geometric parameters, in particular, the initial crossflow-to-total jet flow ratio and the corresponding jet flow distributions presented in Section 4.

Part I closes with concluding remarks presented in Section 6.

3. INITIAL CROSSFLOW EXPERIMENTAL FACILITY

The basic test model geometry and nomenclature are shown schematically in Fig. 3.1. The flow region of primary interest is that bounded by the jet exit plane and the impingement surface. The length (L) of this region is considered to extend from one-half a streamwise hole spacing ($x_n/2$) upstream of the first spanwise row of holes to the same distance downstream of the last row. The total crossflow rate approaching a given row is equivalent to the initial crossflow rate (m_c) combined with the total jet flow introduced upstream of that row.

The basic experimental facility was that originally used for a comprehensive series of noninitial crossflow tests [1,2], but set up in a modified form suitable for conducting tests with initial crossflow. The original facility was designed for conducting heat transfer tests but was also utilized for measurement of jet flow distributions. A complete description of the original facility may be found in [1]. Here a description of the facility in the initial crossflow configuration will be given. For the convenience of the reader certain basic features previously described in detail [1], will also be reviewed.

A cross-sectional view of the arrangement is shown in Fig. 3.2. There are two plenum chambers, each with two sections of porous plenum packing supported by screens, supplied individually with dried and filtered laboratory compressed air, one for introducing air to the main jet plate, and one for introducing the initial crossflow air to the channel. An electric resistance heater (not shown) in the line immediately upstream of the initial crossflow plenum permits independent control of the initial crossflow air temperature at levels above the jet plenum air temperatures. The initial crossflow was introduced to the channel through two spanwise rows of jet holes. The main jet plates, each with ten spanwise rows of holes, are interchangeable. The plenum/jet plate assembly was mounted over the test plate unit (impingement plate) through interchangeable spacers which fixed the channel height (i.e., the jet exit plane-to-impingement surface spacing). The spacers also formed the upstream end-surface and side walls of the channel, thus constraining the initial crossflow and the jet flow to discharge in a single direction to the

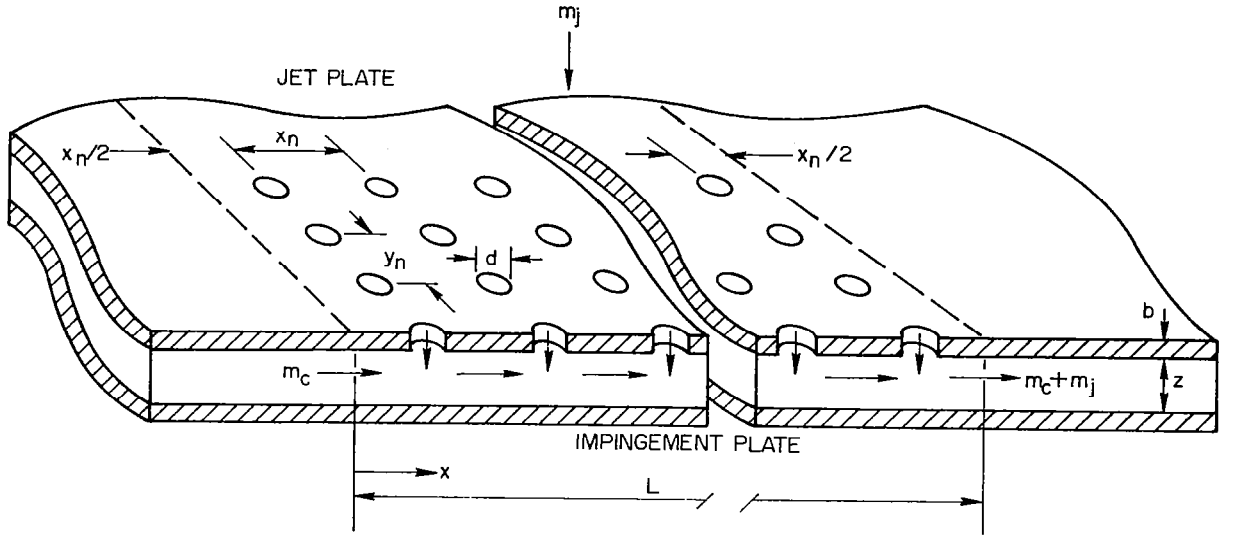

Fig. 3.1 Initial crossflow basic test model geometry and nomenclature.

laboratory environment at atmospheric pressure. The test plate unit consists of a segmented copper heat transfer test plate with individual segment heaters, the necessary thermal insulation, and the test plate support structure. The segmented design provides for control of the streamwise thermal boundary condition at the heat transfer surface, as well as for determination of spatially resolved heat transfer coefficients in the streamwise direction. Note that in the configuration shown the spanwise rows of jet holes are centered over the test plate segments, one row per segment. This results in a streamwise resolution of measured heat transfer coefficients equivalent to one streamwise jet hole spacing. There are a total of 31 segments in the test plate, 19 upstream of the jet array, 10 immediately opposite the array, and two downstream of the array.

Significant geometric characteristics of the configurations tested are summarized in Table 3.1. The array of length L = 12.7 cm with matching jet plenum (Fig. 3.2) was designated as size B. The jet plates are identified by the notation $B(x_n/d,y_n/d)I$ where the I designates an inline hole pattern, replaced by S to designate a staggered pattern. A staggered pattern was identical to its inline counterpart, except that alternating spanwise rows of holes were offset by one-half the spanwise spacing. Note that the overall channel width exceeded the width of the heat transfer test plate and that the

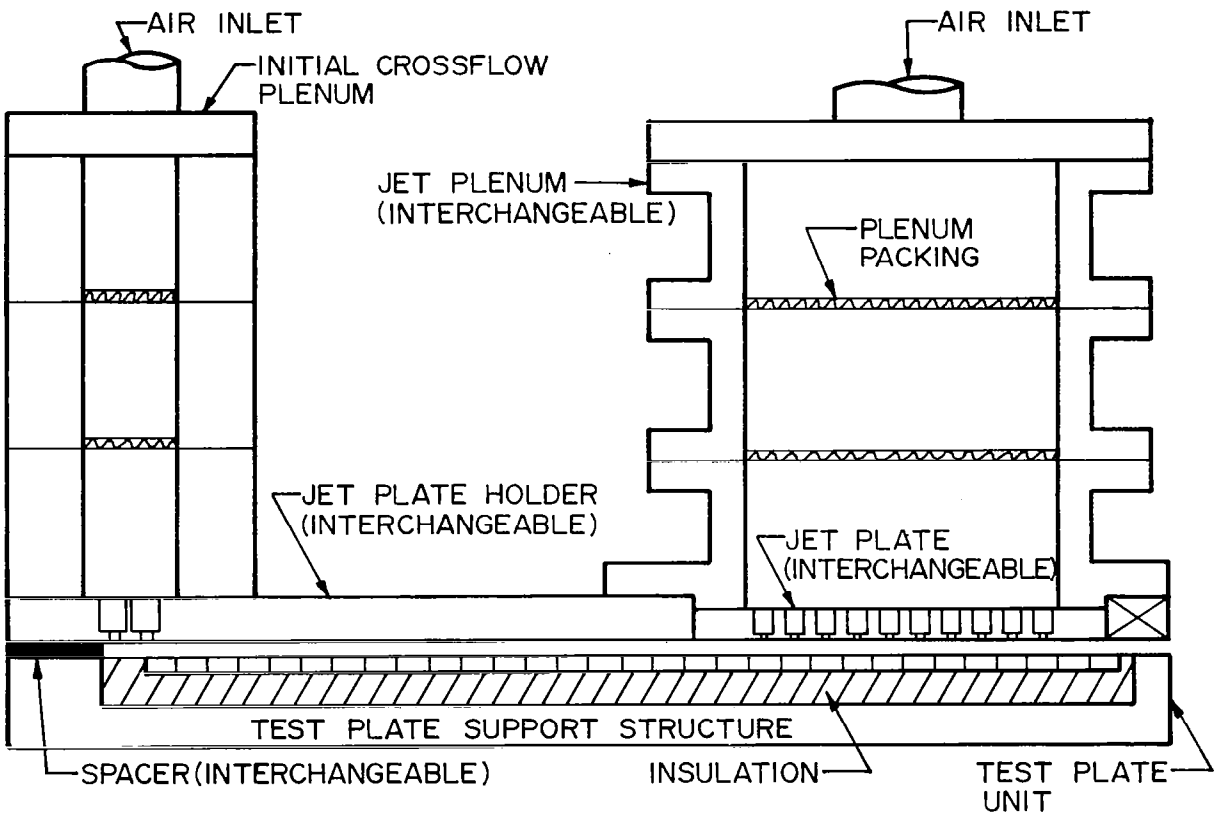

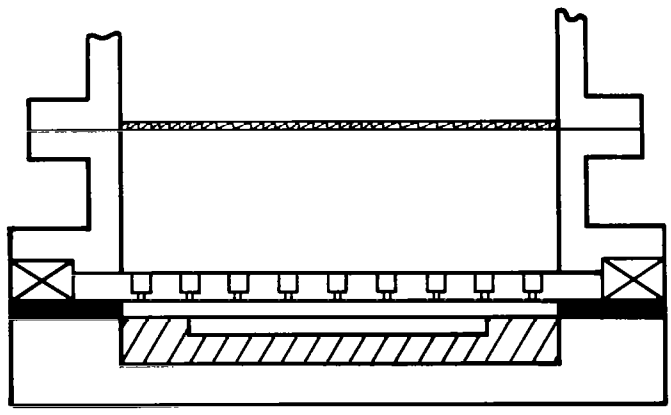

SPANWISE VIEW

Fig. 3.2 Initial crossflow test facility schematic.

number of holes across the channel (N_s') exceeded the number across the test plate (N_s). Jet holes were always symmetrically aligned with both the edges of the channel and the edges of the heat transfer test plate. Reckoned from the centerline of the second (i.e., downstream) spanwise jet row of the initial crossflow plenum, the channel length available for flow development upstream of the jet array (initial crossflow development length, 24.1 cm) ranged from 16 to 95 hydraulic diameters, depending on the channel height. It may also be noted that this length was 19 times the streamwise hole spacing in the main jet array (x_n = 1.27 cm). Average jet plate discharge coefficients, to be discussed later, are also included in Table 3.1.

The jet plates were machined from aluminum. The jet plate thickness, b, at each hole location was equal to the jet hole diameter. This was achieved by appropriately counterboring jet plates of a larger overall thickness, 1.1 cm (Fig. 3.2). This design feature was dictated primarily by the desire to insure accurate channel heights during test runs, a particularly critical requirement for the narrowest channel heights. The counterbore was three jet hole diameters, except for the narrowest hole spacings where a two-diameter counterbore was used. The B(10,8)I jet plate was originally machined with a 2d counterbore and utilized in that form for both heat transfer and discharge coefficient tests. The counterbored holes were subsequently bored out to 3d, with both the heat transfer tests (at z/d = 1) and discharge coefficient tests repeated over a range of jet Reynolds numbers. The results were identical to within experimental uncertainty.

The copper test plate segments were 0.635 cm thick and 1.19 cm wide with 0.079 cm balsa wood insulation bonded between adjacent segments to minimize heat leak. The individual heaters were foil-type bonded to the underside of each segment, each with power input controlled by a separate variac. The edges and undersides of the segment/heater assemblies were bonded to basswood, selected for the combination of structural and insulating qualities it provided. Those insulation surfaces which would have formed part of the channel and been exposed to the air flow were surfaced with 0.079 cm Lexan plastic to provide a smooth aerodynamic surface and prevent possible erosion of the wood insulation materials. The primary temperature instrumentation in the test plate consisted of copper-constantan thermocouples mounted in the

Table 3.1. Geometric Parameters and Mean Discharge Coefficients for Jet Plates Tested.

Jet Plate $B(x_n/d, y_n/d)I$	A_o^*	d and b (cm)	N_s	N_s'	$\bar{C}_D$
B(5,4)I(&S)	0.0393	0.254	12	18	0.85
B(5,8)I	0.0196		6	9	0.80
B(10,4)I	0.0196	0.127	24	36	0.76
B(10,8)I	0.0098		12	18	0.76

Channel heights, (z/d) = 1, 2, and 3

Fixed Parameters:

Channel width (span), w = 18.3 cm

Heat transfer test plate width, 12.2 cm

Heat transfer test plate length, 39.4 cm

Overall channel length, 43.2 cm

Initial crossflow channel length, 26.0 cm

B-size jet array and plenum length, L = 12.7 cm

Downstream exit length, 4.5 cm

Initial crossflow development length, 24.1 cm

Number of spanwise rows of jet holes, N_c = 10

I = Inline, S = staggered hole pattern

center of each copper segment, with a redundant thermocouple in each segment offset 1.52 cm in the spanwise direction. Several segments at intervals along the plate had additional thermocouples mounted out to the edge to verify that the spanwise temperature distributions during testing were essentially uniform. Thermocouple output signals and heater power input signals were recorded on a digital data logger.

4. FLOW DISTRIBUTIONS WITH INITIAL CROSSFLOW

4.1 Experimental Procedures and Data Reduction

The initial cross flow rate and total jet flow rate for each test condition were measured utilizing standard square-edge orifice plates in flow metering sections upstream of the respective plenums. Plenum pressure levels were measured via static pressure taps, while plenum air temperatures were determined using copper-constantan thermocouples. All pressure measurements were made with either U-tube or single leg well-type manometers. Flow rates at the flow metering sections were computed according to [12] which gives values of flow coefficients for standard square-edged orifice plates. Plenum air temperatures were nominally at ambient levels of about 300K. Plenum pressures ranged from slightly above the nominal exhaust pressure level of one atmosphere to as high as 275 kPa depending on test conditions. The distribution of the jet flow among the individual spanwise rows of the array was determined from measurements of streamwise channel pressure profiles and jet plate discharge coefficients.

Streamwise channel pressure traverses were accomplished with static pressure probes inserted from the open downstream end of the channel as shown in Fig. 4.1. The probes were stainless steel tubes of either 0.089 or 0.124 cm outside diameter and 0.015 or 0.020 cm tube wall thickness, respectively, closed at the upstream end, with a single orifice of 0.0254 cm in the tube sidewall located 0.32 cm from the end. The smaller diameter tube was used for the channel heights of less than 0.254 cm. For a given run the tube was positioned along one lower corner of the channel and pressed against the channel side wall and bottom by slightly bowing the tube. This positioning provided support of the tube, thus preventing vibration and possible whipping in the presence of a strong channel flow. It may be noted that each channel side wall location, hence the nominal probe position, was at a plane of symmetry midway between streamwise hole row centerlines. For most traverses the orifice was positioned facing upward toward the jet plate, with readings made opposite each spanwise jet row location. For some traverses readings were also made midway between spanwise jet rows. And in some instances,

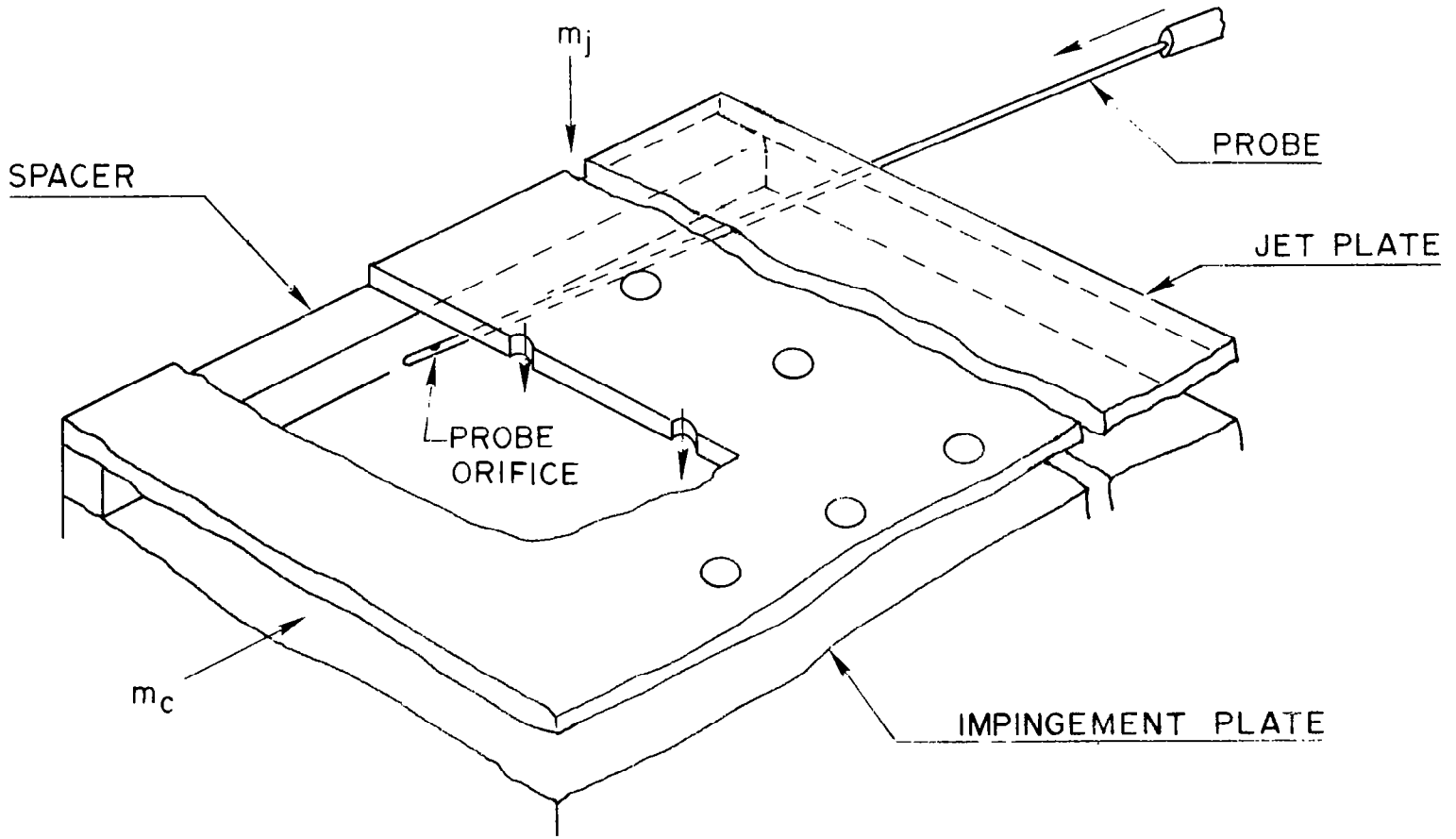

Fig. 4.1 Pressure traverse test configuration.

traverses were repeated with the orifice positioned facing downward toward the impingement surface, or toward the channel sidewall. These, as well as prior similar results, showed that the pressure measurements were not normally very sensitive to the orifice orientation and that the profiles were rather smooth in traversing from positions between jet rows to positions immediately opposite jet rows. This indicated that dynamic pressure effects were normally of minor significance.

Discharge coefficients for each jet plate were previously determined by separate tests [2]. These tests were conducted with the plenum/jet plate assembly removed from the impingement plate and discharging directly to the laboratory environment at atmospheric pressure. Discharge coefficients were defined in the standard manner as the ratio of the actual to the ideal flow rate, where the latter was calculated assuming one-dimensional isentropic perfect gas flow, using measured values of plenum pressure, plenum temperature, and atmospheric pressure. The defining equation is

$$G_j = C_D P_o (P/P_o)^{1/\gamma} \{2\gamma(\gamma-1)^{-1}(RT_o)^{-1}[1-(P/P_o)^{(\gamma-1)/\gamma}]\}^{1/2} \qquad (4.1)$$

where $G_j = m_j/A_o$. The actual flow rate (m_j) was determined via the standard orifice in the flow metering section upstream of the plenum. A discharge coefficient determined as described above is an average value over all holes in the jet plate. While discharge coefficients for individual holes were not determined, each jet plate was checked for flow uniformity with very satisfactory results as detailed in [1]. Discharge coefficients for each jet plate were measured over a nominal range of jet Reynolds numbers from 2.5×10^3 to 5×10^4. The jet plate discharge coefficient as a function of jet Reynolds number is illustrated for B(5,8)I in Fig. 4.2. The values were found to be essentially independent of Re_j over this range. The values summarized in Table 3.1 are mean values over the range.

The jet mass velocity for each spanwise row of holes was calculated based on Eq. (4.1) using the channel pressure measured at the row location and $C_D = \bar{C}_D$ for the particular jet plate (Table 3.1). The sum of the flow rates over all ten rows was then compared with the standard orifice measurement of the total jet flow rate. These mass balances ordinarily closed to within a

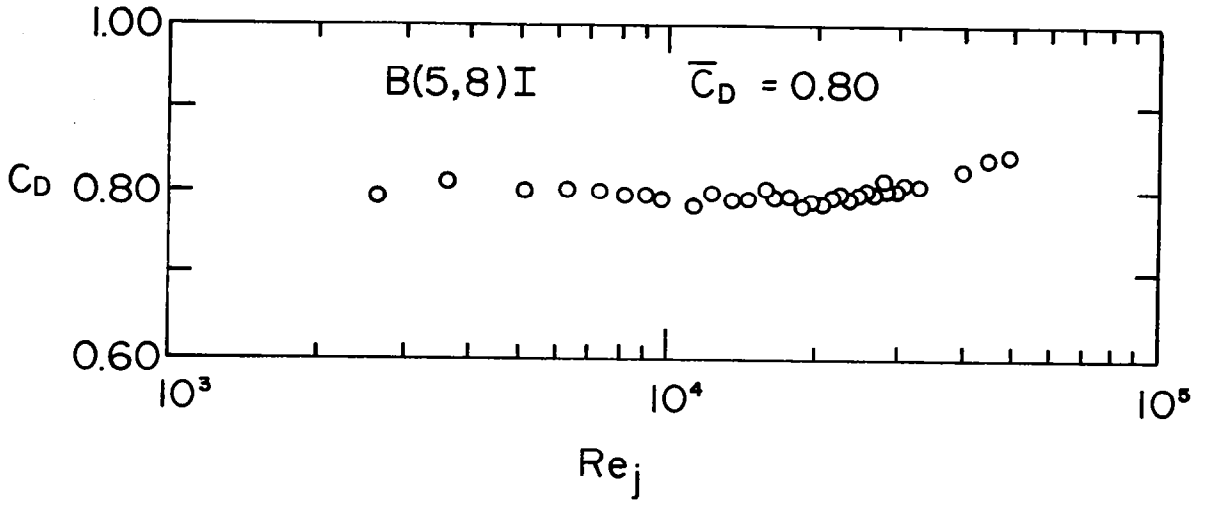

Fig. 4.2 Jet plate discharge coefficient as a function of jet Reynolds number in absence of crossflow and impingement surface.

few percent. However, for tests with the smaller channel heights and larger initial crossflow rates significant discrepancies up to 42% were observed. The discrepancies were thought to be due to crossflow and/or impingement surface proximity effects on the discharge coefficients.

Several special tests were then conducted to determine the effect of crossflow and impingement surface proximity on the discharge coefficients. These tests were performed with the plenum jet plate assembly mounted over the impingement plate as in standard flow distribution tests, but with the last nine spanwise rows plugged leaving only the upstream row open. This permitted the jet flow rate through the single open row to be measured directly at the standard orifice flow metering section upstream of the jet plenum. A crossflow rate was also orifice-metered and then introduced through the initial crossflow plenum as in the standard flow distribution tests. The channel pressure at the open row location was measured with the static pressure probe, using the same technique as described above for the channel pressure traverses. In this way, discharge coefficients were determined as a function of crossflow-to-jet velocity ratio (G_c/G_j) and impingement surface proximity (z/d). The use of these results in the reduction of the flow distribution

data greatly improved the mass balances (flow rate closures) in those cases where significant discrepancies had existed. The detailed results of the special tests for the crossflow effect on discharge coefficients are presented in the next section.

4.2 Effect of Crossflow on Discharge Coefficients

Special discharge coefficient tests were conducted as just described using the B(5,4)I jet plate at z/d = 1,2, and 3 and the B(5,8)I jet plate at z/d = 1. The jet flow rate was set to give a jet hole Reynolds number of 10^4. The crossflow was then varied to give a range of G_c/G_j for one spanwise row of holes. The results are plotted in Fig. 4.3. Tabular values are listed in Appendix C, Table C.1. For the larger values of G_c/G_j the jet Reynolds numbers were set at less than 10^4 in order not to exceed the available

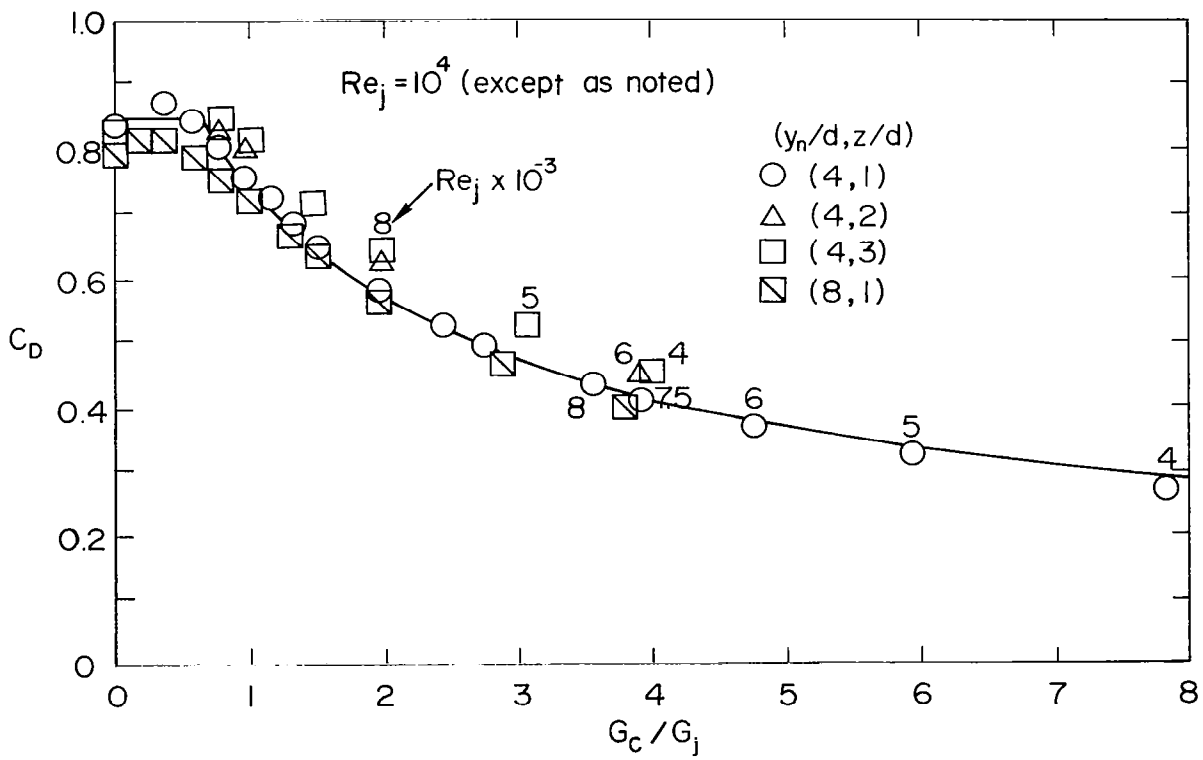

Fig. 4.3 Effect of confined crossflow on jet orifice discharge coefficient.

compressed air supply for the crossflow rate. For these cases the specific Re_j values are noted in the Figure adjacent to the appropriate data points. The composite uncertainty for these C_D values was estimated by the method of Kline and McClintock [13] to be $\pm$ 3% (Appendix B).

The behavior indicated is that C_D remains essentially constant for G_c/G_j ranging from zero to a value somewhat less than unity. The data in this range is in close agreement with the individual jet plate average values previously determined in the absence of both a crossflow and an impingement surface (Table 3.1). Beyond this range C_D decreases significantly in a smooth monotonic fashion, and values for z/d = 2 and 3 are somewhat larger than values for z/d = 1.

To examine the sensitivity of C_D to Re_j in the presence of a confined crossflow, a second set of special tests was conducted using the upstream row of holes of the B(5,4)I jet plate with z/d = 1. G_c/G_j was maintained constant at several different values. At each value, C_D was measured over a range of

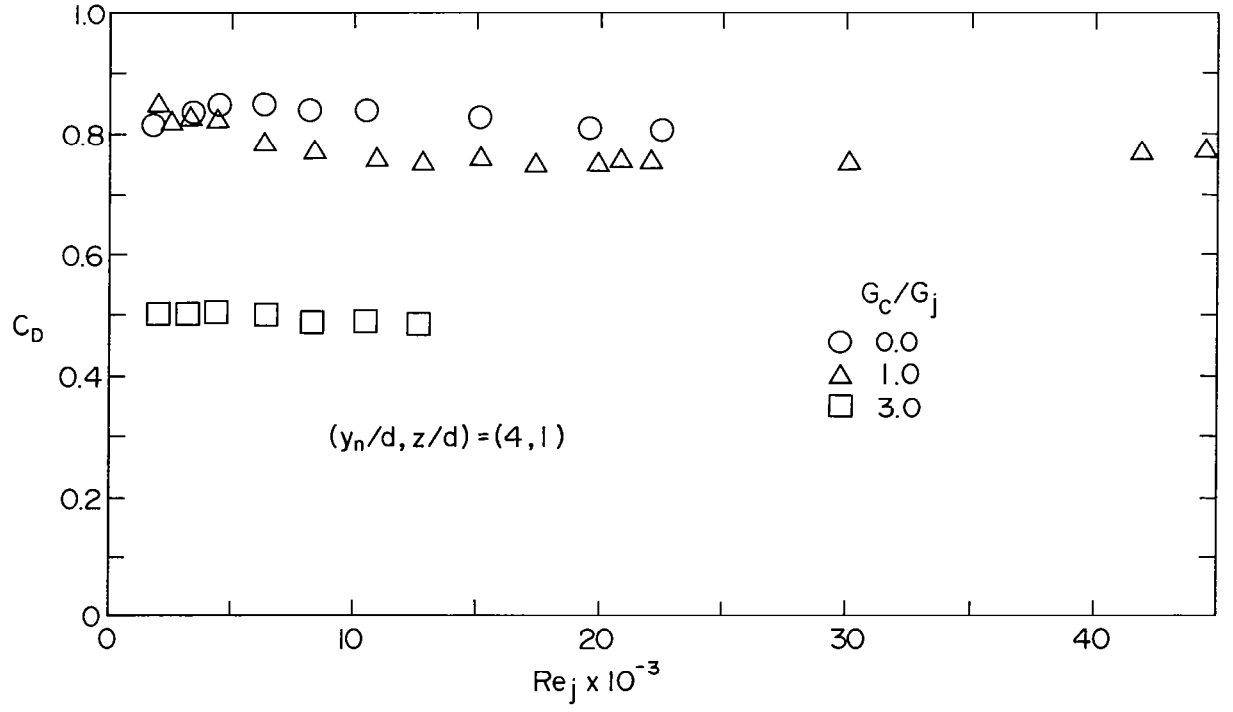

Fig. 4.4 Effect of jet Reynolds number on jet orifice discharge coefficients for several values of cross-to-jet mass velocity ratio.

Re_j. The results (Fig. 4.4, also Appendix C, Table C.2) indicate that for $G_c/G_j = 0$, C_D is not very sensitive to Re_j, which is consistent with the prior test results made with the full jet plate in the absence of both a crossflow and an impingement surface. For the finite values of G_c/G_j, a similar conclusion may be drawn, though for $G_c/G_j = 1$ some small dependence is noticeable as Re_j drops below about 5×10^3. Nevertheless, deviations from a mean value over the Re_j range are no larger than a few percent.

Labeling the value of G_c/G_j at which C_D begins to decrease as the ''break point'' (bp) value the observed behavior may be summarized as follows: (1) for $0 \leq G_c/G_j \leq (G_c/G_j)_{bp}$, C_D may be considered constant (i.e., independent of G_c/G_j and z/d) and equal to $\bar{C}_D$, (2) for $G_c/G_j > (G_c/G_j)_{bp}$, C_D depends primarily on G_c/G_j and secondarily on z/d, and (3) for practical purposes C_D may be considered independent of Re_j.

In order to make use of these results in the reduction of the flow distribution data, algebraic representations of C_D vs. G_c/G_j were developed. These are summarized in Table 4.1. The function $\xi(G_c/G_j)$ appearing in Table 4.1 is defined by

$$\xi(G_c/G_j) = \frac{1.06}{(G_c/G_j + 0.806)^{0.602}} \qquad (4.2)$$

This represents a nonlinear least squares curve fit to the C_D data points for $G_c/G_j > (G_c/G_j)_{bp}$ obtained using the B(5,4)I jet plate with z/d = 1 (open circles in Fig. 4.3). The coefficients of ξ shown in Table 4.1 for the (5,4) plate at z/d = 2 and 3 (1.08 and 1.11, respectively) are the best fit constant multipliers of ξ based on the z/d = 2 and 3 data, respectively. The equation for intermediate G_c/G_j values for the (5,8,1) case is a best fit straight line constrained to be tangent to the ξ function at $G_c/G_j = 1.5$. For clarity, only the curve for the (5,4,1) case is shown in Fig. 4.3.

Since the (10,4) and (10,8) jet plates were not used in conducting the special C_D tests, the representation summarized in Table 4.1 for the (10,4,1) and (10,8,1) configurations was inferred from the results for the (5,4,1) and (5,8,1) cases. The ''break point'' was set at the same value as existed for the (5,8,1) case. As in the prior cases, C_D for G_c/G_j below the ''break point'' was set equal to $\bar{C}_D$ from Table 3.1. Since only one spanwise row of

Table 4.1. Algebraic Representations for Dependence of Discharge Coefficients on the Crossflow Parameter (G_c/G_j).

Configuration	Equation	Range of G_c/G_j
B(5,4,1)I	$C_D = \begin{cases} 0.85 \\ \xi(G_c/G_j) \end{cases}$	0 to 0.63 > 0.63
B(5,4,2)I	$C_D = \begin{cases} 0.85 \\ 1.08\xi(G_c/G_j) \end{cases}$	0 to 0.83 > 0.83
B(5,4,3)I	$C_D = \begin{cases} 0.85 \\ 1.11\xi(G_c/G_j) \end{cases}$	0 to 0.90 > 0.90
B(5,8,1)I	$C_D = \begin{cases} 0.80 \\ -0.169(G_c/G_j)+0.893 \\ \xi(G_c/G_j) \end{cases}$	0 to 0.54 0.54 to 1.5 > 1.5
B(10,4,1)I and B(10,8,1)I	$C_D = \begin{cases} 0.76 \\ -0.128(G_c/G_j)+0.825 \\ \xi(G_c/G_j) \end{cases}$	0 to 0.54 0.54 to 1.8 > 1.8

Note: The function $\xi(G_c/G_j)$ is defined by Eq. (4.2).

holes was open, the values of C_D are independent of x_n/d in this test. Accordingly, for the largest values of G_c/G_j, the ξ function was used, with a linear function joining the ''break point'' with the ξ function.

The determination of the jet velocities from the pressure traverse results, using Eq. (4.1), requires special consideration when C_D depends on G_c/G_j since then C_D is not known a priori. This requires an iterative calculation involving Eq. (4.1) and the appropriate equation from Table 4.1, with G_j and C_D at the row in question as the unknowns. The value of G_c approaching the row is already known based on the sum of the initial crossflow rate and the total jet flow upstream of the row in question. The jet mass velocity may thus be determined at each row, in turn, proceeding in the downstream direction. The effect of these results for C_D vs. G_c/G_j on the overall mass balances is presented in Table 4.2 for those cases where G_c/G_j at one or more rows exceeded $(G_c/G_j)_{bp}$. The mass closures for both constant and variable C_D are listed. For $(G_c/G_j)_{max}$ slightly larger than $(G_c/G_j)_{bp}$, the mass balances with constant C_D closed to within a few percent of unity, and the use of variable C_D did not change the mass balances significantly. For $(G_c/G_j)_{max}$ considerably larger than $(G_c/G_j)_{bp}$, the mass closures with constant C_D were much larger than unity, and the results were improved significantly by use of the variable C_D.

Only for the B(5,8,1)I case at $m_c/m_j = 0.52$ was the mass closure distinctly worsened. A possible explanation may be related to the fact that the upstream history of the crossflow approaching a given row within the array was not, in general, identical to the upstream history of the crossflow for the special discharge coefficient tests. For the special tests a crossflow distributed uniformly across the span of the channel approaches the jet row. However, the local crossflow velocity immediately upstream of a jet in a row within an array may be somewhat less than the average velocity across the span of the channel due to the partial diversion of the crossflow around jets immediately upstream of the row in question. Therefore, the spanwise local value of G_c/G_j seen by a jet within the array may be somewhat lower than the average across the span, resulting in a slightly higher actual C_D value than that predicted based on the results of the special tests. It may be noted that, overall, the adjustments in the closures by use of the variable C_D for

Table 4.2 Effect of Variable Discharge Coefficient on Overall Mass Balances ($\overline{Re}_j \simeq 10^4$).

Configuration	m_c/m_j	Mass Closure* With C_D Constant	Mass Closure* With C_D Variable	$(G_c/G_j)_{max}$	$(G_c/G_j)_{bp}$
B(5,4,1)I	0.00	1.03	1.00	0.79	0.63
	0.20	1.09	0.99	2.71	
	0.51	1.22	0.97	51.4	
	0.99	1.42	1.00	29.4(See Note 3)	
B(5,4,2)I	0.49	1.01	1.01	0.89	0.83
	1.01	1.13	0.98	4.73	
B(5,4,3)I	0.99	1.00	0.99	1.05	0.90
B(5,8,1)I	0.00	0.95	0.94	0.61	0.54
	0.20	0.94	0.93	0.68	
	0.52	0.99	0.91	1.18	
	0.99	1.13	0.94	4.00	
B(10,4,1)I	0.00	1.01	0.98	0.82	0.54
	0.49	1.14	0.98	53.8	
B(10,8,1)I	0.00	0.98	0.97	0.66	0.54
	0.23	0.98	0.96	0.76	
	0.46	1.01	0.96	0.85	
	1.01	1.15	0.99	3.86	

Note 1: Only those cases where G_c/G_j at one or more rows exceeded $(G_c/G_j)_{bp}$ are listed.

Note 2: Data for B(10,4,1)I at m_c/m_j = 0.2 and 1.0 and B(10,4,2)I cases were not available.

Note 3: This is the value at the third spanwise row of holes. The values of G_j at the first two rows were too close to zero to be well defined relative to experimental uncertainty. Therefore, the values of G_c/G_j at these rows are very large and highly uncertain.

*Ratio of sum of individual row flow rates to total flow rate measured at flow metering orifice upstream of jet plenum.

the B(10,8,1)I case are better than for the B(5,8,1)I case. This is consistent with the explanation suggested above since, with $x_n/d = 10$ as opposed to 5, the crossflow approaching a row within the array has a longer ''entrance length'' over which to adjust and become more nearly uniformly distributed across the span before reaching that row.

In a prior study by Damerow, et al. [14], no significant effect of a confined crossflow on jet orifice discharge coefficients was found. Since in that study the maximum value of G_c/G_j was only about 0.8 at $z/d = 3.0$, the conclusion reached is quite consistent with the present results. For angled film cooling holes Meitner and Hippensteele [15] found a significant effect of the mainstream flow on the coolant injection rate for coolant-to-mainstream momentum flux ratios less than about 0.4.

4.3 Flow Distribution Model

4.3.1 Formulation

In an earlier study [2,11] a simple one-dimensional, incompressible flow distribution model was found to be adequate for predicting flow distributions for the array geometries considered here, under a noninitial crossflow condition. The model was developed by assuming the discrete hole array to be replaced by a surface over which the injection is continuously distributed. It also included the assumptions of constant discharge coefficient and negligible effect of channel wall shear. A similar approach was used by Dyban, et al. [16] for arrays with no initial crossflow, including some attempt at accounting for channel friction effects. Martin [17] applied a similar model for a geometry in which the injected flow was in fact continuous in the streamwise direction, i.e., an array of slot nozzles in which the outlet flow was constrained to exit parallel to the slots.

The basic model developed in [2,11] is here extended to include the presence of an initial crossflow. For some of the geometries considered the effect of crossflow on the discharge coefficient and the effect of wall shear were found to be significant when an initial crossflow was present. The model is therefore extended to include these effects as well.

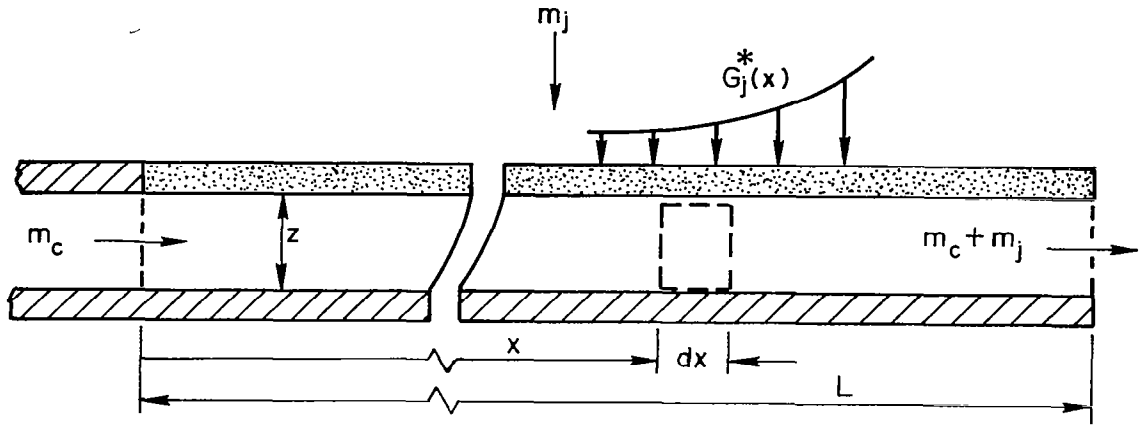

Fig. 4.5a Continuous injection model.

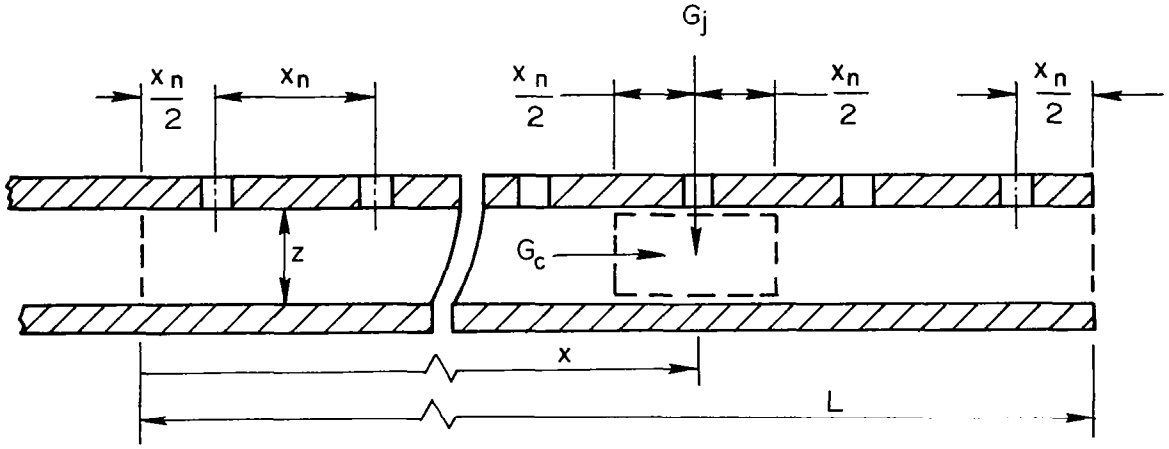

Fig. 4.5b Discrete hole injection model.

Consider the continuous injection model illustrated in Fig. 4.5a. The continuously distributed injection velocity G_j^* is related to the jet velocity G_j (Fig. 4.5) through the open area ratio, $G_j^* = G_j A_o^*$. The distributed injection velocity may then be written in terms of the discrete hole discharge coefficient as

$$G_j^* = A_o^* C_D [2\rho(P_o - P)]^{1/2} \qquad (4.3)$$

where, in general, we consider

$$C_D = C_D(G_c/G_j)$$

A force-momentum balance on the control volume indicated in Fig. 4.5 results in

$$dP = -\frac{2G_c dG_c}{\rho} - \frac{2\tau_w dx}{z} \tag{4.4}$$

A mass balance leads to

$$G_j^* = \frac{z dG_c}{dx} \tag{4.5}$$

For constant P_o, the elimination of G_j^* and P from Eqs. (4.3), (4.4), and (4.5) in favor of G_c yields in dimensionless form (See Appendix A).

$$\frac{d^2\tilde{G}_c}{d\tilde{x}^2} = \frac{B^2\tilde{G}_c[1+f(L/2z)\tilde{G}_c/(d\tilde{G}_c/d\tilde{x})] + C(d\tilde{G}_c/d\tilde{x})}{1 + C\tilde{G}_c/(d\tilde{G}_c/d\tilde{x})} \tag{4.6}$$

where

$$B = \sqrt{2}\ A_o^* C_D L/z$$

and

$$C = \frac{A_o^* L}{z} \cdot \frac{1}{C_D} \cdot \frac{dC_D}{d(G_c/G_j)}$$

In the presence of an initial crossflow the boundary conditions are $G_c = m_c/(z \cdot w)$ at $x = 0$ and $G_c = (m_c + m_j)/(z \cdot w)$ at $x = L$ or in dimensionless form

$$\tilde{G}_c = M/(1 + M) \qquad \text{at} \qquad \tilde{x} = 0 \tag{4.7a}$$

$$\tilde{G}_c = 1 \qquad \text{at} \qquad \tilde{x} = 1 \tag{4.7b}$$

Eq. (4.6) is nonlinear and must be solved numerically for the general case. Numerical solutions will be presented shortly. However, for the important and useful special case where C_D is constant and wall shear is

negligible (f = 0) the equation is linear and closed form solutions may be easily written.

4.3.2 Closed Form Solutions for Constant C_D, f = 0

For constant C_D and f = 0, Eq. (4.6) simplifies to

$$\frac{d^2\tilde{G}_c}{d\tilde{x}^2} - B^2\tilde{G}_c = 0 \qquad (4.8)$$

The solution to Eq. (4.8) for $\tilde{G}_c$ with boundary conditions of Eqs. (4.7a) and (4.7b) may be conveniently written in terms of hyperbolic trigonometric functions:

$$\tilde{G}_c = \frac{1 - [M/(1 + M)]\ \text{coshB}}{\text{sinhB}}\ \text{sinhB}\tilde{x} + \frac{M}{1 + M}\ \text{coshB}\tilde{x} \qquad (6.7)$$

The corresponding continuous injection velocity G_j^* may then be written in closed form with the aid of Eq. (4.5). This result is then utilized to evaluate the discrete hole array jet velocity distribution by assuming that the value of G_j for a given spanwise row of holes is that corresponding to $G_j^*(x)$ with x evaluated at the centerline of the row. Utilizing $A_o^*\bar{G}_j = m_j/(w \cdot L)$, the final result for the jet velocity distribution is

$$\frac{G_j}{\bar{G}_j} = B\ \frac{(1 + M)\text{coshB}\tilde{x} - M\text{coshB}(1 - \tilde{x})}{\text{sinhB}} \qquad (4.10)$$

The crossflow parameter of interest is the crossflow velocity approaching a given spanwise jet row relative to the jet velocity of the row. This may be satisfactorily approximated utilizing G_c from the continuous injection model evaluated one-half a hole spacing upstream of the given row (Fig. 4.5b), divided by G_j from Eq. (4.10). This operation results in

$$\frac{G_c}{G_j} = \frac{1}{\sqrt{2}\ C_D}\ \frac{(1 + M)\text{sinhB}\tilde{x}' + M\text{sinhB}(1 - \tilde{x}')}{(1 + M)\text{coshB}\tilde{x} - M\text{coshB}(1 - \tilde{x})} \qquad (4.11)$$

where $\tilde{x}' = \tilde{x} - (1/2)(x_n/L)$

4.3.3 Numerical Solutions

For conditions under which C_D is dependent on G_c/G_j or the wall

shear term is included, or both, Eq. (4.6) must be solved numerically. In each case, C_D was evaluated as a function of G_c/G_j using the appropriate equation from Table 4.1. Note that G_c/G_j may be written in the form

$$\frac{G_c}{G_j} = \frac{A_o^* L}{z} \cdot \frac{\tilde{G}_c}{(d\tilde{G}_c/d\tilde{x})} \tag{4.12}$$

with the aid of Eq. (4.5) and the relation $G_j^* = G_j \cdot A_o^*$. Thus, C_D may be considered as a function of $\tilde{G}_c$ and $d\tilde{G}_c/d\tilde{x}$.

For the complex flow conditions encountered in these jet array geometries a general accurate model for the friction factor is not available. However, in order to assess the significance of wall shear effects the friction factor was approximated according to standard representations for fully developed flow in smooth ducts of constant cross section [18] and extending the lower limit of Re_c for turbulent flow from 5×10^3 to 2×10^3 to include a transition region:

$$f = \begin{cases} 24/Re_c & Re_c < 2\times10^3 \\ 0.079/Re_c^{0.25} & 2\times10^3 < Re_c < 3\times10^4 \\ 0.046/Re_c^{0.20} & Re_c > 3\times10^4 \end{cases} \tag{4.13}$$

For use in Eq. (4.6), the crossflow channel Reynolds number appearing in these friction factor expressions may be replaced by

$$Re_c = 2\tilde{G}_c \overline{Re}_j (1 + M) A_o^* (L/d) \tag{4.14}$$

To proceed with the numerical solution of Eq. (4.6) with boundary conditions (4.7a) and (4.7b) it is necessary to specify the geometrical parameters, the flow ratio M and the mean jet Reynolds number $\overline{Re}_j$. Then, taking into account (4.12), (4.13), and (4.14), Eq. (4.6) is of the form

$$d^2\tilde{G}_c/d\tilde{x}^2 = fcn(\tilde{x}, \tilde{G}_c, d\tilde{G}_c/d\tilde{x}) \tag{4.15}$$

Solutions were obtained by the shooting method using a fourth order Runge-

Kutta method. Once the numerical solutions for $\tilde{G}_c$ were found, the final discrete hole array results for $G_j/\bar{G}_j$ and G_c/G_j were then obtained using the same approach as outlined above for the closed form solutions. These results are presented in graphical form in the next section.

As long as the continuous injection model results in an injection velocity distribution which is approximately linear over any given streamwise hole spacing, basing the discrete injection velocity on the continuous value evaluated at the jet row centerline should give essentially the same result as averaging the continuous distribution over the streamwise hole spacing centered at the jet row. As a check, the averaging method was applied to one of the most highly non-uniform flow distributions, the B(5,4,1)I geometry at $m_c/m_j = 0.2$. The differences in $G_j/\bar{G}_j$ and G_c/G_j between the two methods were less than 0.3 percent.

4.4 Results and Discussion

4.4.1 Flow Distributions

Experimental flow distribution results for seven different configurations are presented in Figs. 4.6 through 4.12, with one configuration represented by each Figure. Both the jet flow distribution ($G_j/\bar{G}_j$) and the cross-to-jet velocity ratio (G_c/G_j) are shown in each Figure for nominal values of $M = m_c/m_j$ at zero, 0.2, 0.5, and 1.0. However, in some instances the data for intermediate values of M is omitted for clarity. The closure obtained for the experimental mass balance in each case is listed in the Figures. This closure value is the ratio of the sum of the individual spanwise row jet flow rates to the total jet flow rate measured by the standard orifice. The data points for $G_j/\bar{G}_j$ were determined using $\bar{G}_j$ based on the sum of the individual row flow rates. This approach tends to compensate for any small bias which may have been present in the individual row measurements. The uncertainty associated with these data points was estimated by the method of Kline and McClintock [13]. The uncertainty for the $G_j/\bar{G}_j$ data points is about $\pm$ 2%. The uncertainty for the G_c/G_j data points ranges from about $\pm$ 2% for downstream rows, smaller values of m_c/m_j, and larger values of $(y_n/d)(z/d)$ to about $\pm$ 4% for upstream rows, larger m_c/m_j, and smaller $(y_n/d)(z/d)$ (see

Appendix B, Section B.1 for details). Tabular data for $G_j/\bar{G}_j$, G_c/G_j, and P/P_o for all tests may be found in Appendix D, Table D.1.

The solid curves in each Figure are based on the theoretical model with f = 0 (i.e. neglecting wall shear effects). For those cases where G_c/G_j did not exceed $(G_c/G_j)_{bp}$, C_D was constant and the solid curves are represented by the closed form solutions, Eqs. (4.10) and (4.11). These cases are indicated in the figures by the notation "C_D constant". Where C_D depended on G_c/G_j, indicated by the notation "C_D variable", the solid curves represent numerical solutions. Numerical solutions including the effect of wall shear ($f \neq 0$) are shown by dashed curves for those cases where the effect is noticeable relative to the corresponding f = 0 case.

Consider first Figs. (4.6), (4.7), and (4.8). These are geometries with $x_n/d = 10$, and values of the product $(y_n/d)(z/d)$ equal to or greater than 12. For the (10,8,3) case (Fig. 4.6), the jet flow distribution remains nearly uniform with a nearly uniform linear increase in G_c/G_j even for $m_c/m_j = 1$. As $(y_n/d)(z/d)$ decreases (Figs. 4.7 and 4.8) and m_c/m_j increases the flow distribution becomes more nonuniform. G_c/G_j continues to increase in a nearly linear fashion, but at $m_c/m_j = 1$ the initial crossflow has become large enough to cause G_c/G_j to be almost uniform for the (10,4,3) case (Fig. 4.8). The predictions show the effect of wall shear just beginning to appear for (10,8,2) and (10,4,3) at $m_c/m_j = 1$. Test results with $x_n/d = 5$ (Figures for these cases will be presented shortly) were essentially the same as those for $x_n/d = 10$ except for an even smaller effect of wall shear. The composite uncertainty (sensitivity) of these predictions due to uncertainties in the input parameters, again based on the method of Kline and McClintock [13], is less than about $\pm$ 2% for G_j/G_j, and about $\pm$ 4% for G_c/G_j except for upstream rows where it ranges up to about $\pm$ 7% (see Appendix B, Section B.2 including Tables B.1 and B.2 for details). In the light of these sensitivities and the previously noted data point uncertainties, verification of the predictions by the data is excellent.

Consider next Figs. 4.9 through 4.12. These geometries all have $(y_n/d)(z/d)$ equal to or less than eight, and all have z/d = 1, except the (5,4,2) case (Fig. 4.9). The flow distributions all become much more highly nonuniform with increasing m_c/m_j than for the previous cases considered. The

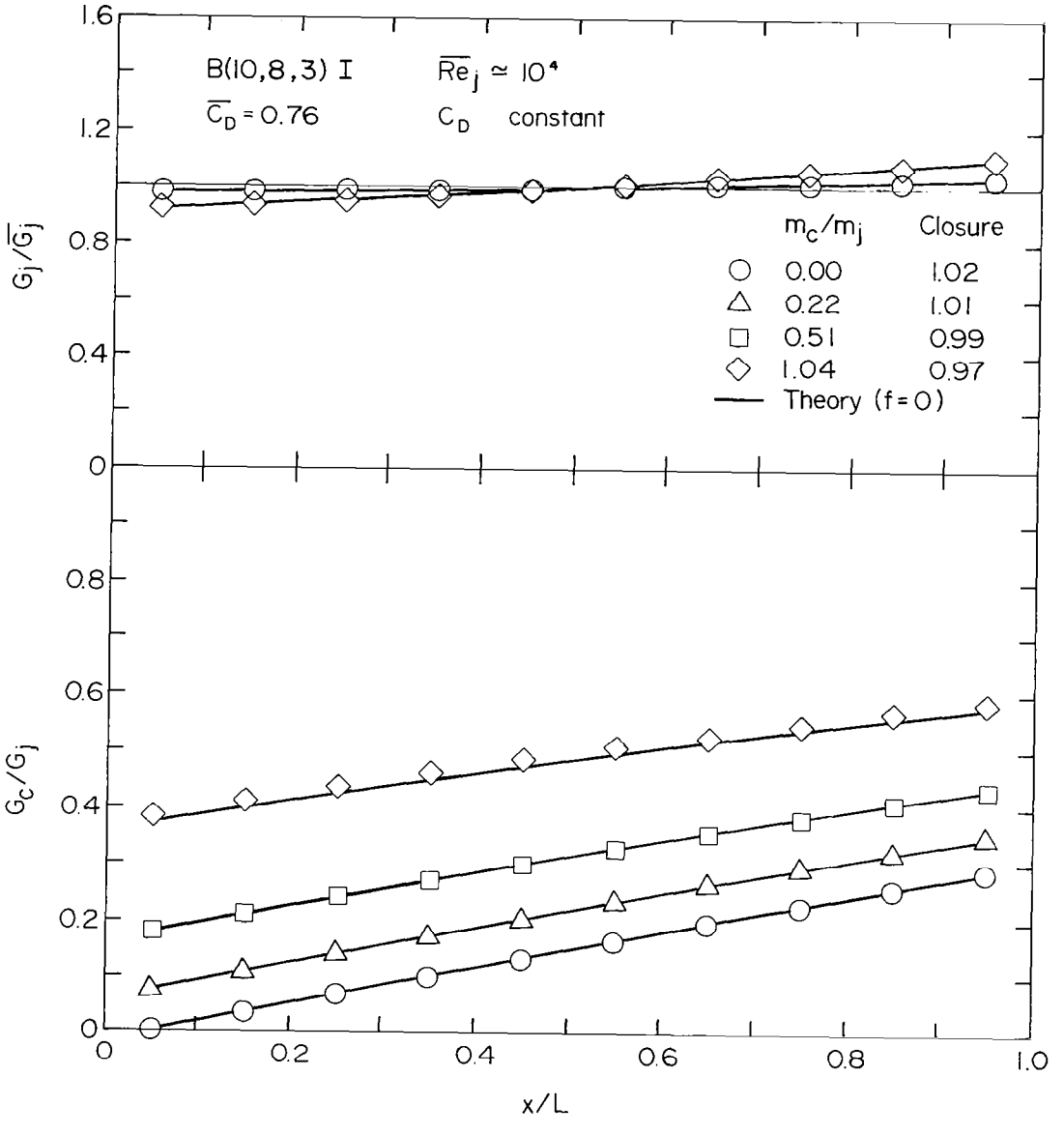

Fig. 4.6 Effect of initial crossflow on jet array flow distribution for B(10,8,3)I geometry - experimental data compared with predictive model.

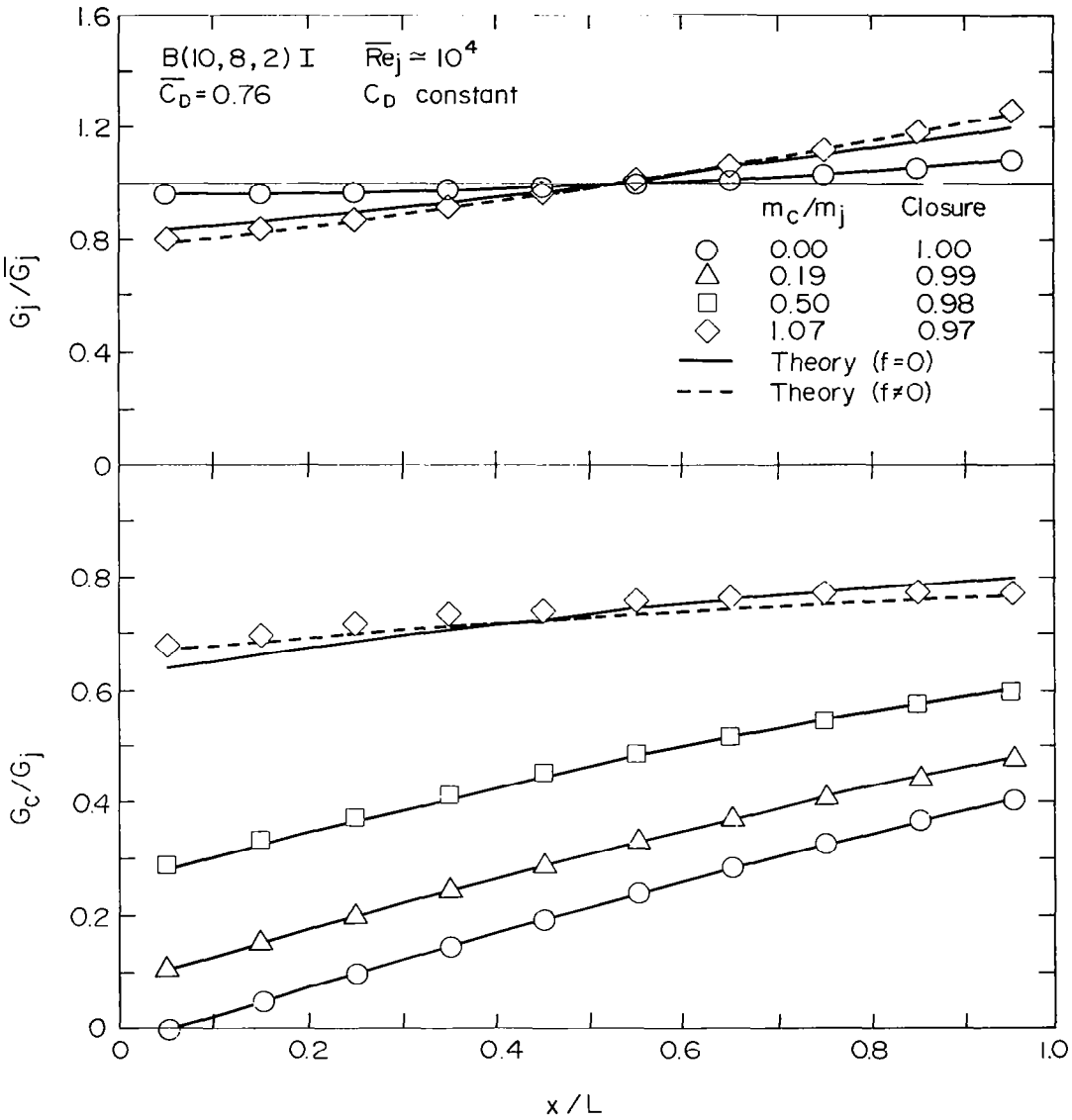

Fig. 4.7 Effect of initial crossflow on jet array flow distribution for B(10,8,2)I geometry - experimental data compared with predictive model.

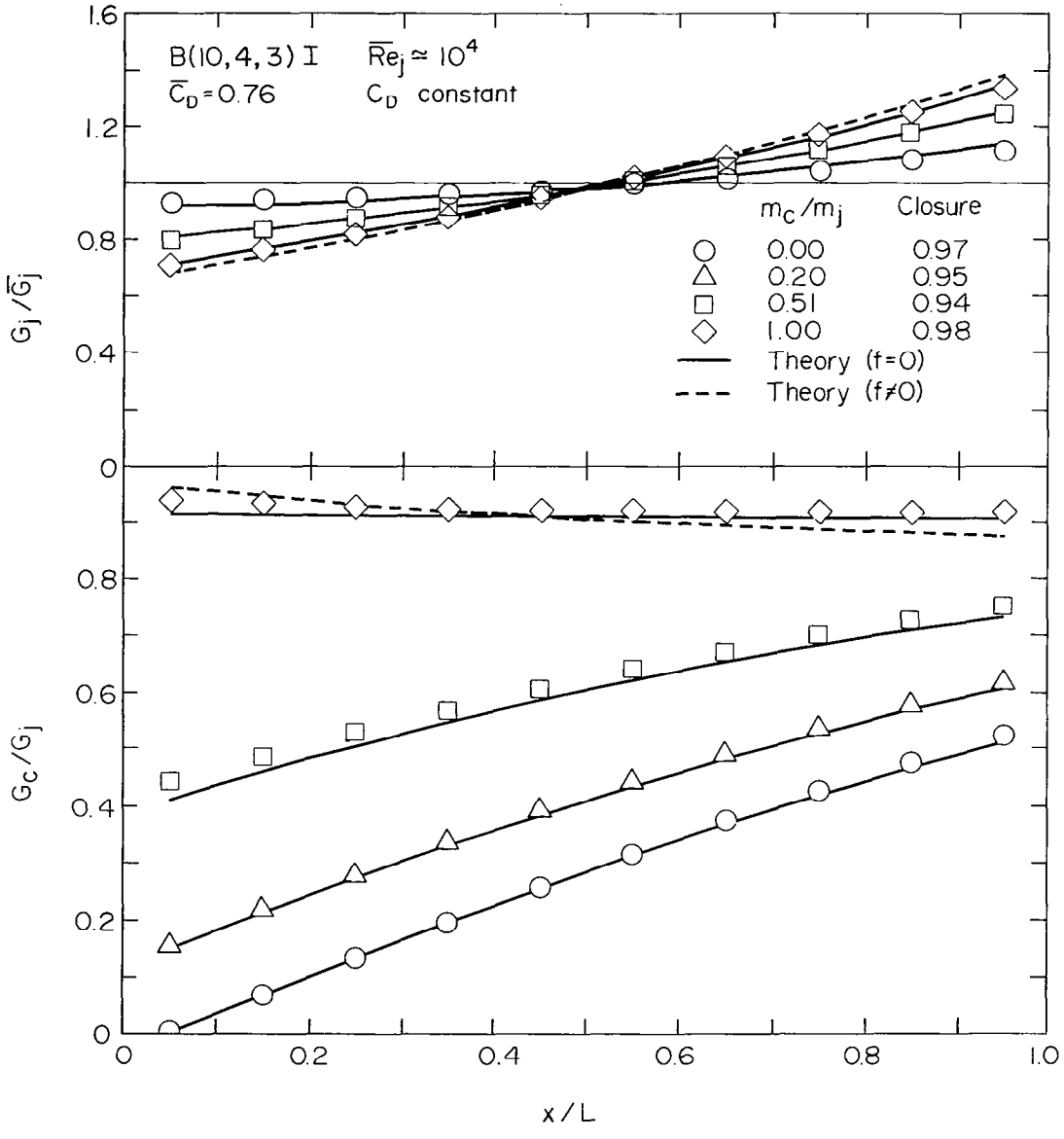

Fig. 4.8 Effect of initial crossflow on jet array flow distribution for B(10,4,3)I geometry - experimental data compared with predictive model.

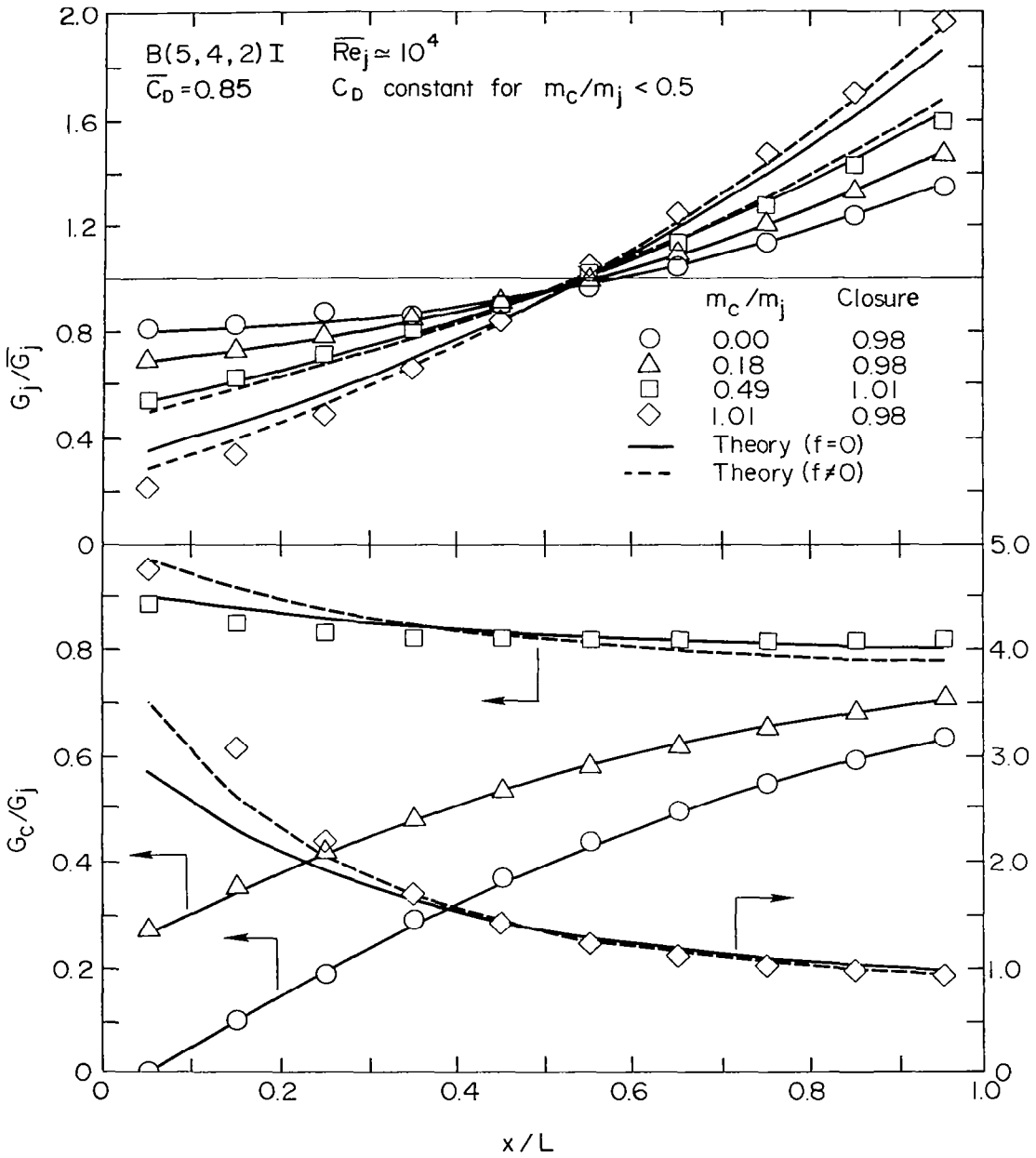

Fig. 4.9 Effect of initial crossflow on jet array flow distribution for B(5,4,2)I geometry - experimental data compared with predictive model.

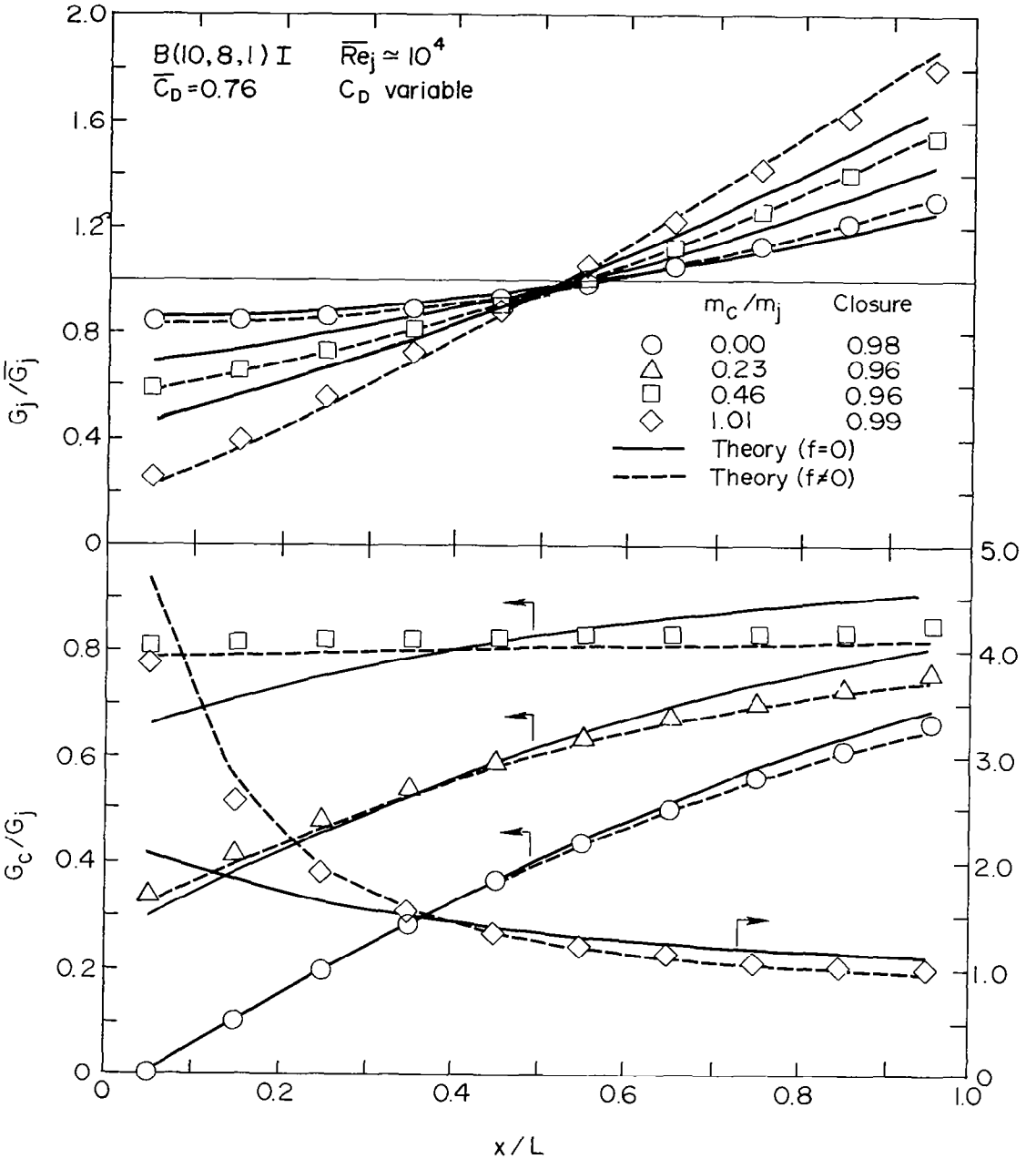

Fig. 4.10 Effect of initial crossflow on jet array flow distribution for B(10,8,1)I geometry - experimental data compared with predictive model.

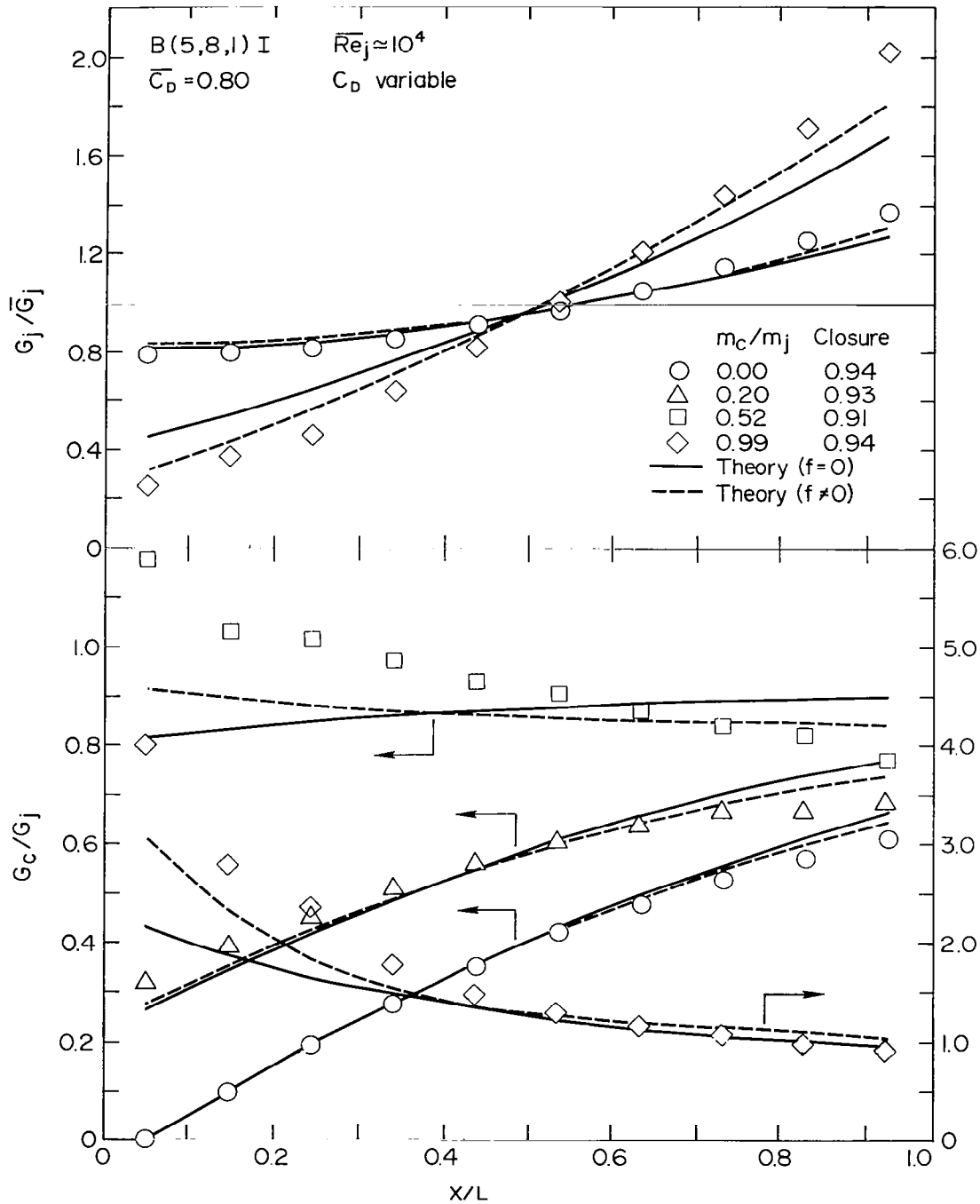

Fig. 4.11 Effect of initial crossflow on jet array flow distribution for B(5,8,1)I geometry - experimental data compared with predictive model.

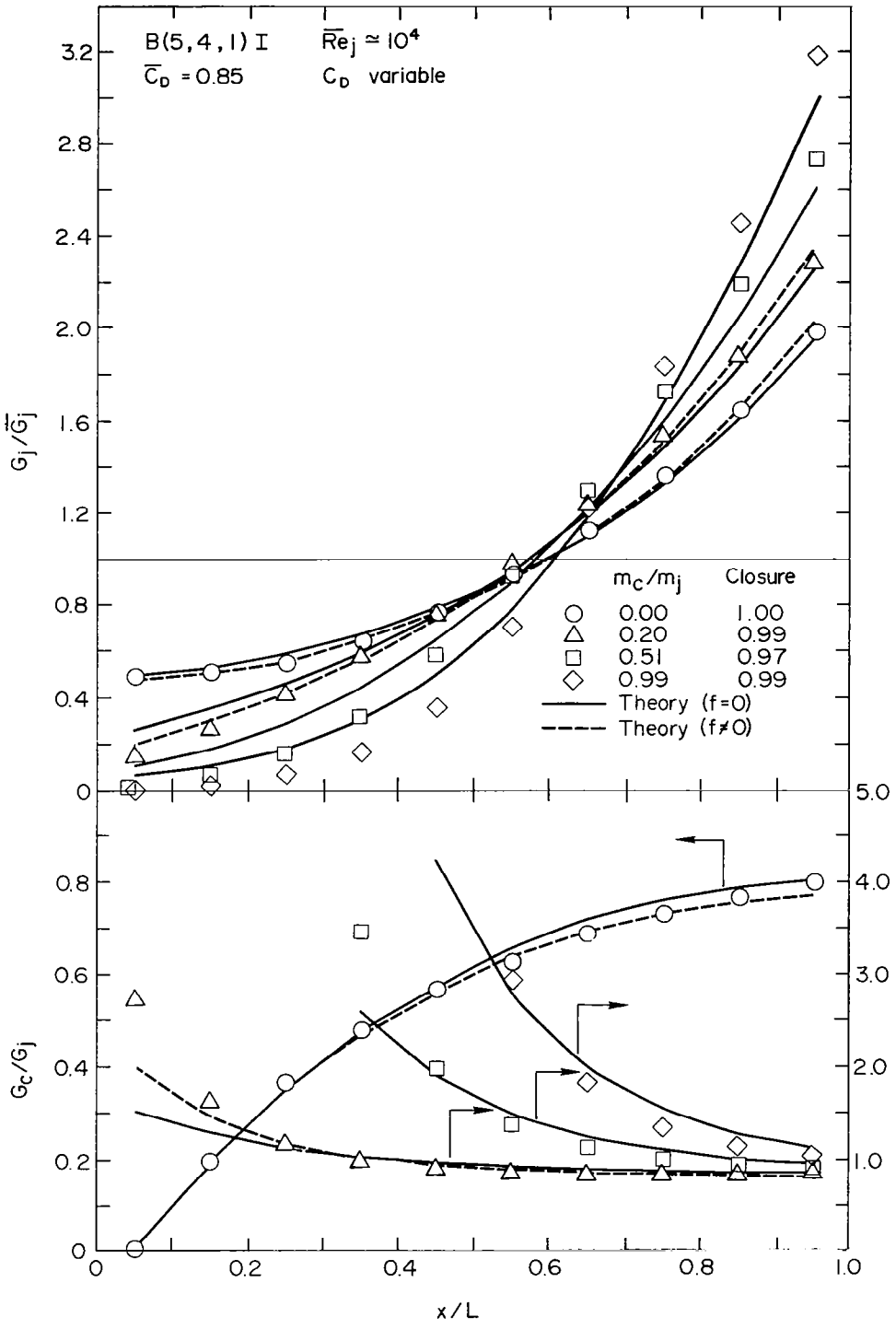

Fig. 4.12 Effect of initial crossflow on jet array flow distribution for B(5,4,1)I geometry - experimental data compared with predictive model.

cross-to-jet velocity ratio now varies, in general, in a nonlinear fashion and in all cases changes from a monotone increasing to a monotone decreasing function of streamwise location as m_c/m_j goes from zero to unity. For the (5,4,2) and (10,8,1) cases (Figs. 4.9 and 4.10) this transition occurs for a nominal value m_c/m_j of 0.5, while for the (5,8,1) case (Fig. 4.11) it occurs between 0.2 and 0.5, and for the (5,4,1) case (Fig. 4.12) it occurs before m_c/m_j has reached 0.2.

For all of these cases (Figs. 4.9 through 4.12), except (5,4,2) for $m_c/m_j < 0.5$, G_c/G_j reached values greater than the ''break point'' values at which C_D began to decrease (compare Fig. 4.3 and Table 4.1 or 4.2). However, the effect is minor for $m_c/m_j = 0$ and becomes significant more or less rapidly with increasing m_c/m_j depending on the particular geometry. With increasing m_c/m_j, G_c/G_j greatly exceeds unity at the upstream locations; and for the (5,4,1) case (Fig. 4.12) with $m_c/m_j = 0.5$ and 1, the jet flow at the first upstream row is essentially zero.

The effect of wall shear for the cases of Figs. 4.9 through 4.12 also becomes much more significant than for the previous cases. However, the effect is still minor with no initial crossflow present. Where the theory curves show little or no effect of friction, they are again quite consistent with the data. Where the theory shows a significant friction effect, the prediction including this effect generally agrees more closely with the data; and considering the complexity of developing a more precise accounting of wall shear effects for these flow fields, the agreement is quite satisfactory. The results with friction are particularly good for the (10,8,1) case (Fig. 4.10). For (5,8,1) (Fig. 4.11) the magnitude of the friction effect appears to be somewhat under-predicted. This may be due to the smaller streamwise flow development length between spanwise rows for this case, which is just one half that for the (10,8,1) case. Recall that the predictive model for the friction factor, Eq. (4.13), was written assuming a fully developed flow. It may also be noted, however, that the mass balance closures were, unfortunately, not quite as good for (5,8,1) as they were for (10,8,1).

For the cases with $(y_n/d)(z/d) \leq 8$ (Figs. 4.9 through 4.12), the sensitivity of the predictions due to uncertainties in the input parameters is the same as previously noted for $(y_n/d)(z/d) \geq 12$ (Fig. 4.6 through 4.8), except

for the first several upstream rows at the larger m_c/m_j, where the sensitivity is larger. For example, at the first row for $(y_n/d)(z/d) = 8$ (Fig. 4.9, 4.10 and 4.11), with $m_c/m_j = 1.0$, it is $\pm$ 12% for $G_j/\bar{G}_j$ and $\pm$ 16% for G_c/G_j. At the first row for $(y_n/d)(z/d) = 4$ (Fig. 4.12), with $m_c/m_j = 0.2$, it is $\pm$18% for $G_j/\bar{G}_j$ and $\pm$ 22% for G_c/G_j (Appendix B, Tables B.1 and B.2). For these conditions, the largest discrepancies between the predicted curves and the data points are also observed for the first row or two, the agreement, in general, quickly improving downstream. The discrepancies may be due to uncertainties, or to an inadequate friction factor model, or both.

It should be noted that predicted curves with friction are not indicated for (5,4,1) (Fig. 4.12) for $m_c/m_j = 0.5$ and 1. Because of singularities arising during iterations involved in the numerical solution technique these predicted results were not obtained. However, the position of the $G_j/\bar{G}_j$ curves for f = 0 (Fig. 4.12) relative to the data points fits the pattern shown by the results for the smaller initial crossflow ratios for which predicted curves with the friction effect are shown. In any event, this (5,4,1) geometry with any significant crossflow is not a good candidate for practical application since the jet flow rates at the upstream rows of holes are essentially nullified by the crossflow.

It is worthwhile to emphasize that the parameter $(y_n/d)(z/d)$ is proportional to the area ratio of the channel cross-section to the jet holes. Small values of this parameter result in large pressure drops along the channel relative to the pressure drops across the jet holes, leading, in turn, to highly nonuniform flow distributions. The reduction of the discharge coefficient with increasing crossflow may be viewed as an effective jet hole area reduction. Hence, the variable C_D effect tends to result in more nearly uniform flow distributions than would occur if the C_D were to remain constant at its value in the absence of a crossflow. On the other hand, the channel wall shear effect causes the flow distributions to be more nonuniform than they would be in its absence. Thus, it is possible that neglecting both the variable C_D and wall shear effects in the model could result in a prediction closer to the data than a prediction which neglects only one of the two effects.

The effect of mean jet Reynolds number magnitude on the flow distribution was tested using the B(10,8,1)I geometry. As discussed already, the wall

shear effect was not significant for the noninitial crossflow cases, but the effect becomes significant for the larger initial crossflow rates with the narrower channel heights. When the predictions begin to show a significant friction effect, the predicted flow distributions begin to show a dependence on $\overline{Re}_j$ [see Eq. (4.14)]. An additional test with the B(10,8,1) configuration was conducted at a low $\overline{Re}_j$ of about $5x10^3$. The data is compared with the model prediction in Fig. 4.13. The agreement is excellent just as it was for the $\overline{Re}_j \simeq 10^4$ test (Fig. 4.10).

To see clearly the parametric effect of $\overline{Re}_j$ on the flow distribution, the predicted flow distributions for B(10,8,1)I with $m_c/m_j = 1.0$, with and without friction effects at $\overline{Re}_j$ = 5,10, and 20K, are shown in Fig. 4.14. As $\overline{Re}_j$ decreases, the friction effect becomes more significant. However, the sensitivity to the Reynolds number magnitude is not very large except at the upstream rows where the percentage change in $G_j/\overline{G}_j$ and G_c/G_j starts to become significant.

Flow distributions for four additional configurations are shown in Figs. 4.15 through 4.18. The first three of these configurations (Figs. 4.5 through 4.17) are identical to the first three originally presented (Figs. 4.6 through 4.8), except for the decrease in x_n/d from 10 to 5. The model predicts that for C_D constant, negligible wall shear, and a fixed number of spanwise rows in the array, the flow distribution is independent of x_n/d, with $(y_n/d)(z/d)$ the only significant geometric parameter. The data in Figs. 4.15 through 4.17 verify this conclusion. One exception is the B(5,4,3)I case at $m_c/m_j = 1.0$ (Fig. 4.17), which falls outside the set of conditions just noted, due to a small variable C_D effect. The wall shear effect is noticeable but still negligible.] The last of these configurations, B(10,4,1)I in Fig. 4.18, shows a behavior similar to the B(5,4,1)I case of Fig. 4.12. Like that case, for $m_c/m_j = 0.5$, a predicted result with friction was not obtained. Also, like that case, the (10,4,1) geometry with any significant crossflow is not a good candidate for practical application since the jet flow rates at the upstream rows of holes are essentially nullified by the crossflow.

4.4.2 Pressure Profiles

The measured pressure distributions corresponding to several of

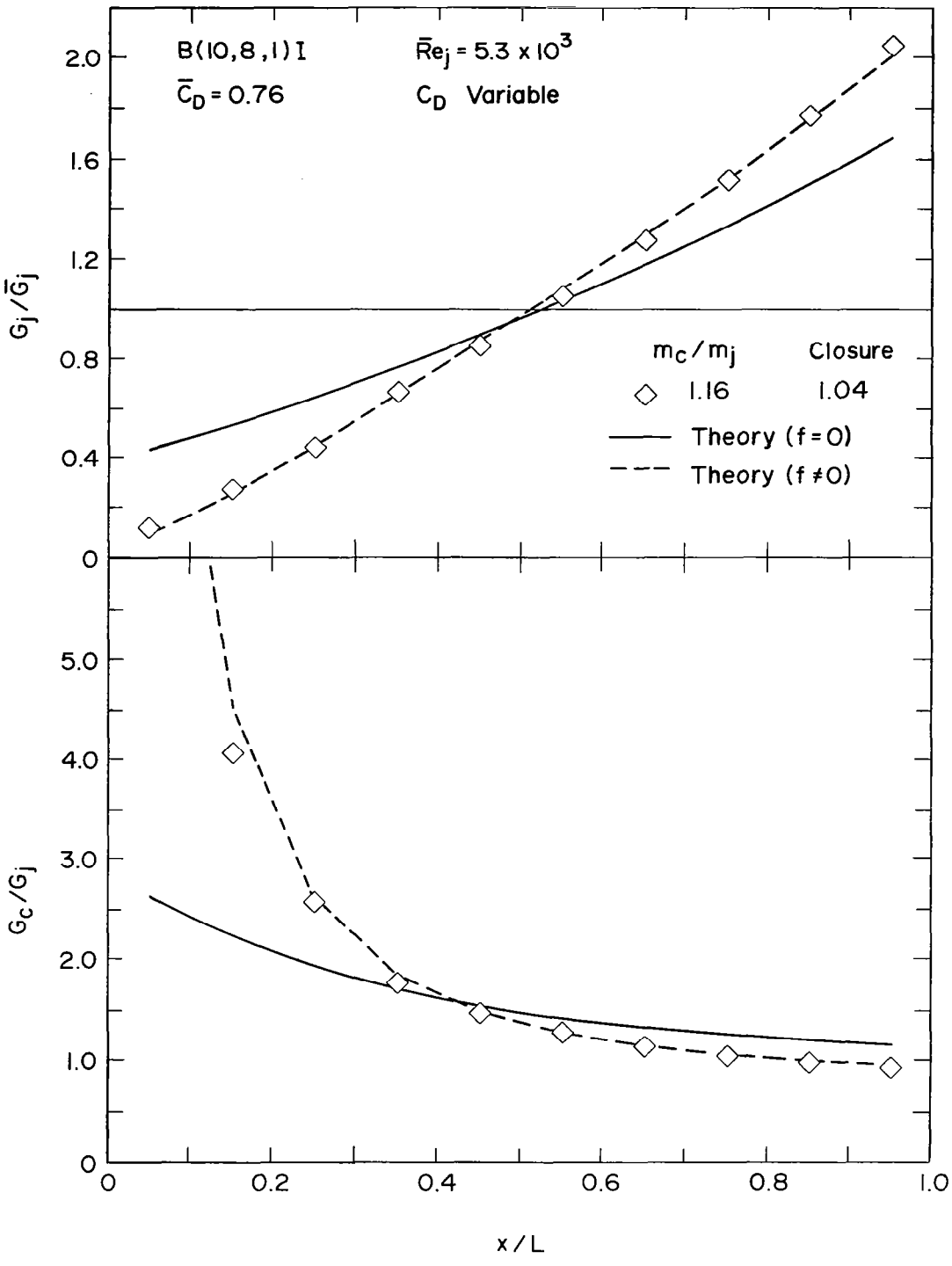

Fig. 4.13 Effect of mean jet Reynolds number on jet array flow distribution for B(10,8,1)I geometry - experimental data compared with predictive model.

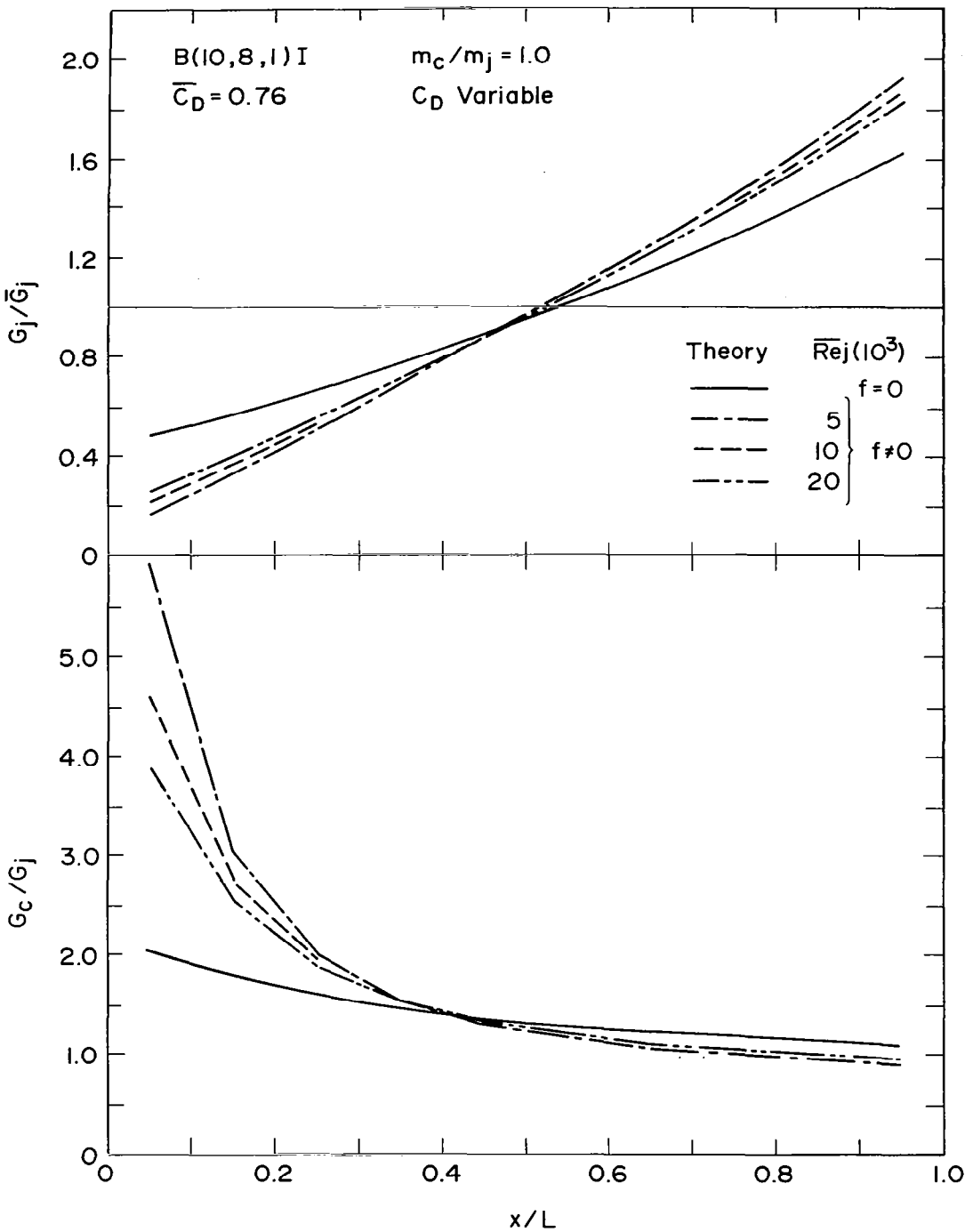

Fig. 4.14 Effect of mean jet Reynolds number on predicted flow distribution for B(10,8,1)I geometry.

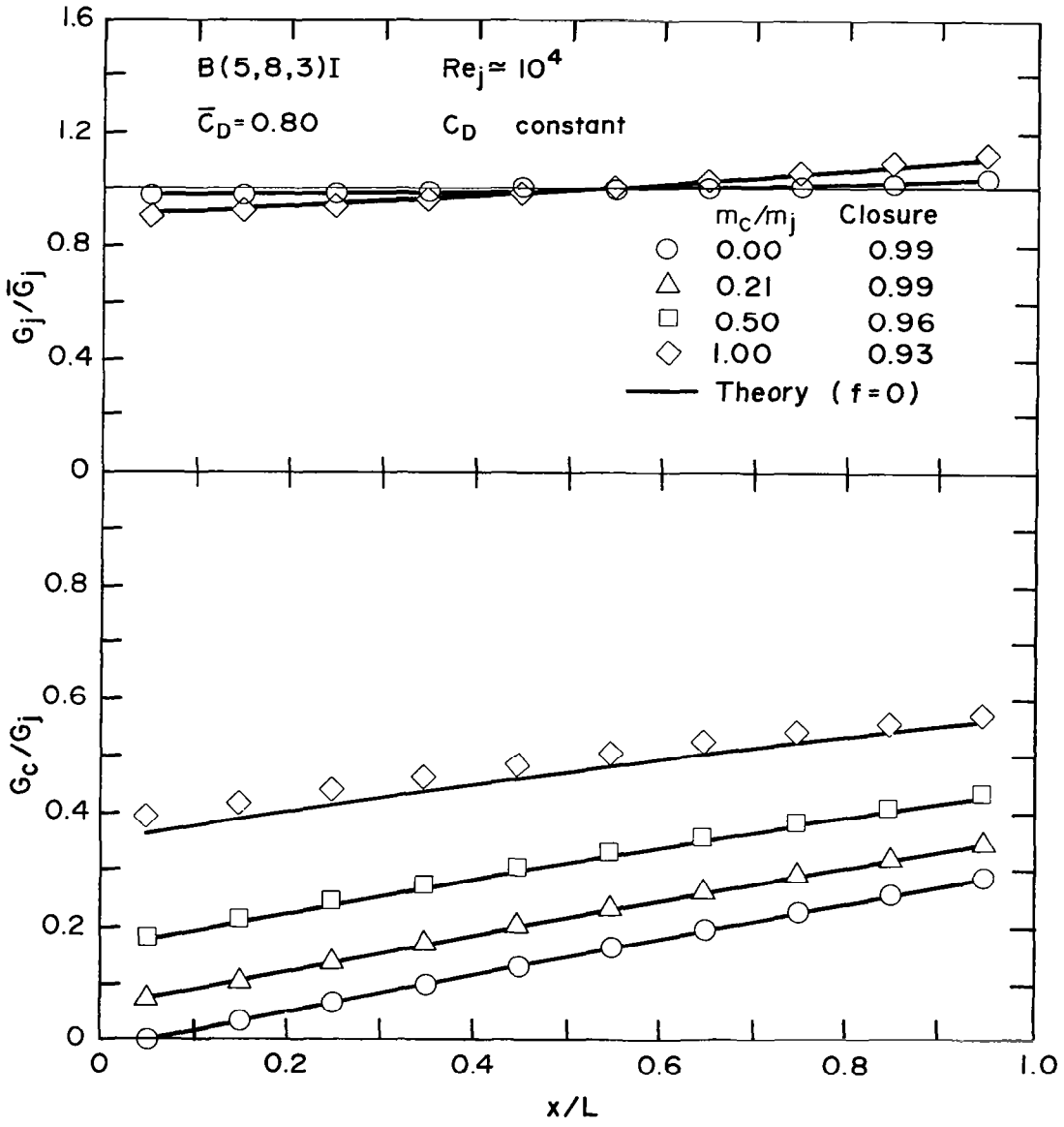

Fig. 4.15 Effect of initial crossflow on jet array flow distribution for B(5,8,3)I geometry - experimental data compared with predictive model.

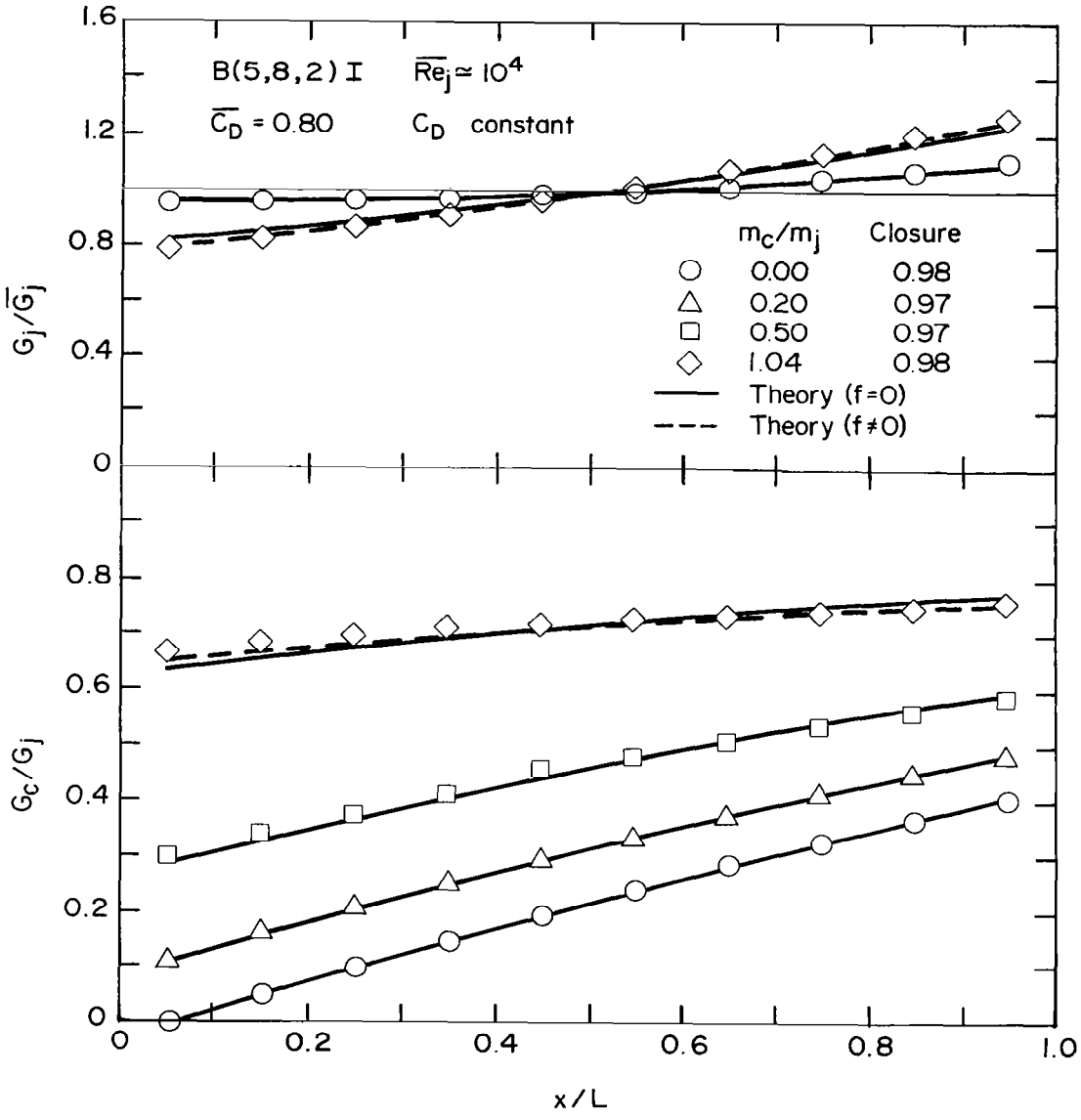

Fig. 4.16 Effect of initial crossflow on jet array flow distribution for B(5,8,2)I geometry - experimental data compared with predictive model.

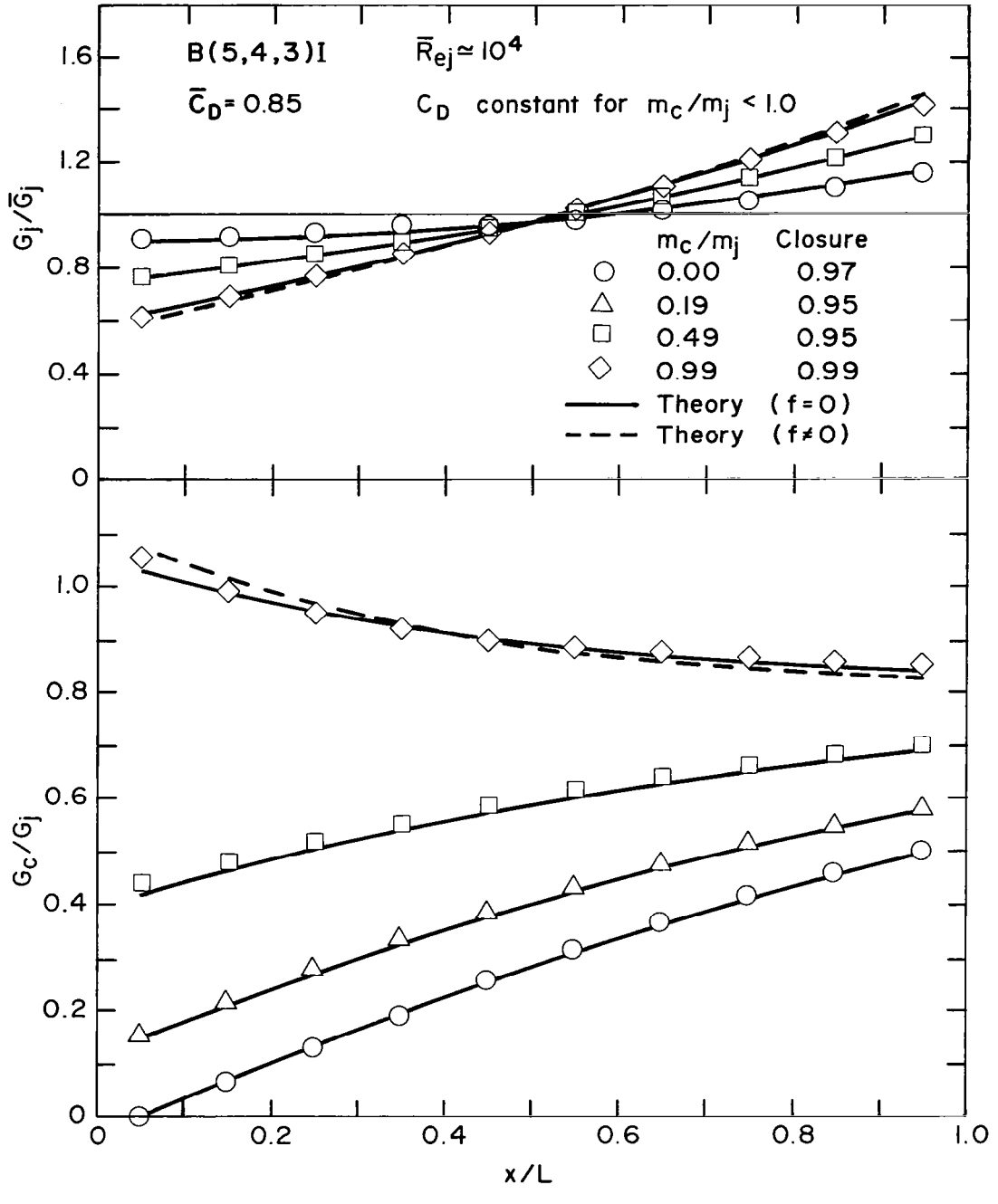

Fig. 4.17 Effect of initial crossflow on jet array flow distribution for B(5,4,3)I geometry - experimental data compared with predictive model.

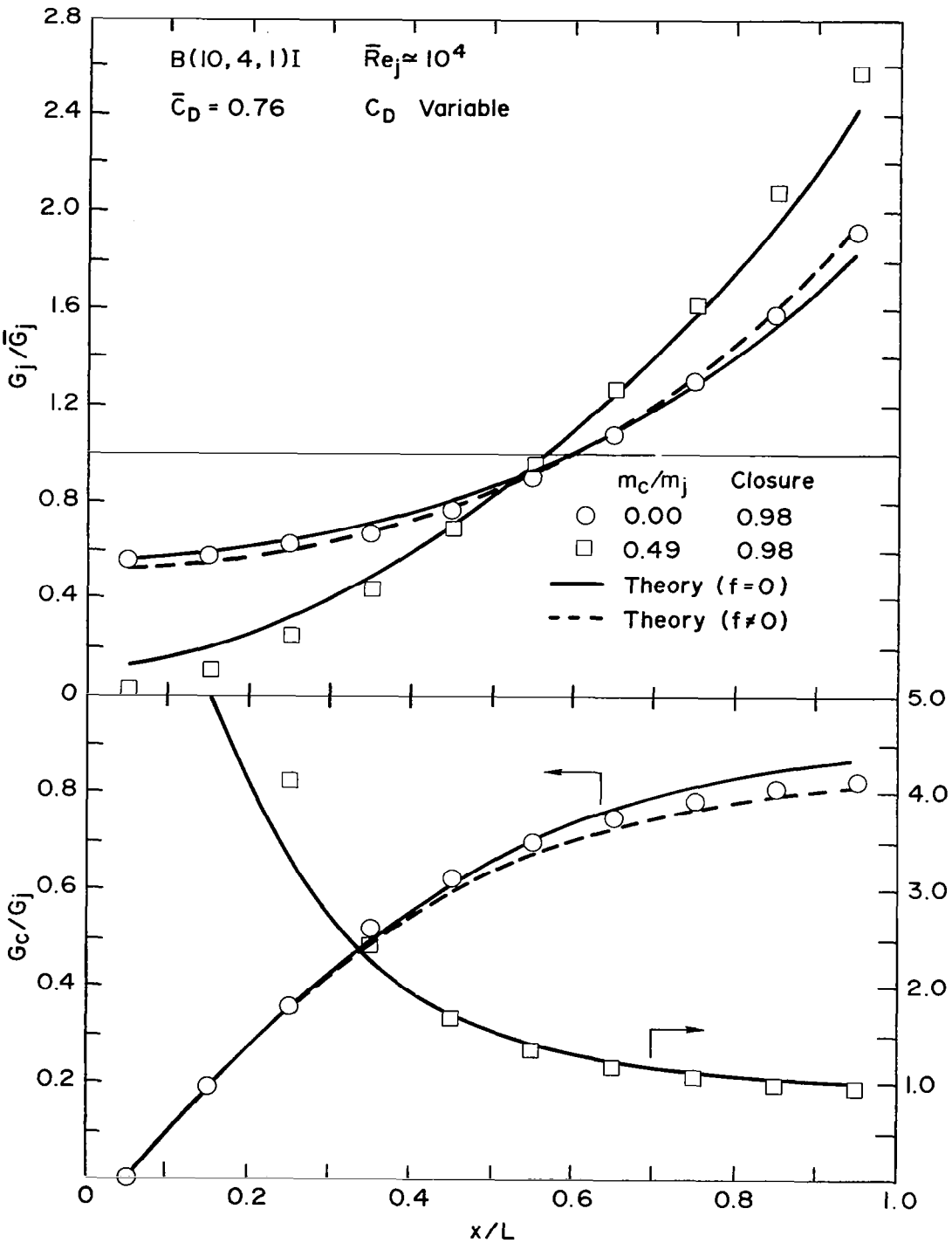

Fig. 4.18 Effect of initial crossflow on jet array flow distribution for B(10,4,1) geometry - experimental data compared with predictive model.

the cases for which flow distributions have been presented are shown in Fig. 4.19. These are typical and span the range from the most nearly uniform to the most nonuniform pressure distributions. The theoretical curves shown were computed from Eq. (4.1) using as input the solutions for $G_j/\bar{G}_j$ from the flow distribution model. This approach results in quite satisfactory predictions for the pressure distributions and therefore also for the overall pressure drop from the jet plenum to the jet array exit section.

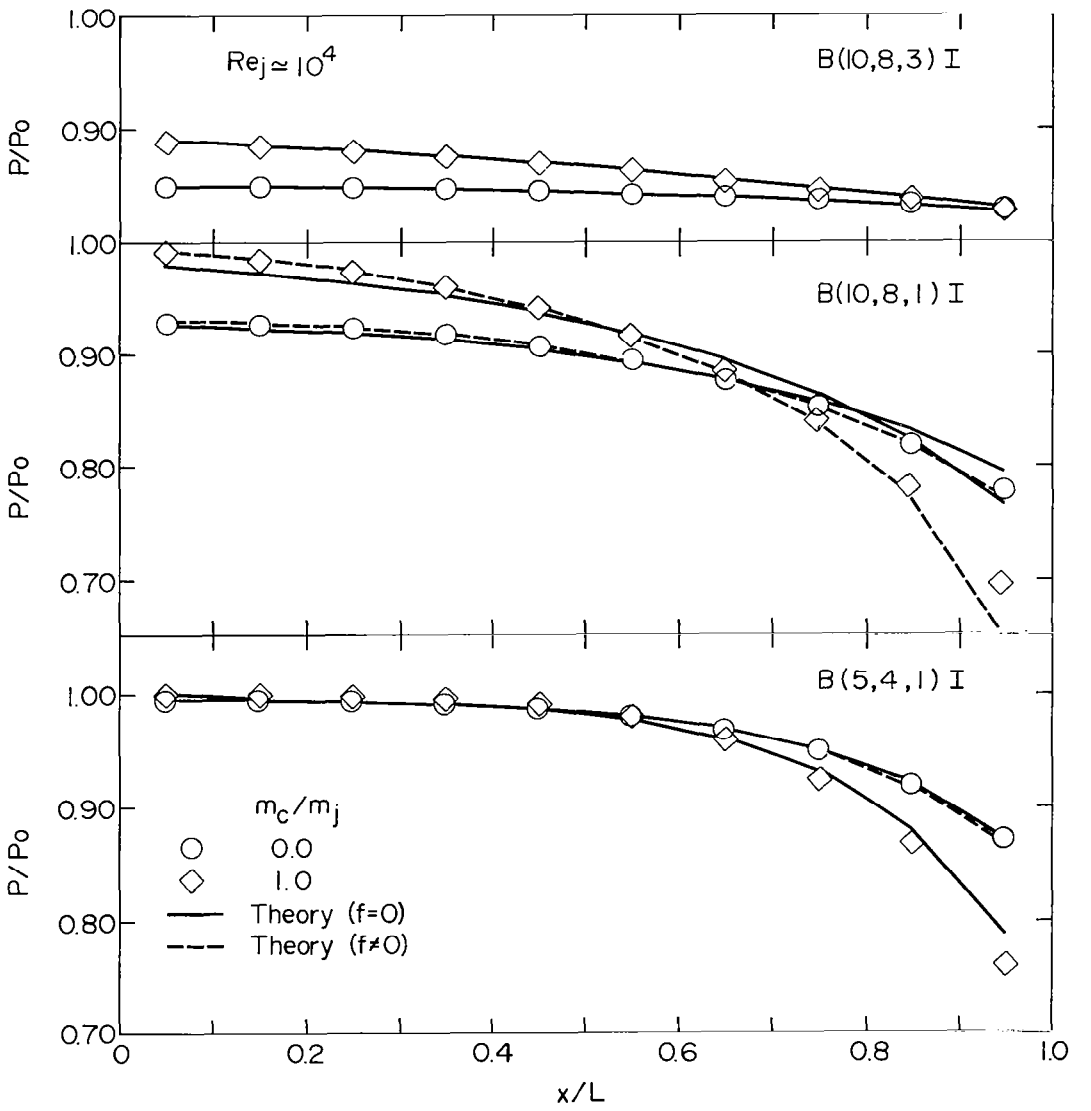

Fig. 4.19 Channel pressure profiles compared with predictive model.

5. HEAT TRANSFER CHARACTERISTICS WITH INITIAL CROSSFLOW

5.1 Impingement with Crossflow as a Three-Temperature Problem

The simplest and most frequently encountered convection heat transfer conditions can usually be treated in terms of two characteristic temperatures - a surface temperature and a fluid temperature (a two-temperature problem). Jet array impingement cooling with initial crossflow (Fig. 3.1) in which the initial crossflow temperature differs from that of the jets can be viewed as a three-temperature problem. This is a convection heat transfer situation where the surface heat transfer is to a fluid in the process of mixing from two different sources at two different temperatures. The best known example of a three-temperature situation is film cooling. In film cooling it is well known that the interaction of a secondary fluid stream with a primary stream affects not only the heat transfer coefficient, but also the value of the reference fluid temperature which drives the heat flux. In the simplest terms (Fig. 5.1):

$$q = h\,(T_s - T_{aw}) \tag{5.1}$$

where T_{aw} is the adiabatic wall temperature and is embodied in a non-dimensional effectiveness:

$$\eta = (T_{aw} - T_m)/(T_f - T_m) \tag{5.2}$$

The heat fluxes for jet array impingement with an initial crossflow can also be written as in 5.1, but T_{aw} is now expressed as the non-dimensional adiabatic wall temperature (effectiveness) in terms of T_j and T_c (Fig. 5.2):

$$\eta = (T_{aw} - T_j)/(T_c - T_j) \tag{5.3}$$

For jet impingement cooling it seems appropriate to identify the jet flow as the primary flow and the crossflow as the secondary flow. With this in mind, the form of the definition of η given in (5.3) for impingement cooling is

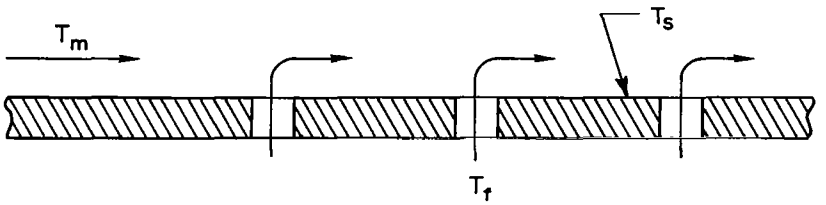

Fig. 5.1 Film cooling as a three-temperature problem.

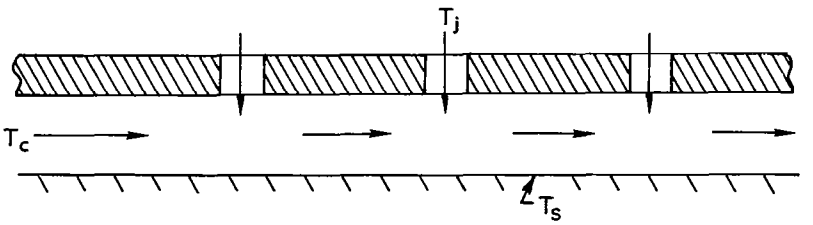

Fig. 5.2 Jet array impingement with initial crossflow as a three-temperature problem.

analogous to the established form utilized for film cooling. However, in the case of impingement it may not be appropriate to refer to this η as an ''effectiveness'' since in cases of practical interest in turbine impingement cooling it is desirable to have the jet flow dominating. This condition is reflected by η approaching zero.

It is useful to emphasize that (5.1) and (5.3) may be combined to give

$$q = h[(1 - \eta)(T_s - T_j) + \eta\ (T_s - T_c)] \qquad (5.4)$$

This form points up the fact that η is merely a ''temperature-difference weighting factor'', and for jet impingement with crossflow is perhaps best viewed in this manner.

In order to define the heat transfer characteristics (h, η) of a two-dimensional array of discrete impinging jets with an initial crossflow, it is necessary to characterize T_c and T_j. T_c is chosen to characterize the initial crossflow temperature at the entrance to the array portion of the crossflow channel (x = 0, Fig. 3.1). The entrance location is defined to be one-half a streamwise hole spacing upstream of the first spanwise row of holes in the array. This choice of entrance location is based on the fact that the array

heat transfer characteristics (h, η) are considered averaged across the span, but resolved in the streamwise direction to increments x_n, centered immediately opposite each spanwise row of holes. For low-speed flow T_c may be characterized by the mixed-mean temperature of the initial crossflow at the entrance to the array, while T_j may be taken as the mixed-mean fluid temperature at the jet exit plane.

However, for high-speed flow a somewhat generalized definition is necessary, just as in the case of film cooling [19]. T_c may be characterized as the adiabatic wall temperature at the array entrance, and T_j as the adiabatic wall temperature opposite the given jet row in the absence of an initial crossflow. In the case of low-speed flow, these values reduce to the mixed-mean temperatures previously indicated.

In cases of practical interest in turbine cooling the distinction indicated above in establishing T_c and T_j will not be particularly significant since differences between T_s and both T_c and T_j are quite large. However, for the experimental results to be reported herein these temperature differences were small (5 to 35 K) and with the relatively low laboratory air pressures utilized jet and crossflow velocity magnitudes in some cases may be rather high. Hence it was important to utilize the more general definition in reducing the heat transfer data obtained from the test runs.

5.2 Experimental Procedures and Data Reduction

Many details of the experimental procedures and data reduction techniques utilized for the initial crossflow tests were similar to or identical with those previously reported in [1]. Those details will be included here only as necessary with emphasis placed primarily on those additional features which were unique to the initial crossflow tests.

5.2.1 Standard Test Runs

A standard test run was initially defined by setting up a selected initial crossflow geometry (Section 3.1) with x_n/d, y_n/d, and z/d the primary geometric parameters as previously summarized in Table 3.1. The number of spanwise jet rows was always ten. The centerlines of these rows were always aligned directly opposite the spanwise centerline of segment numbers 20

through 29 of the test plate, counting from upstream (Fig. 3.2). Segments 1 through 19 formed the heat transfer surface of the initial crossflow channel, and segments 30 and 31 formed an extension of the heat transfer surface in the exit channel downstream of the array. Values of η and h, as defined by Eqs (5.1) and (5.3) [or by (5.4)] were determined for each segment opposite the array (20 through 29) as well as for segment 30 immediately downstream. Segment 31 was used as a guard element. Values of h could also be determined upstream of the array where $\eta = 1$ by definition.

Two separate sets of tests were required to determine these streamwise profiles of η and h for a given geometry, $\overline{Re}_j$, and flow ratio m_c/m_j. First, with the initial crossflow geometry, but with zero initial crossflow ($m_c = 0$), a set of tests was conducted to determine T_j, the characteristic temperature for jet flow alone, for each segment. These tests were conducted at three different steady-state conditions corresponding to three different power input levels to the segment heaters. A linear least squares fit to the three resulting data sets (q, T_s) for each of the segments under the jet rows (plus Segment 30) was used to determine the appropriate T_j for each segment from $q = h(T_s - T_j)$. In addition the fits result in streamwise resolved values of h for the array in the absence of initial crossflow.

Second, a similar set of three different power levels was conducted with the heated initial crossflow present. For the conditions of these tests, the adiabatic wall temperature of the initial crossflow at the entrance to tne array, used to characterize T_c, was essentially identical to the mixed-mean stagnation (i.e., total) temperature of the initial crossflow. This stagnation temperature was determined for each steady-state condition from the measured initial crossflow plenum temperature, combined with an energy balance over the initial crossflow channel:

$$T_c = T_o^c + \frac{1}{m_c c_p} \sum_{n=1}^{19} Q_n \qquad (5.5)$$

With T_j and T_c determined, a linear least squares fit to the three data sets (q, T_s) was used to determine the two unknowns h and η from Eq. (5.4) for each of the segments 20 through 30. Values of h in the initial crossflow channel were also determined using the adiabatic wall temperature at the given

segment as the reference temperature approximated by the local mixed-mean stagnation temperature again determined from an energy b lance.

Additional details relating to the test procedure will now be discussed. For each standard test run the jet flow rate (m_j) was set at the appropriate value to give a nominal $\overline{Re}j$ of 10^4. The jet plenum air temperature was normally at an ambient level of about 300K. For each geometry, the initial crossflow rate (m_c) was set, in turn, at the appropriate levels to give nominal values of m_c/m_j of 0.2, 0.5 and 1.0. Several iterations on the flow rate adjustments were sometimes required since the introduction of the initial crossflow increased the backpressure seen by the jet plenum, causing a slight reduction in the jet flow rate. As the final flow rate adjustments were being made the line heater just upstream of the initial crossflow plenum was energized in order to increase the initial crossflow air temperature above that of the jet air. The initial crossflow plenum air temperature was brought to a value approximately midway between the jet plenum temperature and the maximum value of the heat transfer surface temperature to be utilized (about 330 K).

The first steady-state condition was achieved with zero power input to the test plate segment heaters, and the segment temperatures were recorded. The entire test plate was then brought to a uniform temperature at the maximum value of about 330 K by individually adjusting the power input to each of the 31 test plate segment heaters. When this second steady-state condition was achieved, both the segment temperatures and the individual segment heater power inputs were recorded. The third and final condition was set with the heater power inputs cut to about half of their maximum values. Segment (surface) heat fluxes were determined from the measured power inputs suitably corrected for heat leaks [1]. Heat fluxes for the zero power input condition were not precisely zero because of these small but unavoidable heat leaks.

Test run procedures for the determination of T_j were also as outlined above except for the absence of the initial crossflow. Segments 1 through 18 were inactive with Segment 19 used as a guard element.

Results for η and h (in the form of Nusselt numbers) for the standard tests reported in Section 5.3 and Appendix D were essentially all obtained with the jet plate holder (Fig. 3.2) machined from Plexiglass in place in the

test rig. The only exceptions were the B(5,4,1)I geometry, the B(5,4,2)I geometry for the $m_c/m_j = 0.2$ test, and the B(5,8,3)I for the $m_c/m_j = 1.0$ test. For these the aluminum jet plate holder was in place. Use of the Plexiglass unit was preferred since it minimized the thermal coupling between the initial crossflow plenum and the jet plenum/jet plate assembly, and also minimized the heat leak through the upper surface of the initial crossflow channel. This heat leak was neglected in the energy balance on the initial crossflow channel, Eq. (5.5), used to determine T_c. Estimated on the basis of one-dimensional heat flow from the air in the initial crossflow channel through the jet plate holder to the surrounding ambient, the effect of this heat leak was negligible with either jet plate holder in place.

In several cases where test runs which had been completed with the original aluminum jet plate holder in place were repeated with the Plexiglass unit, some effect on the resulting η values was observed. This may have been due to axial heat conduction effects in the aluminum jet plate holder which may affect somewhat the energy balance and also the thermal boundary condition at the jet exit plane within the array. This thermal boundary condition might be expected to affect somewhat the adiabatic wall temperature (and therefore η) at the impingement surface within the array, while having negligible effect on the Nusselt numbers.

The observed effect on η was most apparent for smaller values where the jet flow dominates. It may be considered a secondary effect since temperature differences in the gas turbine application are such that for smaller values of η, the relation between q and T_s is not strongly sensitive to variations in η. Nevertheless, in future studies more attention should be paid to the control of the thermal boundary condition at the jet exit plane of the jet plate.

5.2.2 Experimental Uncertainties

The linear least squares fit based on Eq. (5.4) was actually carried out in the form

$$\frac{q}{T_s - T_c} = h(1 - \eta)\frac{T_s - T_j}{T_s - T_c} + h\eta \qquad (5.6)$$

with the coefficients $h(1 - \eta)$ and $h\eta$ determined directly from the fit. It is

clear from either Eq. (5.4) or (5.6) that only two independent test conditions are required to determine η and h. The use of three independent conditions provided additional confidence to the fit. As a measure of this confidence three values of η and of h were also computed using each of the three possible combinations of two members of each data set (zero/maximum, zero/half, and half/maximum power input conditions). These values were then compared with the original values of η and h based on the linear least squares fit to all three data sets.

Considering all standard test runs with initial crossflow present, 95% of the values of h computed from two members of each set deviated by less than $\pm$ 3% of the values based on the fit. For η the result was $\pm$ 7% with most of the larger deviations coming at downstream rows where the η values were smaller. The total number of values compared for both η and h was 1188 (12 geometries x 3 initial crossflow rates x 11 segments x 3 values from each three member set). For the zero initial crossflow tests 95% of the h values were within $\pm$ 2%.

The percentage deviations noted above provide some indication of the uncertainty associated with the η and h results. Experimental uncertainties must be at least as large as these values. Composite uncertainties for η and Nu were also calculated by the method of [13]. Input uncertainties were estimated at $\pm$ 1% to $\pm$ 2% for the heat fluxes, $\pm$ 0.25 K for $(T_s - T_c)$, $\pm$ 0.1 K for $(T_s - T_j)$, and $\pm$ 1% for d as it enters the Nusselt number calculated from h. $(T_s - T_j)$ values depended only on differences between measurements made with the same thermocouple, whereas $(T_s - T_c)$ values depended on the difference between measurements from two different thermocouples plus an energy balance. The calculated η and Nu composite uncertainties varied depending on the particular conditions but for Nu within the array most conditions result in values of $\pm$ 6% or less. For η the composite uncertainties, expressed on a percentage basis, vary more widely depending on conditions, from about $\pm$ 2 to $\pm$ 4% for η values near unity to as much as $\pm$ 20% for a downstream value as low as 0.1. Overall, the calculated composite uncertainty ranges appear consistent with the percentage deviations from the least squares fit lines summarized in the preceding paragraph.

5.2.3 Special Test Runs

Several special test runs were conducted to examine the sensitivity of the results to changes in certain parameters or conditions normally held constant during the standard test runs. These included the effect of $\overline{Re}_j$, the value of the initial crossflow plenum temperature relative to the jet plenum temperature, and the effect of the thermal entrance length (test surface thermal boundary condition) in the initial crossflow channel upstream of the array. Otherwise the procedures for the special runs were the same as for the standard runs. With the B(5,8,3)I geometry at $m_c/m_j = 0.51$ tests were conducted for $\overline{Re}_j = 10^4$ (standard test run value) and also for a larger $\overline{Re}_j$ (1.81×10^4). The results for η and h are compared in Fig. 5.3. The h values are plotted as Nusselt numbers normalized by $\overline{Re}_j^{0.73}$ for direct comparison. The exponent on $\overline{Re}_j$ is from the jet array impingement correlation previously reported [2,11]. The η values appear to be relatively insensitive to $\overline{Re}_j$, while the Reynolds number dependence from the prior correlation appears to account quite well for the Nusselt number variation. The differences in the η values, though small, appear to increase downstream. This may be due to the existence of larger experimental uncertainties for smaller η values or a possible effect of the thermal boundary condition at the jet exit plane on the adiabatic wall temperature at the heat transfer surface.

With the B(5,4,3)I geometry at $m_c/m_j = 0.84$ two otherwise identical test runs were conducted, one with the initial crossflow plenum temperature set at a value such that the initial crossflow-to-jet plenum temperature difference was one-third of the maximum surface-to-jet plenum difference, the second with the initial crossflow plenum temperature increased such that the fractional difference was two-thirds. The results for both η and Nu were in agreement to well within experimental uncertainty, providing additional confidence that these coefficients were independent of the temperature differences.

The B(5,4,3)I geometry at $m_c/m_j = 0.2$ and 1.0, and the B(5,8,3)I geometry at 1.0 were tested with test plate segments 1 through 9 at zero heater power inputs for each of the three steady state conditions comprising a complete test run. This cut the isothermal portion of the entrance length upstream of the array from 15.8 to 8.3 hydraulic diameters (and from 38 to 20 in terms of streamwise hole spacings). The available hydrodynamic entrance length

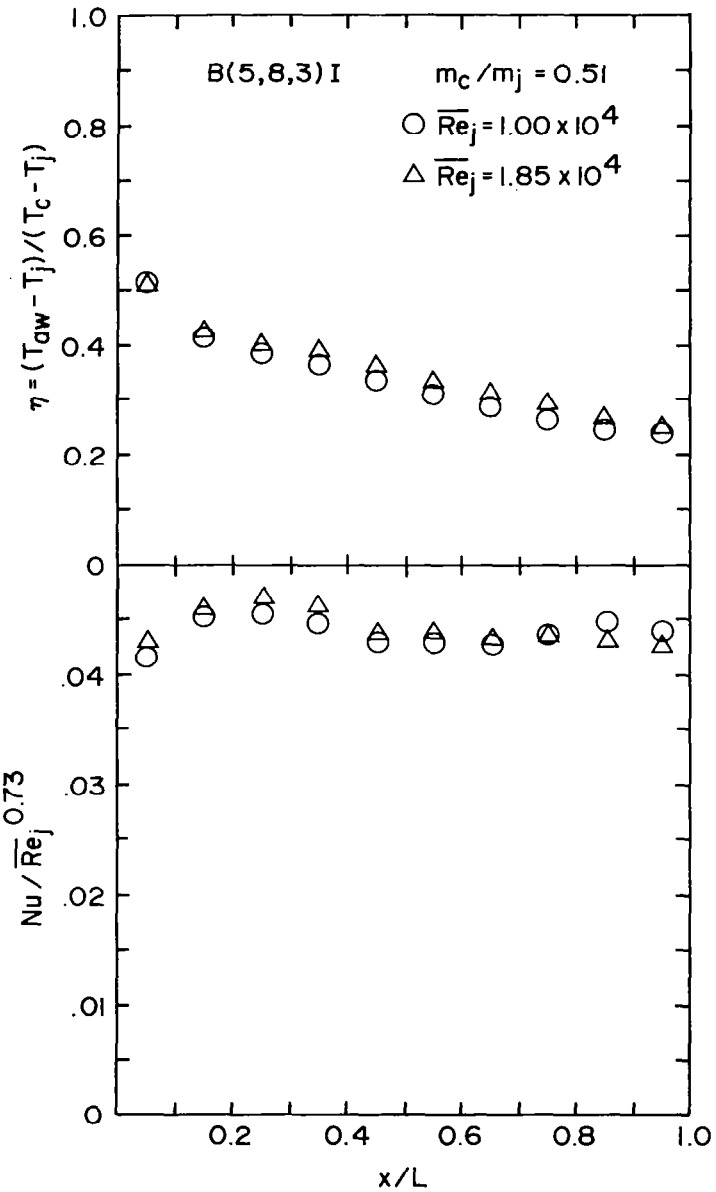

Fig. 5.3 Effect of mean jet Reynolds number on η and Nu.

remained constant at 15.8 hydraulic diameters or 38 hole spacings. Again, the results for both η and Nu remained unchanged to well within experimental uncertainty.

5.3 Results and Discussion

A complete set of η and Nu profiles for the standard test runs will be presented and discussed shortly. First, however, the heat transfer coefficients in the initial crossflow channel immediately upstream of the jet array section will be considered.

For all standard test runs reported here the entrance length and the width (span) of the initial crossflow channel were fixed, as was the width of the heat transfer test plate (Table 3.1). The entrance length (Le) (measured) in terms of hydraulic diameters ($D_h = 2z$) varied with the channel height z set for the particular test. Measured to the center of Segment 19, the first segment upstream of the jet array, Le/D_h ranged from 15.4 to 92.5. The aspect ratio of the channel cross-section also varied with z, and ranged from 24 to 144. The corresponding aspect ratio of the cross-section reckoned with respect to the width of the test plate varied from 16 to 96. Hence, both hydrodynamic and heat transfer edge effects could be considered negligible, and the configuration closely approximated an infinite parallel plate duct with asymmetric heating such that the primary heat transfer surface was isothermal while the opposing surface was essentially adiabatic. Some prior measurements for heat transfer with turbulent flow under similar conditions are available in the literature [20,21]. For the present test, initial crossflow channel Reynolds numbers (Re_c) ranged from 4×10^3 to 4×10^4. Nominal values of Re_c ($\sim 10^4$ and 2×10^4) for a number of test runs happened to match fairly closely with the values at the ends of the range covered by Tan and Charters [21], 9.5×10^3 to 2.12×10^4. Their test results, which included the entrance length, were for a 4.75 cm high rectangular duct with an aspect ratio of 3 with one large side heated. Channel Nusselt numbers (hD_h/k) at Segment 19 from the present tests are compared with their results in Fig. 5.4. Nusselt number values for the present tests were adjusted somewhat according to $Re_c^{0.8}$ in order to compare directly to the Tan and Charters' data. The two

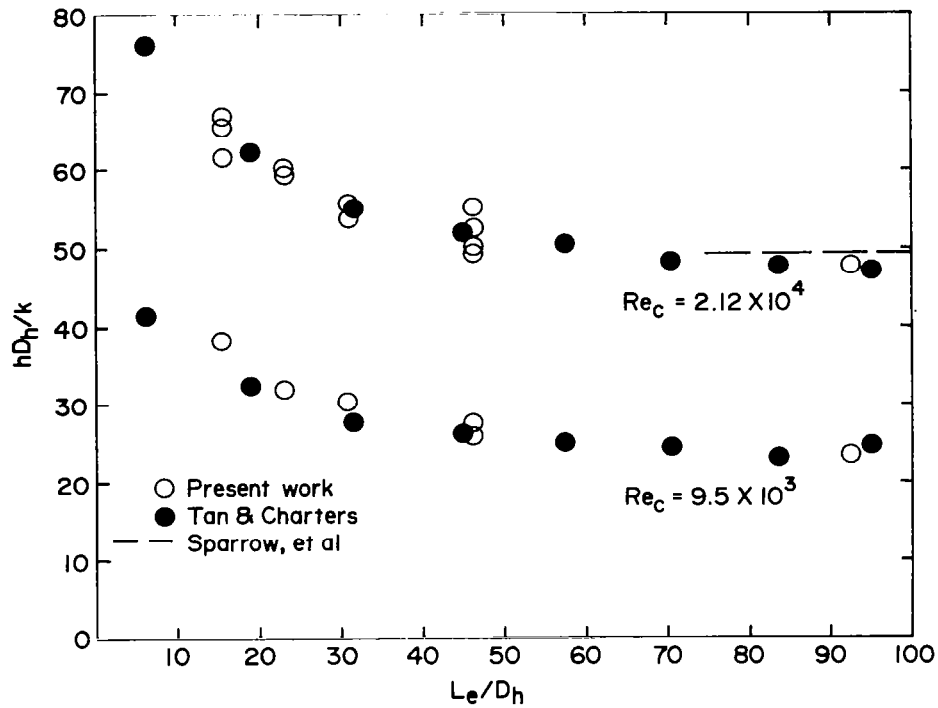

Fig. 5.4 Nusselt numbers in initial crossflow channel at entrance to jet array compared with prior data from literature.

sets of results are seen to be quite consistent. A fully developed Nusselt number magnitude based on the data of Sparrow, et al. [20] for a 5:1 aspect ratio duct heated on one large side only shown in Fig. 5.4 is also seen to be quite consistent. The data point utilized from Sparrow, et al. was at $Re_c = 1.85 \times 10^4$ with the Nusselt number also adjusted according to $Re_c^{0.8}$ for direct comparison in the Figure.

As already pointed out in Section 5.2.1, the initial crossflow reference temperature utilized in defining the heat transfer coefficients was the mixed-mean stagnation temperature. This was used as a suitable approximation to the adiabatic wall temperature. It was shown experimentally by McAdams, et al. [22] that for duct flows at subsonic velocities the heat transfer coefficient defined on the difference between the temperature of the heated wall and adiabatic wall temperature is independent of this difference. They also showed that for such flows preferred values of the recovery factor lie in the range 0.875 to 0.905. Using a recovery factor of 0.89 it was determined that

for the present tests the difference between the stagnation temperature and the adiabatic wall temperature at the end of the initial crossflow channel was normally less than 0.1 K, and always less than 0.2K. Hence, the use of the stagnation temperature as satisfactorily representing the adiabatic wall temperature is justified for the conditions of these tests.

We now return to the results for heat transfer characteristics in the jet array impingement region with the presence of an initial crossflow at a temperature different from the jet temperature. Standard test series results for twelve different geometric configurations are presented in Figs. 5.5 through 5.16, with one configuration represented by each figure. Corresponding tabular results are included in Appendix D, Table D.2. Each figure shows streamwise profiles of η and Nu resolved to one streamwise hole spacing. η and Nu are paired in each figure to emphasize that, in general, in order to appropriately relate the heat flux to the surface and characteristic fluid temperatures both parameter values are needed. The total jet flow rate, m_j, was fixed such that the mean jet Reynolds number for the array was fixed nominally at 10^4 for each case. For each geometry profiles are shown for m_c/m_j at nominal values of 0.2, 0.5, and 1.0. Nusselt number profiles for the initial crossflow configuration, but with $m_c = 0$, are also shown as a reference or baseline case for comparison. Since each array had ten spanwise rows of holes, each profile includes ten points within the array proper, with three additional points included for the initial crossflow channel immediately upstream of the array and one point immediately downstream. The first eleven figures are for inline arrays and the twelfth is for a staggered array.

Consider first Figs. 5.5 through 5.10. These all have $x_n/d = 5$, and are arranged in order of decreasing value of the parameter $(y_n/d)(z/d)$. This means the corresponding jet flow distributions range from highly uniform to highly nonuniform (Section 4.4). Examine first the values of η. In general, η decreases with increasing x/L and decreasing m_c/m_j. These trends simply reflect the increasing influence of the jet flow. It may be emphasized that since the crossflow temperature was characterized by its value at the entrance to the array, the value of η at a specific row reflects the influence of the jet flow introduced at all upstream rows as well as that of the row in question. Of particular note is the fact that overall, the η values within

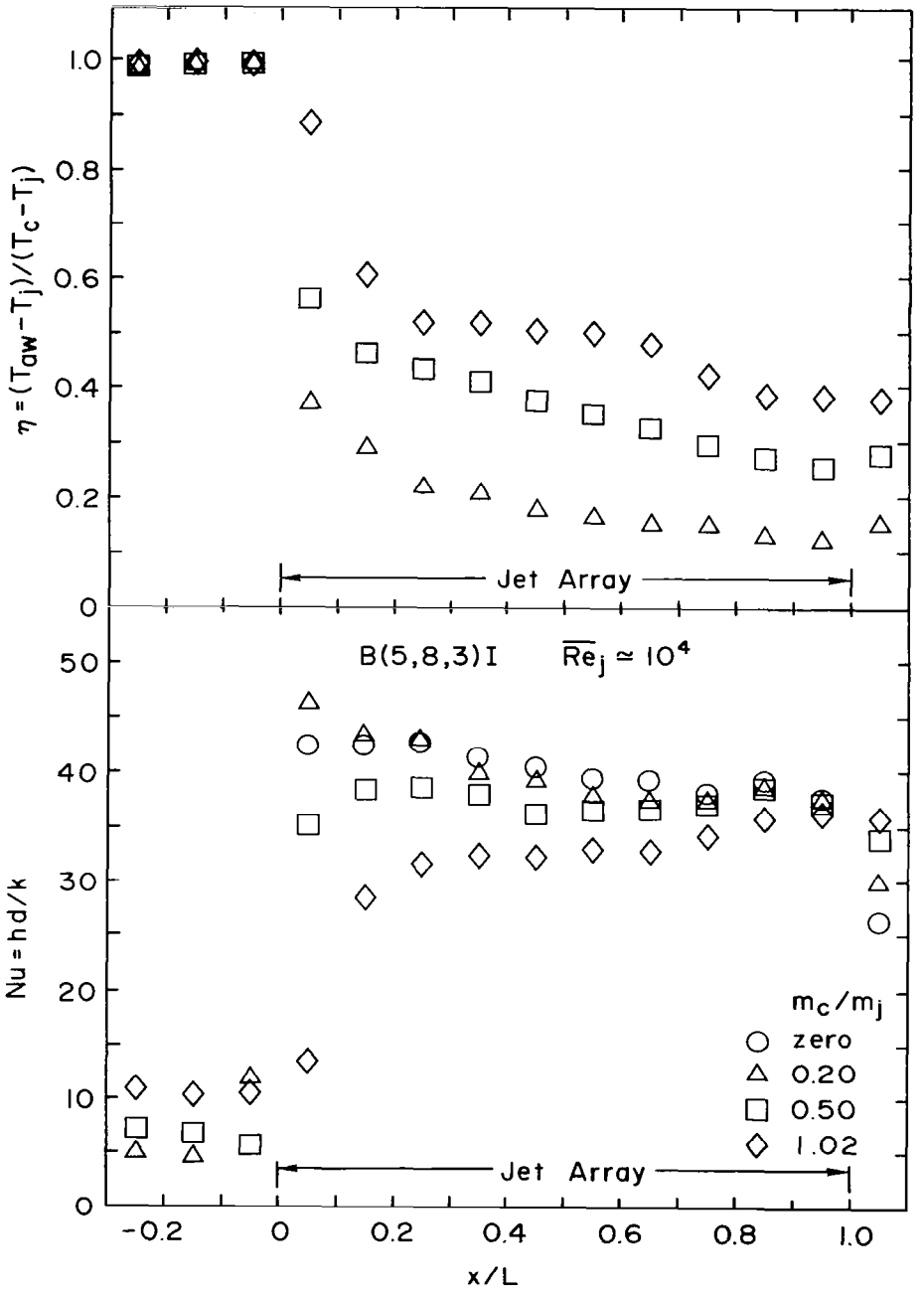

Fig. 5.5 Effect of initial crossflow rate on η and Nu profiles for B(5,8,3)I geometry.

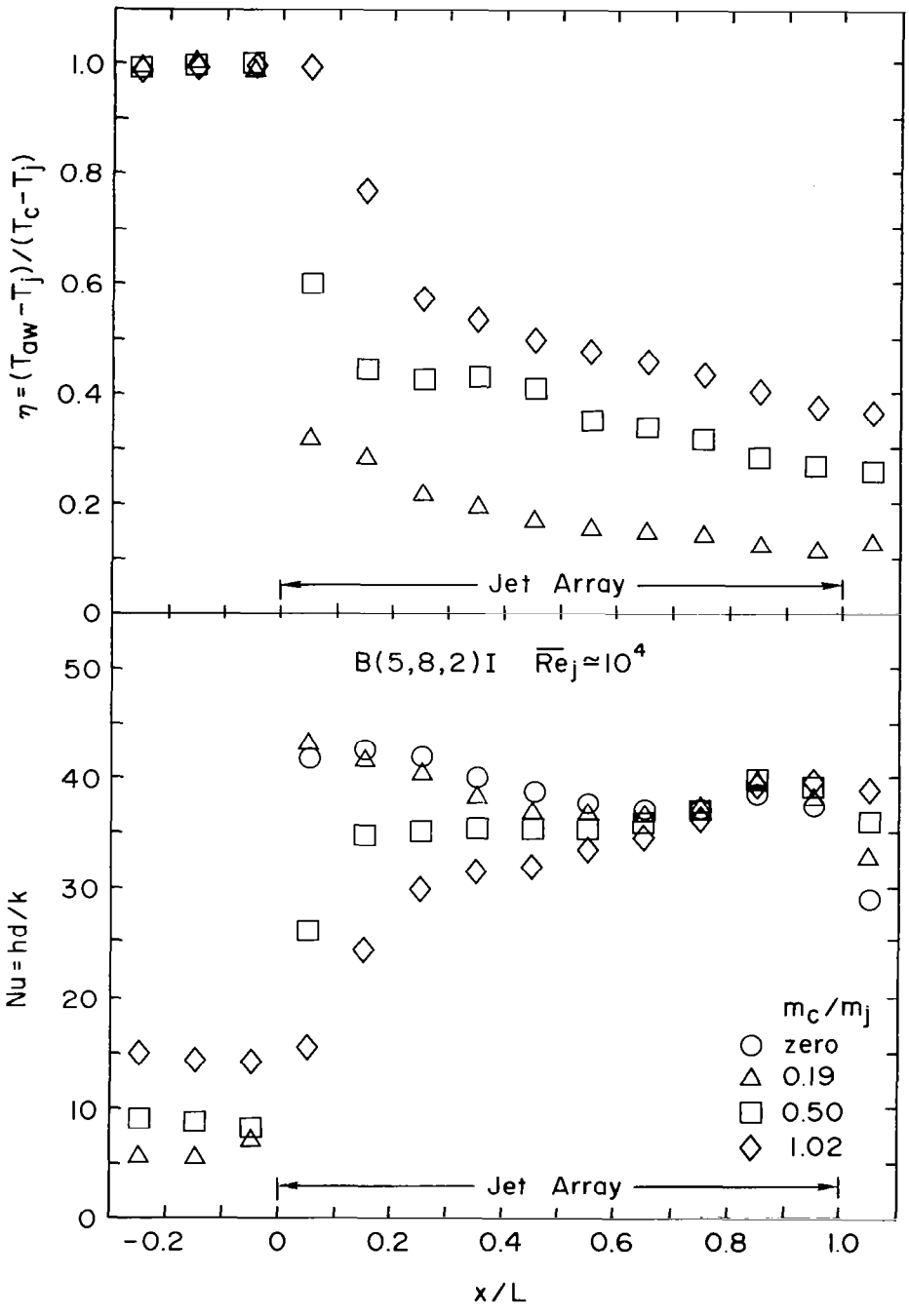

Fig. 5.6 Effect of initial crossflow rate on η and Nu profiles for B(5,8,2)I geometry.

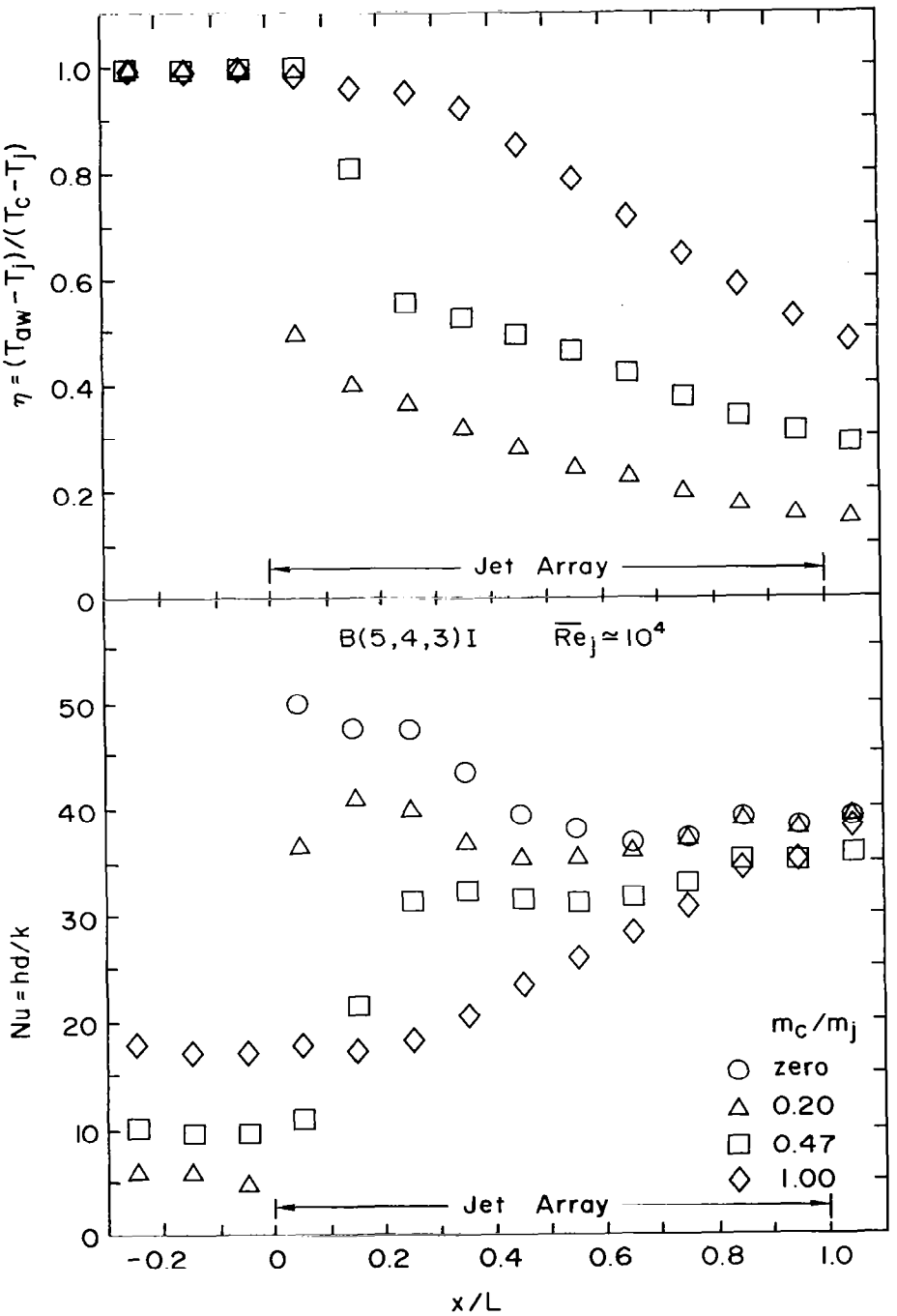

Fig. 5.7 Effect of initial crossflow rate on η and Nu profiles for B(5,4,3)I geometry.

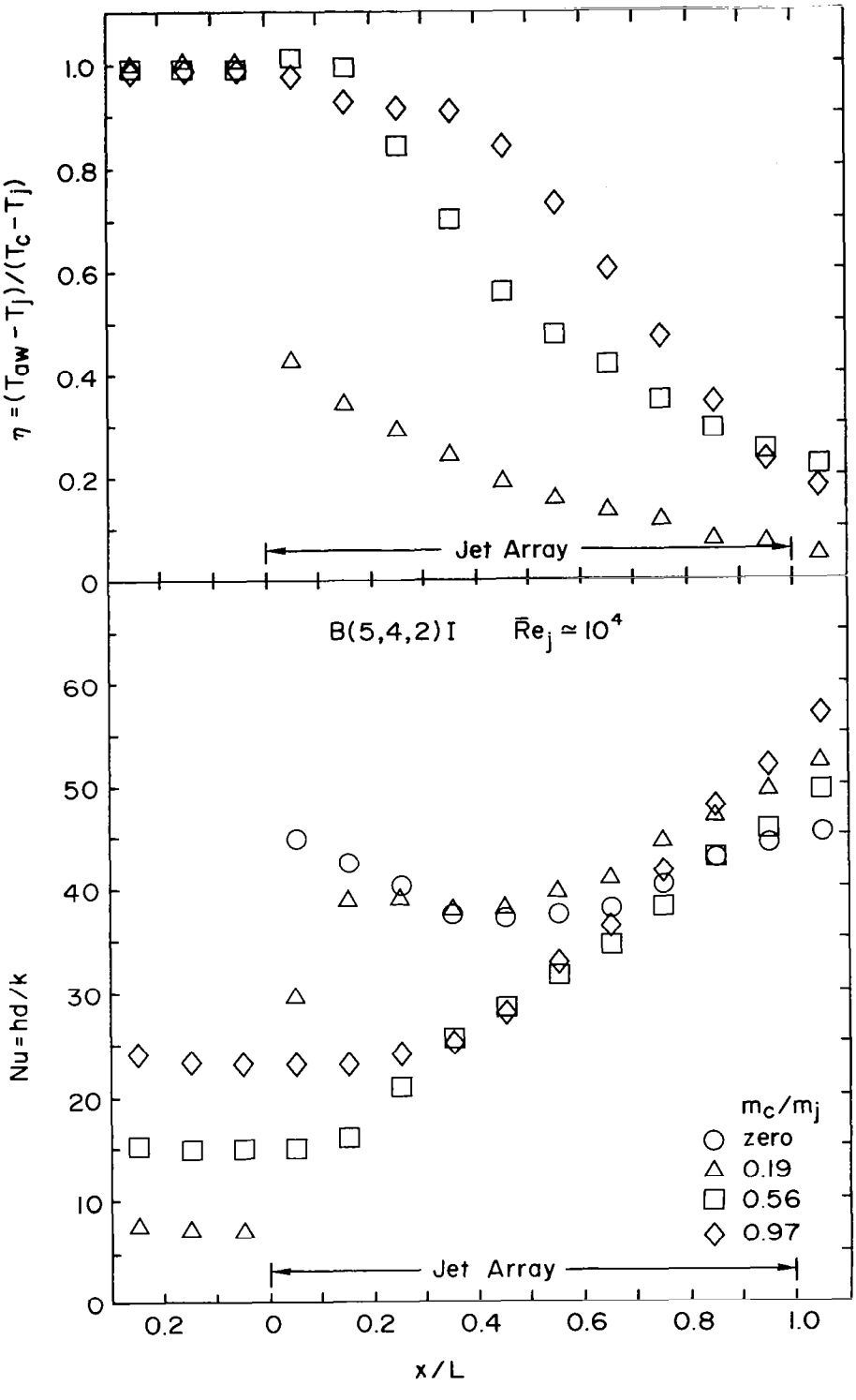

Fig. 5.8 Effect of initial crossflow rate on η and Nu profiles for B(5,4,2)I geometry.

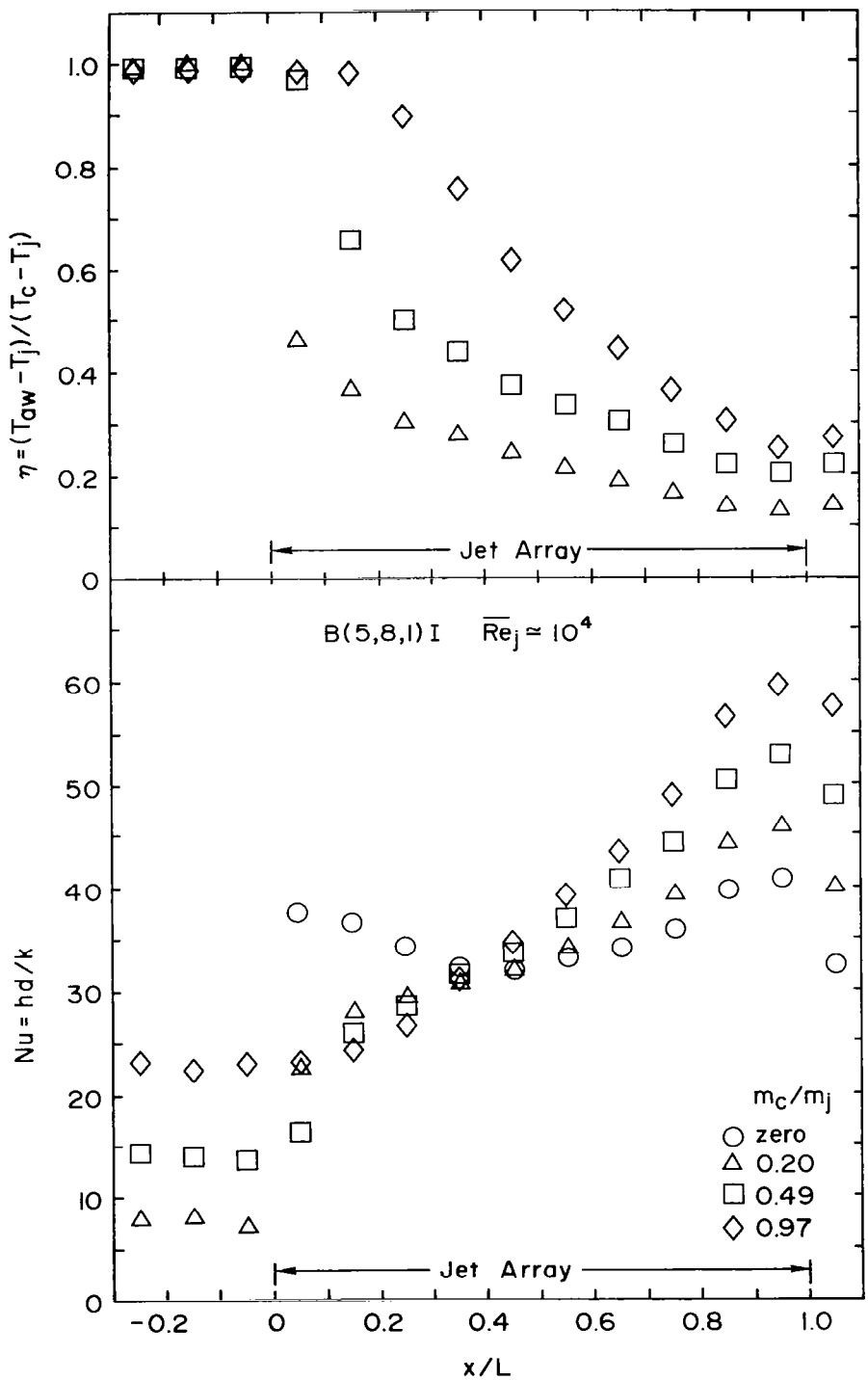

Fig. 5.9 Effect of initial crossflow rate on η and Nu profiles for B(5,8,1)I geometry.

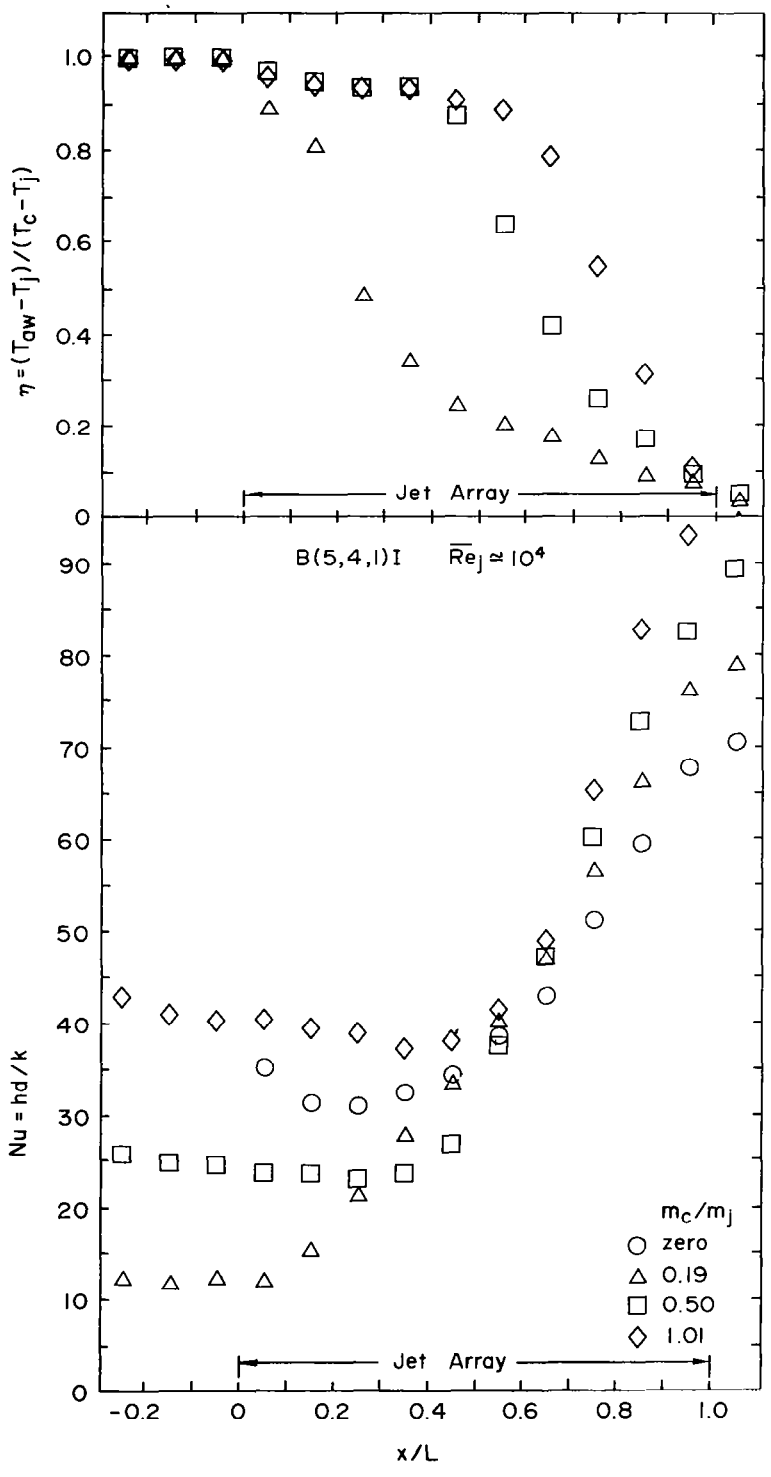

Fig. 5.10 Effect of initial crossflow rate on η and Nu profiles for B(5,4,1)I geometry.

the array span the range from unity to nearly zero (less than 0.1), and in the most extreme case (Fig. 5.10) cover this range for a single configuration. This case also has a highly nonuniform flow distribution (Fig. 4.12). Note that here the effect of initial crossflow not only penetrates into the array, but essentially dominates ($\eta \simeq 1$) at the first row for all m_c/m_j; and for $m_c/m_j = 0.5$ and 1.0, dominates over halfway through the array. This dominance can also be seen by examining the Nu profiles for this case which remain essentially at their upstream initial crossflow channel levels well into the array. This behavior is quite consistent with the very large cross-to-jet mass velocity ratios which were observed to persist well into this array (Fig. 4.12).

Returning to Fig. 5.5 a contrasting behavior is observed corresponding to a more nearly uniform flow distribution (Fig. 4.15). Here η has already dropped to nearly one-half at the first row, except for $m_c/m_j = 1.0$, where this occurs at the second row. Similarly, the strong immediate influence of the jets is reflected in the very large increase in Nu from immediately upstream of the array to the very first row of jets (excepting the $m_c/m_j = 1.0$ case in which the change is again less pronounced). It is interesting to note that at the first row an increase of G_c/G_j (Fig. 4.15) from 0.2 to 0.4 causes a reduction in Nu by a factor of more than two-and-one-half, while the increase from 0 to 0.2 causes essentially no change. It is possible that at the larger value of G_c/G_j the impingement points of the jets are displaced downstream by $x_n/2$ or more and thus provide little cooling of the area $0 \leq x \leq x_n$ associated with the first row. This explanation is reinforced by examining the Nu values immediately downstream of the array. For $m_c/m_j = 1.0$ this Nu value is 3.5 times the value upstream of the array though the downstream crossflow Reynolds number would be just twice that upstream of the array. This indicates that the jets in the last row of the array must be displaced enough to be impinging on the surface segment immediately downstream of the array. Also, for these inline hole patterns the crossflow tends to be channeled between the streamwise jet rows, so the downstream rows tend to be ''protected'' somewhat from the crossflow, whereas the first upstream row is subjected to a spanwise uniform initial crossflow, and not partially ''protected'' (compare prior discussion [1,9]).

The trends discussed above as contrasted between that configuration having the most nearly-uniform flow distributions, Fig. 5.5, and that having the most highly nonuniform flow distributions, Fig. 5.10, may be examined for the intermediate cases, Figs. 5.6 to 5.9, and seen to fit within the same general pattern. Reference may be made to the corresponding flow distributions presented and discussed in Section 4.4.

Consider now the second group of figures, 5.11 to 5.15. These all have $x_n/d = 10$, but otherwise correspond with Figs. 5.5 to 5.9 for which $x_n/d = 5$ (no heat transfer data was taken for the B(10,4,1)I geometry). For comparison of Figs. 5.11 to 5.15 with 5.5 to 5.9 on the basis of identical impingement surface lengths, L, the two sets of cases must be considered as having the same x_n since both have $N_c = 10$ rows of holes, and $x_n = L/N_c$. The second set (Fig. 5.11 to 5.15), therefore, had jet hole diameters one-half as large as the first set (Figs. 5.5 to 5.9). For the same mean jet Reynolds number ($\simeq 10^4$) the second set, therefore, has correspondingly higher jet velocities. Thus, the Nusselt numbers shown are generally higher than those for the first set, except in some few cases where the initial crossflow effect penetrates strongly into the array. The η profiles, however, are quite similar to the first set, being most sensitive to the jet flow distribution rather than the level of jet velocities. It may be recalled that the flow distributions for these geometries with a fixed number of jet rows were shown to be independent of x_n/d, depending only on the parameter $(y_n/d)(z/d)$ and (m_c/m_j), whenever wall shear effects were negligible. A small dependence on x_n/d arises when wall shear becomes significant. The overall trends with geometric variation for the second group of figures are similar to the first group.

Unlike the η profiles, the Nu profiles do not all vary monotonically with streamwise location. Rather considering the entire set of results, Figs. 5.5 through 5.16, Nu variations include monotone decreasing, monotone increasing, and cases with one or two local minima and/or maxima. An important observation to emphasize is that in most cases the addition of the initial crossflow (which means an increase in the total coolant flow, since m_j was kept essentially constant for each geometry), resulted in reduced mean values of Nusselt number over the jet array region. Of all the arrays tested only those with $z/d = 1$ showed higher mean values of Nu at one or more of the finite initial

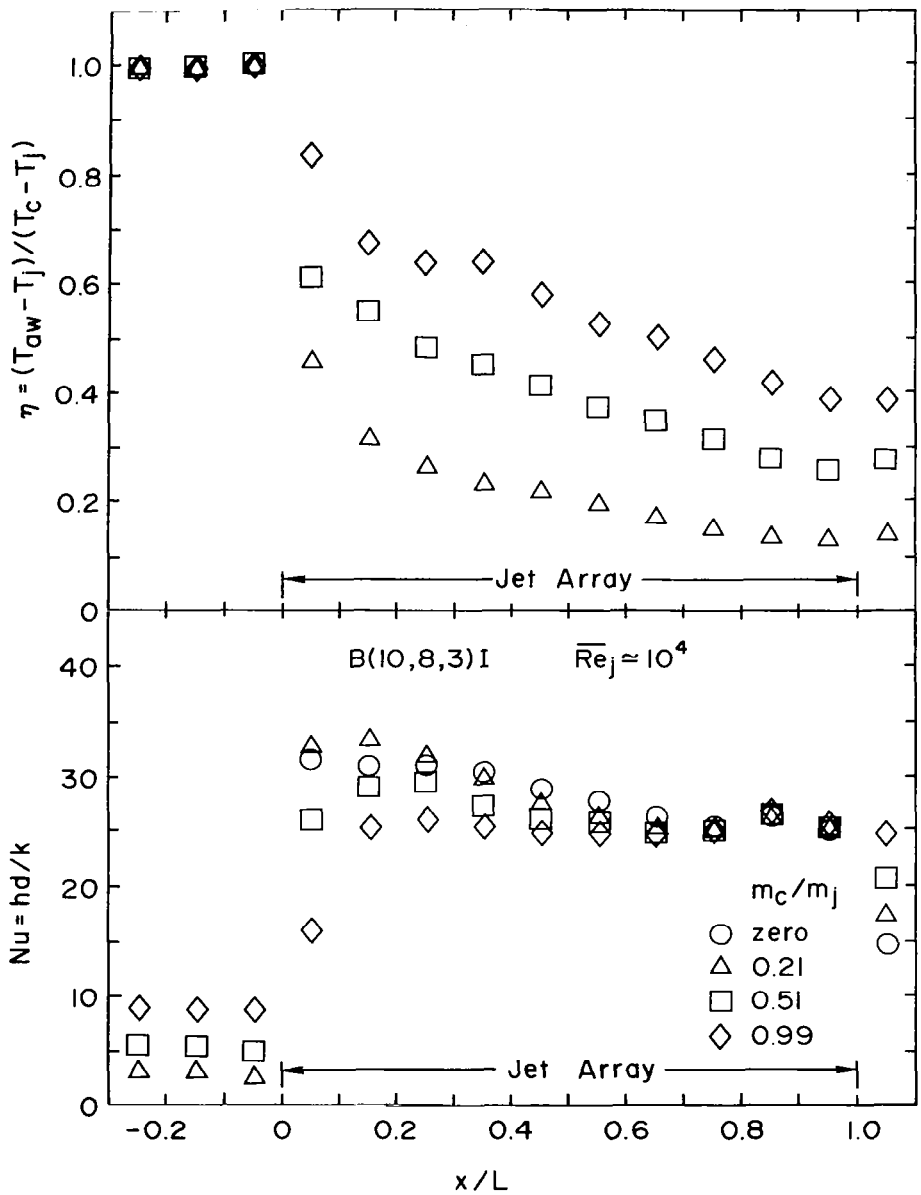

Fig. 5.11 Effect of initial crossflow rate on η and Nu profiles for B(10,8,3)I geometry.

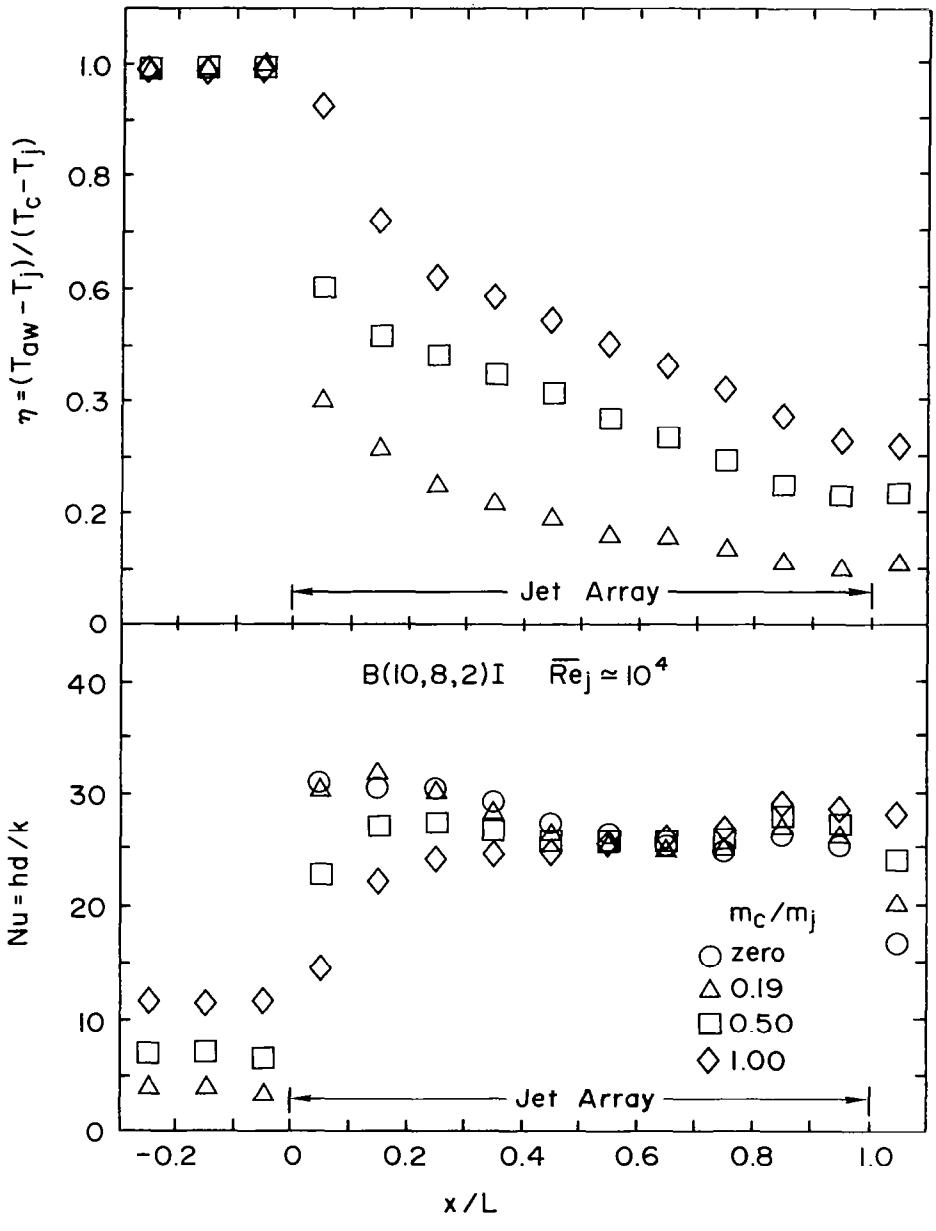

Fig. 5.12 Effect of initial crossflow rate on η and Nu profiles for B(10,8,2)I geometry.

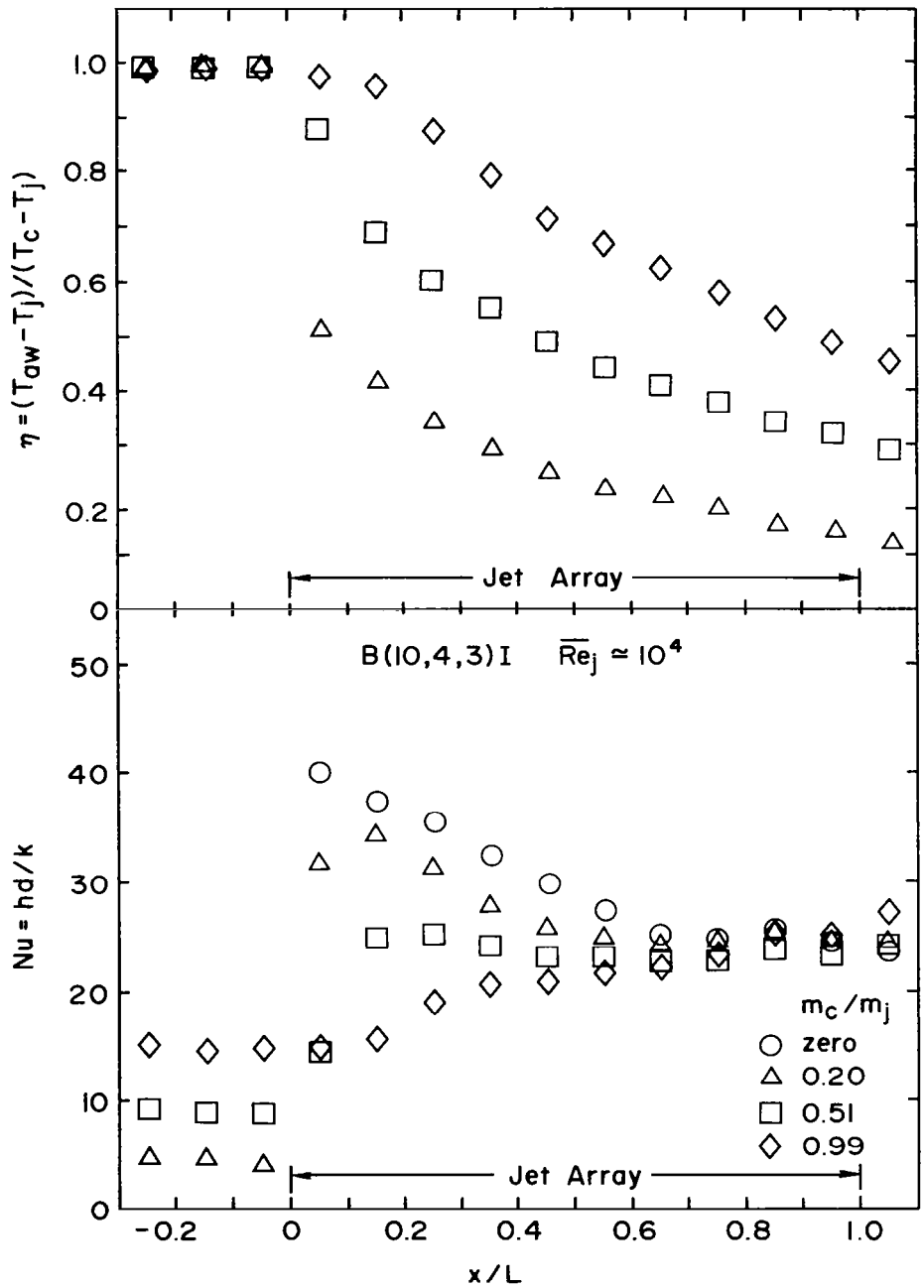

Fig. 5.13 Effect of initial crossflow rate on η and Nu profiles for B(10,4,3)I geometry.

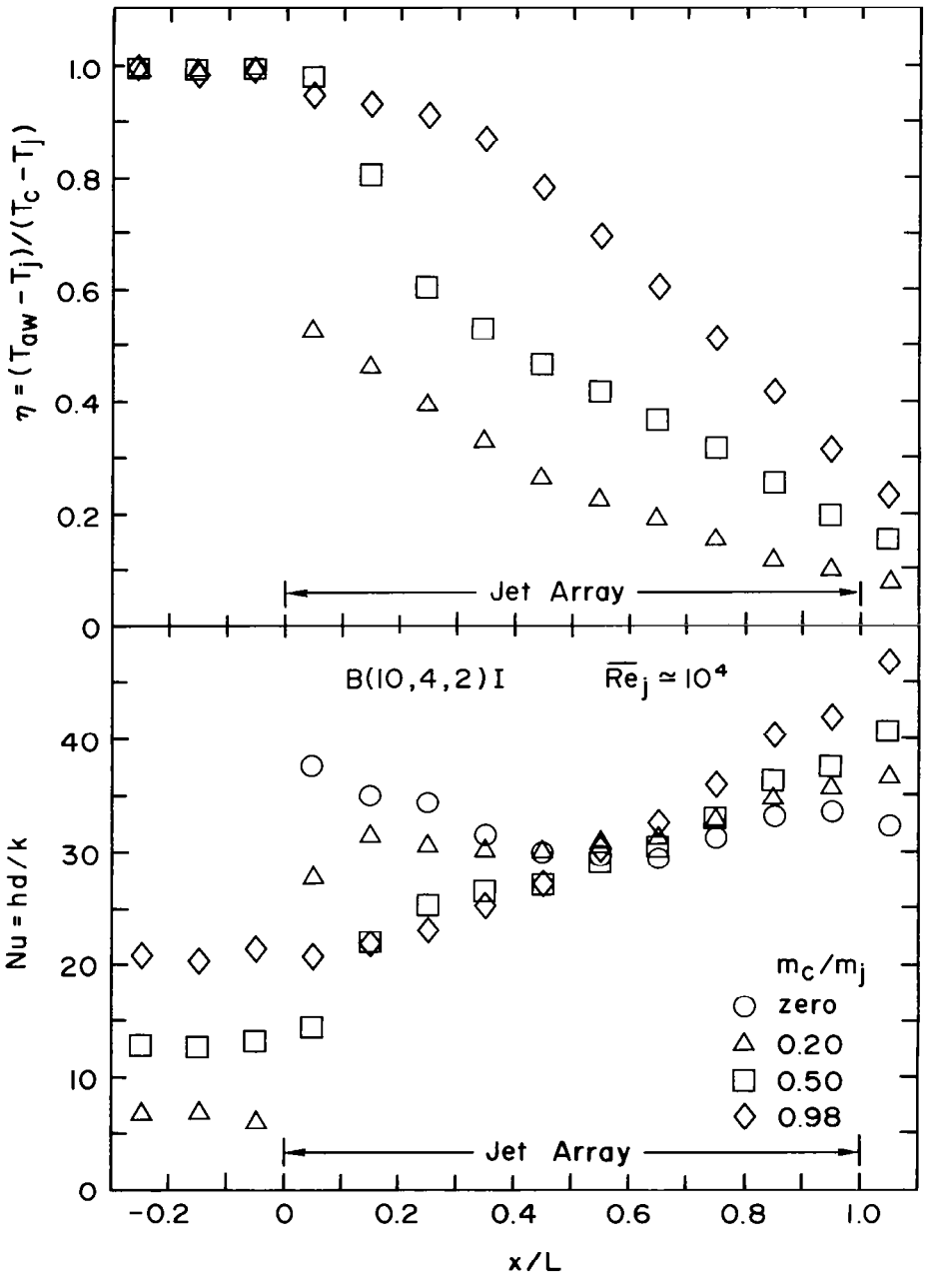

Fig. 5.14 Effect of initial crossflow rate on η and Nu profiles for B(10,4,2)I geometry.

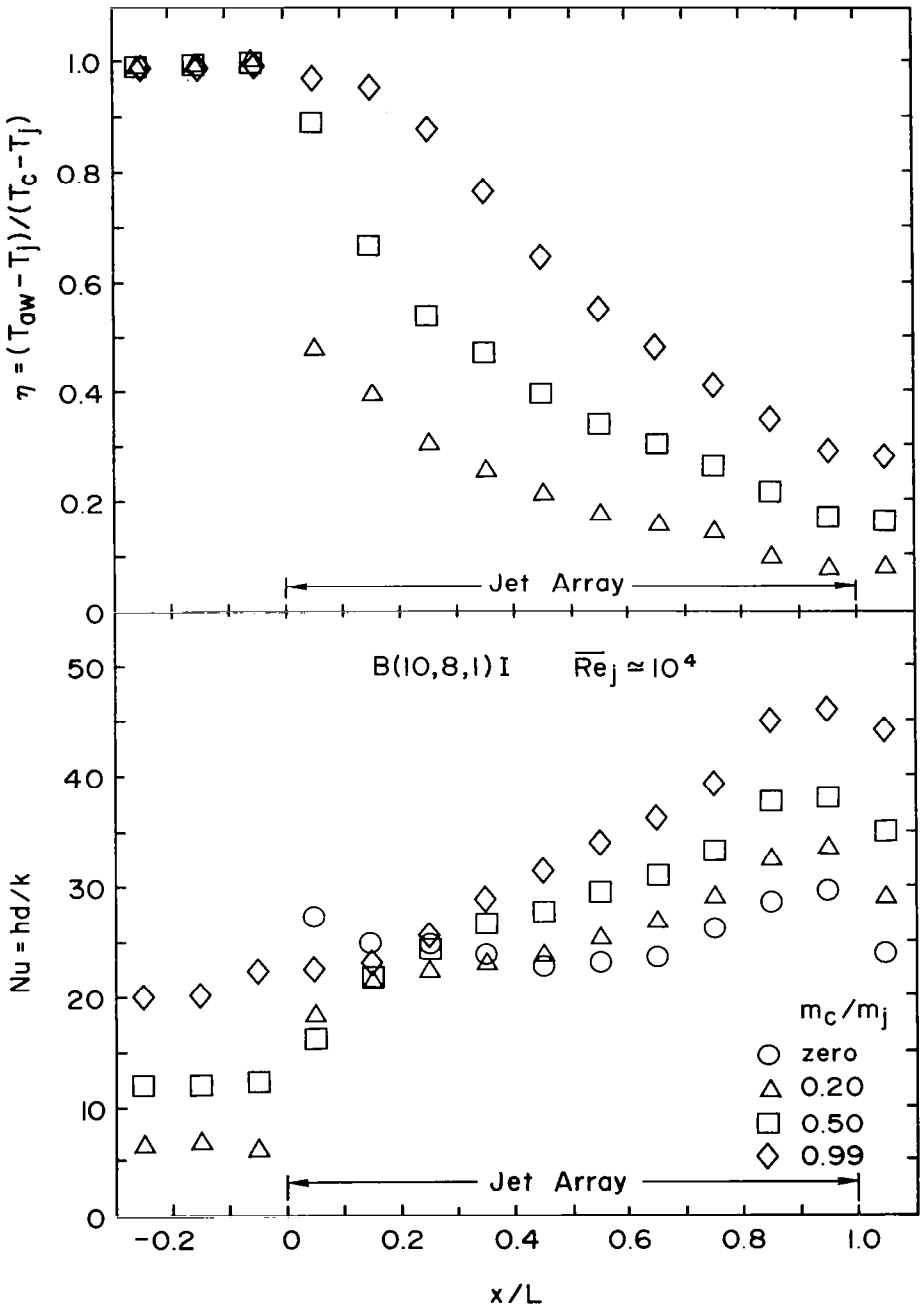

Fig. 5.15 Effect of initial crossflow rate on η and Nu profiles for B(10,8,1)I geometry.

crossflow values, as compared with the zero initial crossflow case. Even these cases resulted in a degradation in mean Nusselt number due to the presence of an initial crossflow, when considered per unit of total coolant flow rate ($m_c + m_j$). The variation of $\overline{Nu}$ with m_c/m_j may be examined in detail in Appendix D, Table D.2, which includes values of $\overline{Nu}$ (mean over the array) as well as the streamwise profiles.

Finally, consider the results for the staggered array, B(5,4,3)S, Fig. 5.16 as compared with its inline counterpart, Fig. 5.7. This geometry was selected for testing with a staggered hole pattern since in prior noninitial crossflow tests it showed the largest effect of hole pattern on the spanwise averaged heat transfer coefficients [1,8]. It has the closest hole spacings and largest z/d of all the arrays tested. Streamwise flows distributions for this staggered pattern were found to be essentially the same as those for the inline case. The η profiles for the staggered array fall above those for the inline array, insignificantly for the smallest initial crossflow ratio, $m_c/m_j = 0.2$, but noticeably for $m_c/m_j = 0.5$ and 1.0, especially downstream.

For all flow ratios from zero to unity, the staggered array Nusselt numbers are the same as the inline values at the first upstream row with inline values becoming larger than the staggered values as one proceeds downstream. An explanation for this type of behavior was originally presented in some detail in connection with noninitial crossflow test results [1,9]. Basically it may be speculated that there is less mixing of the jet and crossflow at downstream rows for the inline pattern than for the staggered pattern. Hence, the inline impinging jets more nearly retain their identity and provide more effective cooling than those in the staggered pattern. Though the phenomena involved is extremely complex, so that conclusive explanations are premature, the η behavior also fits the above intepretation in that the jets are less dominant in the staggered case since they mix somewhat more with the crossflow.

Prior heat transfer measurements for one geometric configuration for a two-dimensional array of circular impinging jets with an initial crossflow were made by Saad, et al. [10]. Only Nusselt number results were presented. No indication of adiabatic wall temperatures or the relation of the initial crossflow temperatures to the jet temperatures was given. The Nusselt numbers

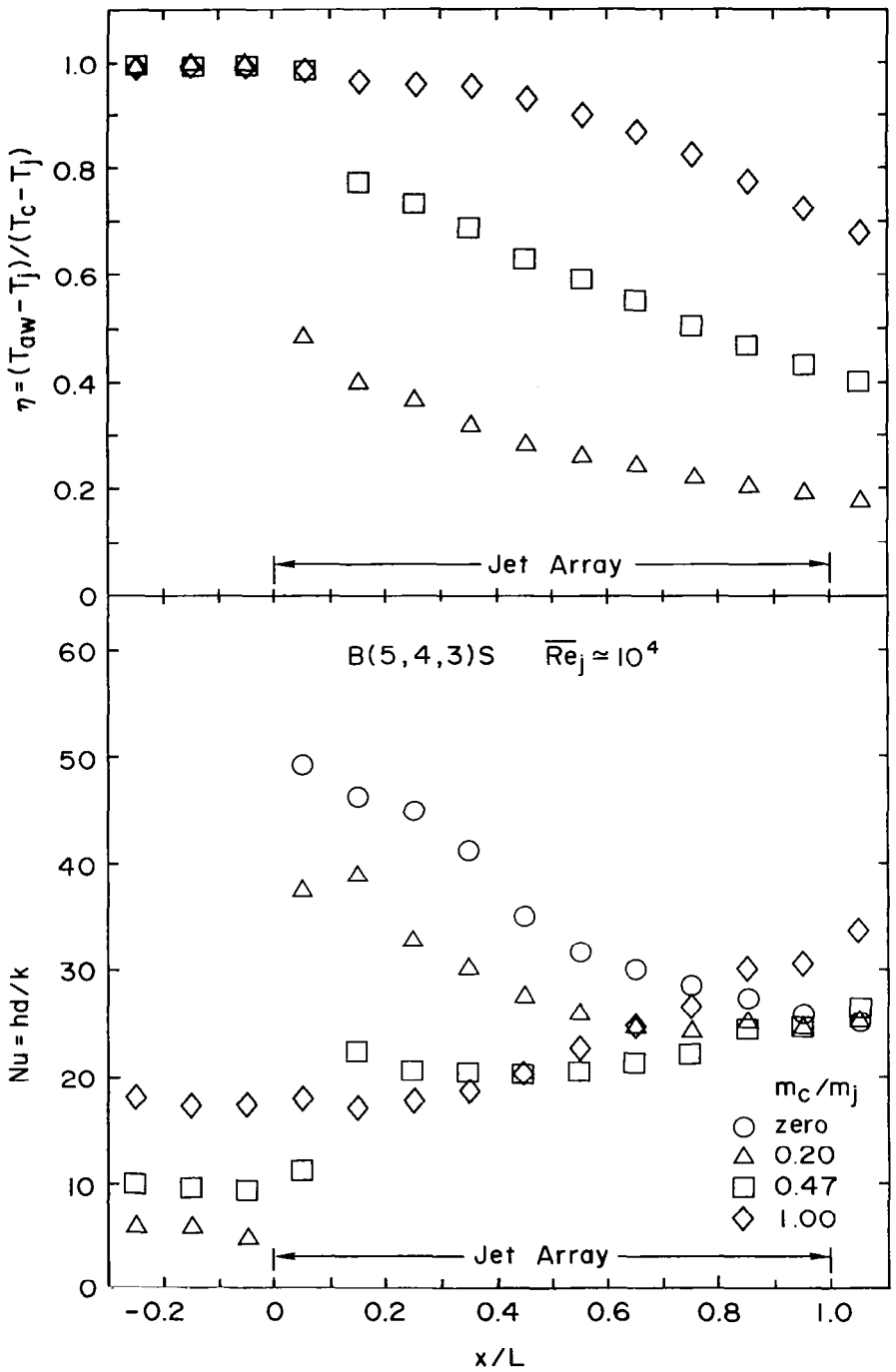

Fig. 5.16 Effect of initial crossflow rate on η and Nu profiles for B(5,4,3)S geometry.

could not be directly compared with results of the present measurements, because the hole spacings of the array studied in [10] were below the range covered in the present study. However, on a relative basis, the Nusselt number magnitudes were consistent with the present results.

6. CONCLUDING REMARKS (PART I)

6.1 Flow Distributions

Experimentally determined flow distributions for jet arrays with ten spanwise rows of holes in the presence of an initial crossflow have been presented. These flow distributions range from uniform to highly nonuniform depending on the geometric parameters and the ratio of initial crossflow to jet flow. For crossflow-to-jet velocity ratios greater than a value somewhat less than unity, jet orifice discharge coefficients do not remain constant but decrease significantly, and show a secondary dependence on z/d. However, for the full range of geometric parameters covered the crossflow-to-jet velocity ratios never become large enough for this discharge coefficient effect to be very significant when there is no initial crossflow present. In addition the effect is not significant in the presence of initial crossflow rates at least as high as the total jet flow rate, as long as the geometric parameter $(y_n/d)(z/d)$ is equal to or greater than 12. As this parameter decreases, cross-to-jet velocity ratios become large enough to affect the discharge coefficients but only for initial crossflow to total jet flow ratios above a certain value. This value decreases as the parameter $(y_n/d)(z/d)$ decreases.

Predictions based on a relatively simple one-dimensional model in which effects of channel wall shear were first excluded, then included show that this effect becomes significant for essentially the same conditions that the variable discharge coefficient effect does. The model, with constant C_D and $f = 0$, results in closed form solutions which are in excellent agreement with the data. Otherwise, numerical solutions are required. These, too, are quite consistent with the data but the agreement in all cases is not as good. The primary reason may be the higher sensitivity, in these cases, of the predictive model to uncertainties in the input parameters and the lack of an adequately precise friction factor model for these complex flows. However, the cases where variable discharge coefficient and wall shear effects tend to be of more than minor significance are primarily those with narrow channel heights of $z/d = 1$. These cases may also have somewhat lesser significance in terms of practical application.

6.2 Heat Transfer Characteristics

Experimentally determined spanwise averaged, streamwise resolved dimensionless adiabatic wall temperatures (η values) and Nusselt numbers for jet arrays with ten spanwise rows of holes in the presence of an initial crossflow have been presented. The η values within the array, under some conditions, span the range from unity to nearly zero. Nusselt numbers at the upstream rows of the array are in many cases significantly reduced even by small initial crossflow rates relative to the total jet flow rate. The practical implication of these results is of considerable importance. For example, in a highly cooled first stage vane like that shown in Fig. 1.2, T_c is often several hundred degrees above T_j. Typical values are T_s = 1260 K, T_j = 760 K, and T_c = 870 K. The results for η and Nu from Section 5, if converted to heat fluxes, imply that local cooling rate predictions within the array could, in many cases, easily be in error by 100% or more depending on the designer's guess, in the event he did not have available to him detailed quantitative results for the effect of the initial crossflow rate and temperature. There is evidence that this level of design uncertainty exists in practice, and that premature failures of impingement cooled airfoils have been the result. With better information available on the effects of initial crossflow, it should be possible to make significant improvements in design and to further develop the full potential of impingement cooled gas turbine vanes and blades.

It should be emphasized that the η values presented, though resolved in the streamwise direction, are defined in terms of the initial crossflow temperature at the entrance to the array. In applications of these coefficients, the designer should also use this characteristic temperature. As a good approximation the stagnation temperature (mixed-mean value) at the entrance to the array may be used. Or, for better accuracy, the corresponding adiabatic wall temperature may be used, computed on the basis of a recovery factor. Unless more specific information is available for the particular conditions being considered, a recovery factor of 0.9 is recommended [22].

Most of the measurements were carried out for nominal mean jet Reynolds numbers values of 10^4. The Nusselt number data tabulated in Appendix D, Table D.2 may be applied at other $\overline{Re}_j$ (or Re_j) by assuming the Nusselt numbers to be

proportional to $Re_j^{0.72}$ [2,11] (see also Fig. 5.3), unless upstream rows are being considered in a case where the initial crossflow dominates ($\eta \sim 1$). Then, the use of the exponent 0.80 on the Reynolds number is recommended since a duct or channel-like flow is not only penetrating within the array but dominating the flow field.

As an extension of the present study it is recommended that streamwise resolved η values, based on characteristic crossflow temperatures evaluated immediately upstream of individual spanwise rows within the array, rather than at the entrance to the array, be determined. This would permit an attempt to correlate the η values, so defined, in terms of the local cross-to-jet velocity ratios and geometric parameters. Such an attempt, if successful, would provide the designer with greater flexibility in the application of the results. In such an effort, however, more attention should also be given to the effect on η of the thermal boundary condition at the jet exit plane of the crossflow channel within the array region.

PART II - EFFECTS OF NONUNIFORM ARRAY GEOMETRY

7. INTRODUCTORY REMARKS (PART II)

Effects of nonuniform jet array geometries on both flow distributions and heat transfer characteristics were investigated for arrays of circular jets in noninitial crossflow configurations. The objective was to determine the degree of confidence the designer can place in streamwise resolved heat transfer coefficients for nonuniform arrays which are based on experimental results from uniform arrays. Results are reported for a number of configurations in which either the spanwise hole spacing or the jet hole diameter is nonuniform. Results for one case in which the streamwise hole spacing was nonuniform are also reported. The experimental facility as used for the nonuniform array tests is described in Section 8, along with a complete summary of the nonuniform jet array geometries tested.

Flow distributions for the nonuniform arrays are dealt with in Section 9. Experimentally determined flow distributions obtained for selected arrays are used to validate a theoretically based flow distribution model, extended in Section 9 to cover the case of nonuniform arrays.

Heat transfer characteristics are presented and discussed in Section 10. Experimental results for spanwise averaged Nusselt numbers, resolved in the streamwise direction to one streamwise hole spacing, are presented for each nonuniform array tested. The validated flow distribution model is then utilized to compare these results with the previously reported uniform array data [1,8] and with the previously developed correlation based on these data [2,11].

Part II closes with concluding remarks presented in Section 11.

8. NONUNIFORM ARRAY EXPERIMENTAL FACILITY

The basic test model geometry for the nonuniform arrays is identical to that previously utilized for a comprehensive series of uniform array tests [1,8,9], except that the arrays are now composed of two adjacent uniform array geometries, each of which have different values of one of the three geometric parameters, x_n, y_n, or d. This is illustrated in Fig. 8.1 for the case where y_n is the parameter whose value changes. The upstream region is denoted as region 1, the downstream region as region 2, with corresponding subscripts used to distinguish quantities having different values in the two regions. For quantities having identical values no subscript is used. These geometric configurations are incorporated into the test unit assembly shown in Fig. 8.2, previously utilized in this same configuration for uniform array tests without initial crossflow. The interchangeability of the jet plates permitted the testing of nonuniform arrays. A description of the interchangeable jet plenum shown in Fig. 8.2, termed a B-size, was given in some detail in Section 3 of Part I. Additional details regarding the basic test facility were also given there and in [1]. When the B-size plenum is in use only the portion of the heat transfer test plate opposite the jet plate is active. The B-size was used for all but one of the nonuniform array tests to be reported here. A larger jet plate (in the streamwise direction) with a larger jet plenum, termed a D-size, was used for testing one of the arrays with a nonuniform jet hole diameter. The D-size plenum/jet plate assembly covers the entire test plate unit, and with it in place the entire heat transfer test plate is active.

The nonuniform array geometries for which tests were conducted are summarized in Table 8.1. Heat transfer tests were conducted for all of the cases listed, with flow distribution tests conducted for those cases so indicated. Most of the tests were for arrays with nonuniform spanwise hole spacings and nonuniform hole diameters. All of these tests had a total of ten spanwise rows of holes over the entire array (two regions) just as did the previously reported results for uniform arrays [1,8,9]. One test is included for an array with a nonuniform streamwise hole spacing. This array had a total of 6 spanwise rows.

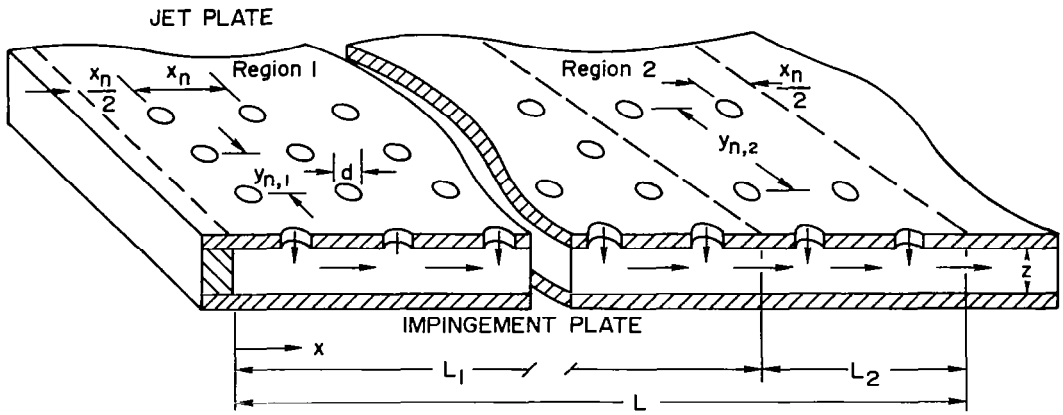

Fig. 8.1 Example of basic test model geometry and nomenclature for nonuniform array.

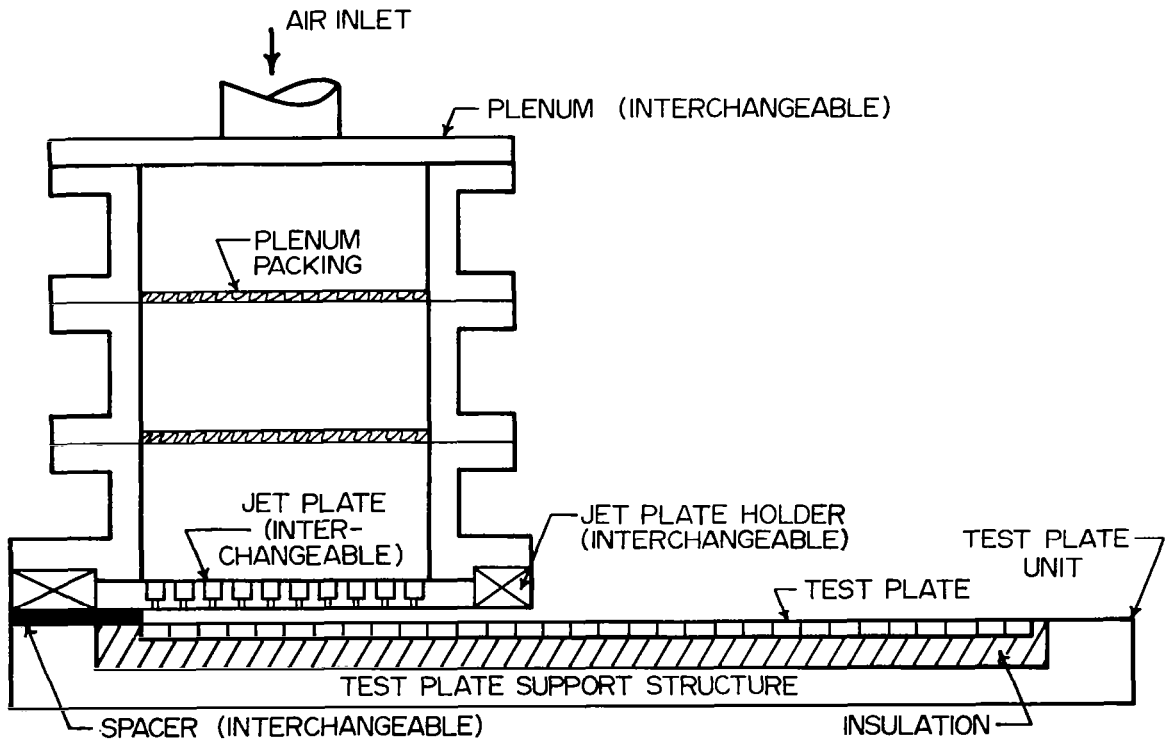

CHORDWISE VIEW

Fig. 8.2 Test unit assembly in noninitial crossflow configuration for nonuniform array tests.

Table 8.1 Nonuniform Array Geometries Tested

Nonuniform Parameter	Array Geometry† Region 1	Region 2	Number of Rows Region 1	Region 2	d (cm)	Test Series #
x_n	B(10,8,3)I	B(5,8,3)I	4	2	0.254	1X*
y_n	B(5,8,3)I	B(5,4,3)I	8	2	0.254	2Y*
	B(5,4,3)I	B(5,8,3)I	4	6	0.254	3Y*
	B(5,8,3)I	B(5,4,3)I	2	8	0.254	4Y*
	B(5,4,3)I	B(5,8,3)I	1	9	0.254	5Y*
	B(10,8,3)I	B(10,4,3)I	8	2	0.127	6Y
	B(5,8,2)I	B(5,4,2)I	8	2	0.254	7Y
	B(10,8,2)I	B(10,4,2)I	8	2	0.127	8Y
	B(10,8,2)I	B(10,4,2)I	5	5	0.127	9Y
					d_1(cm)	
d	B(10,8,2)I	B(5,4,1)I	5	5	0.127	1D*
	B(5,4,1)I	B(10,8,2)I	5	5	0.254	2D*
	D(15,6,3)I	D(10,4,2)I	5	5	0.254	3D
	D(10,4,2)I	D(15,6,3)I	5	5	0.381	4D

† $(x_n/d, y_n/d, z/d)$
Prefix designates overall array length: B(L = 12.7 cm), D(L = 38.1 cm)
Suffix designates hole pattern: I = Inline

* Flow distribution (row-by-row) measured in addition to heat transfer coefficients

Note: b = d, for Test Series 1X and for 2Y through 9Y
b = largest of d_1 or d_2, for Test Series 1D through 4D

Arrays with a nonuniform hole spacing, x_n or y_n, were prepared from previously machined uniform array jet plates by either plugging or taping over selected jet holes. When plugging was used cork composition plugs were inserted in the counterbores of the appropriate jet holes forming a satisfactory seal. For arrays with a nonuniform hole diameter new jet plates were machined. Each had five spanwise rows of holes of a smaller diameter in one region, and five rows of a larger diameter in the other region. They were designed so they could be reversed end-to-end in the streamwise direction in the jet plenum assembly. Thus, each could be used to give a small-to-large hole diameter transition in the streamwise direction, as well as a large-to-small diameter transition.

9. NONUNIFORM GEOMETRY FLOW DISTRIBUTIONS

9.1 Experimental Procedures and Data Reduction

The details of the experimental procedures and data reduction techniques for the nonuniform geometry flow distribution tests were identical to those described in Section 4.1 of this report for the initial crossflow tests, and will not be repeated here. It should be noted, however, that jet hole discharge coefficients for each sub-array (region) within a nonuniform array were assumed constant. This was justified since the resulting crossflow-to-jet velocity ratios were never large enough to significantly affect the discharge coefficients, just as in the case of the prior uniform array geometries in the absence of initial crossflow (Section 4.4). In addition, mass balances performed as described in Section 4.1 closed to within better than 3%.

For nonuniform arrays in which one of the two regions was formed by plugging certain holes in a uniform array jet plate, the discharge coefficients for both regions were set equal to the previously measured $\bar{C}_D$ for the original jet plate. For arrays with nonuniform hole diameters, which were newly machined jet plates, C_D for each region was set equal to the originally measured $\bar{C}_D$ for the uniform jet plate of corresponding geometry. For these cases the $\bar{C}_D$ values used for the two regions may differ somewhat.

9.1 Theoretical Model

A theoretical model for the row-by-row flow distributions for the nonuniform geometries may be developed on the same basis as that originally presented by Florschuetz, et al. [2,11] for uniform geometries, and also utilized for cases with initial crossflow as presented in Section 4, Part I of this report. That is, the uniform discrete hole array is assumed to be replaced (temporarily) by a surface over which the injection is continuously distributed. A nonuniform array in which any one or more of the geometric parameters x_n, y_n, or d undergo one or more changes in value in the streamwise direction along the array (e.g., Fig. 8.1), may be regarded as composed of a series of coupled uniform geometry sub-arrays (regions).

Consider a nonuniform array composed of n regions. A second order

ordinary differential equation of the same form as Eq. (4.6) for the crossflow mass velocity as a function of streamwise location will apply for each region. The boundary conditions at the entrance and exit of the nonuniform array are, in general, the same as expressed in Eqs. (4.7). Two matching conditions must be satisfied at each of the (n − 1) interfaces between the n regions. Both the crossflow rate (therefore, the crossflow mass velocity) and the channel pressure must be continuous across each interface. Thus, there are n second order differential equations with two boundary conditions and 2(n − 1) matching conditions, for a total of 2n side conditions for the general case.

The nonuniform jet plates tested in the present study each had two regions. They were tested in the absence of an initial crossflow, i.e., in a noninitial crossflow configuration (Figs. 8.1 and 8.2). It was shown in Section 4, Part I that for the uniform arrays in the absence of an initial crossflow, both wall shear and variable discharge coefficient effects on the flow distributions were negligible. It may be anticipated that these effects would ordinarily also be negligible for nonuniform arrays whose regions have combinations of geometric parameters corresponding to those of the prior uniform arrays. The governing equations, boundary and matching conditions for a two-region array with no initial crossflow, negligible wall shear, and a constant discharge coefficient in each region (the value of C_D may, in general, be different in each region) are summarized below in dimensionless form:

$$\left.\begin{aligned} \frac{d^2\tilde{G}_{c,1}}{d\tilde{x}^2} - B_1^2\tilde{G}_{c,1} &= 0 \quad \text{for} \quad 0 \le \tilde{x} \le \tilde{L}_1 \\ \frac{d^2\tilde{G}_{c,2}}{d\tilde{x}^2} - B_2^2\tilde{G}_{c,2} &= 0 \quad \text{for} \quad \tilde{L}_1 \le \tilde{x} \le 1 \end{aligned}\right\} \tag{9.1}$$

$$\left.\begin{aligned} \tilde{G}_{c,1} &= 0 \quad \text{at} \quad \tilde{x} = 0 \\ \tilde{G}_{c,2} &= 1 \quad \text{at} \quad \tilde{x} = 1 \end{aligned}\right\} \tag{9.2}$$

$$\left.\begin{aligned} \tilde{G}_{c,1} &= \tilde{G}_{c,2} \\ (d\tilde{G}_{c,1}/d\tilde{x})/(d\tilde{G}_{c,2}/d\tilde{x}) &= B_1/B_2 \end{aligned}\right\} \quad \text{at } \tilde{x} = \tilde{L}_1 \tag{9.3}$$

where $B_k = \sqrt{2}\ (A_o^* C_D)_k L/z$ and $\tilde{L}_k = L_k/L$.

The second of the two matching conditions of Eqs. (9.3) is based on the requirement of a continuous channel pressure noted earlier. It is derived by applying Eq. (4.3) to each region, equating the channel pressures, and eliminating G_j^* in favor of G_c with the aid of (4.5).

The solution of the coupled Eqs. (9.1) with boundary conditions (9.2) and matching conditions (9.3) may be written in terms of hyperbolic trigonometric functions:

$$\tilde{G}_{c,k} = \frac{1}{\sinh B_k \tilde{L}_k} (E_k \sinh B_k \tilde{x} + F_k \cosh B_k \tilde{x}) \qquad (9.4)$$

where for the first region (k=1),

$$E_1 = \frac{1}{(\coth B_1 L_1 + \coth B_2 L_2) \sinh B_2 L_2}$$

$$F_1 = 0$$

and for the second region (k=2),

$$E_2 = \cosh B_2 L_1 - E_1 \cosh B_2$$

$$F_2 = E_1 \sinh B_2 - \sinh N_2 L_1$$

The corresponding continuous injection velocity, $G_{j,k}^*$ may then be written utilizing (9.4) in (4.6), where (4.6) is applied to each region. This result is then utilized to evaluate the discrete hole array jet velocity distribution by assuming that the value of $G_{j,k}$ for a given spanwise row is that corresponding to $G_{j,k}^*(x)$, where x is evaluated at the centerline of the row. Noting that $G_{j,k}^* = A_{o,k}^* G_{j,k}$, the final result for the jet velocity distribution for a nonuniform array composed of two uniform sub-arrays is

$$\frac{G_{j,k}}{\bar{G}_j} = \frac{A_o^*}{A_{o,k}^*} \frac{B_k}{\sinh B_k \tilde{L}_k} (E_k \cosh B_k \tilde{x} + F_k \sinh B_k \tilde{x}) \qquad k=1,2 \qquad (9.5)$$

The crossflow parameter of interest is the crossflow velocity approaching a given spanwise jet row relative to the jet velocity of the row. As in

Section 4, Part I, this may be satisfactorily approximated utilizing $G_{c,k}$ from the continuous injection model, Eq. (9.4), evaluated one-half a hole spacing upstream of the given row (Fig. 4.5b), divided by $G_{j,k}$ from (9.5). This operation results in

$$\left(\frac{G_c}{G_j}\right)_k = \frac{1}{\sqrt{2}\ C_{D,k}} \frac{E_k \sinh B_k\tilde{x}' + F_k \cosh B_k\tilde{x}'}{E_k \cosh B_k\tilde{x} + F_k \sinh B_k\tilde{x}} \qquad k=1,2 \qquad (9.6)$$

where $\tilde{x}' = \tilde{x} - (1/2)(x_{n,k}/L)$.

9.3 Results and Discussion

Flow distribution data for a series of two-region nonuniform geometry arrays are presented in Figs. 9.1 through 9.7. Each figure represents a single geometric configuration tested at a single total jet flow rate. Each figure displays data points for the normalized jet mass velocity, $G_j/\bar{G}_j$, and for the crossflow-to-jet mass velocity ratio, G_c/G_j, as a function of streamwise location, x/L. These data, as well as the original pressure traverse data from which they were determined, are also summarized in tabular form in Appendix E, Table E.1. The position of the interface between the two regions of each array is indicated by the vertical dashed line. Mean jet Reynolds numbers, values of discharge coefficients, and closures resulting from the mass balances are also indicated in each figure. The closures are the ratio of the sum of the individual spanwise row flow rates to the total jet flow rate as measured at the metering section upstream of the jet plenum. The solid curves, representing the predictions of the theoretical model, were calculated from Eqs. (9.5) and (9.6). In every case the agreement between the data and the theoretical predictions is excellent.

Consider first Figs. 9.1 through 9.4, each for a case in which the spanwise hole spacing y_n/d was either doubled or cut in half at some position along the array. Since these cases all had a z/d of three, the resulting flow distributions were rather uniform, and the effect of the step change in y_n/d is not readily apparent in the $G_j/\bar{G}_j$ plots. It is, however, apparent in the plots for G_c/G_j.

The results presented in Figs. 9.5 and 9.6 are for arrays in which the

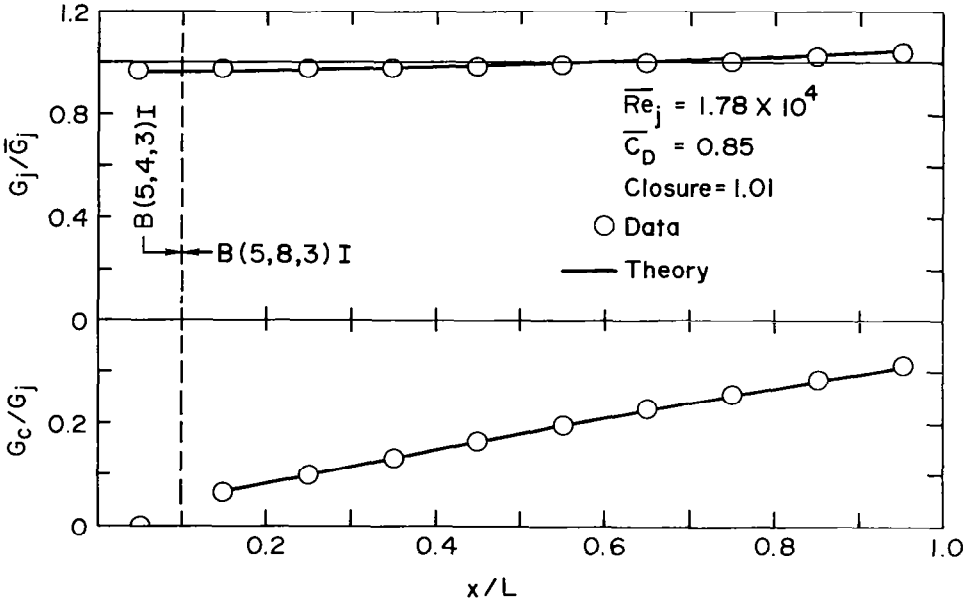

Fig. 9.1 Flow distribution data for nonuniform y_n array compared with theory. Test #5Y.

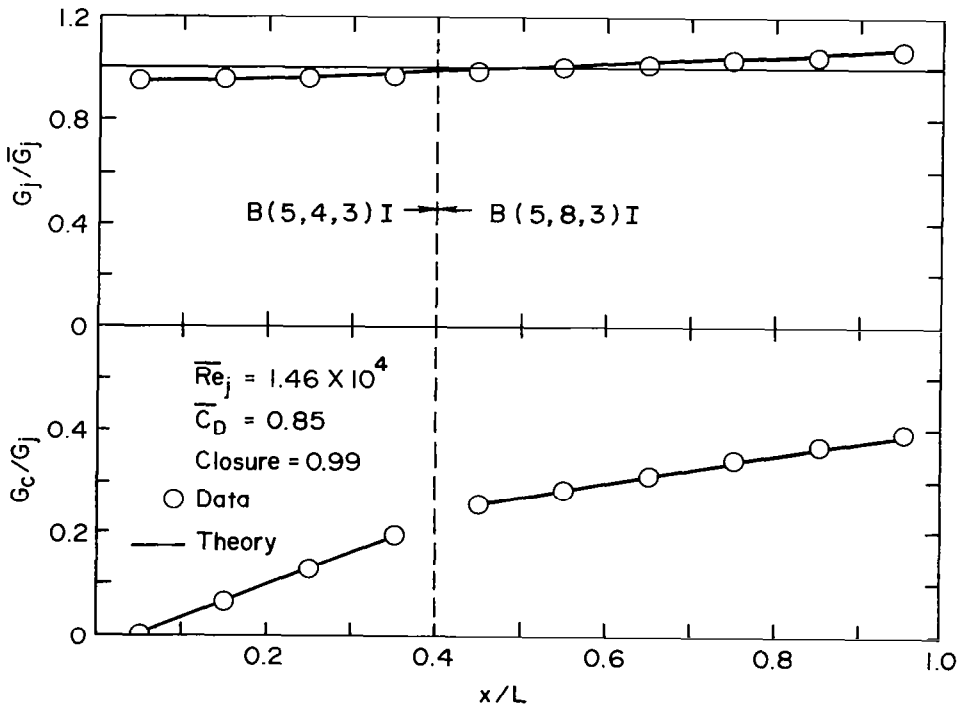

Fig. 9.2 Flow distribution data for nonuniform y_n array compared with theory. Test #3Y.

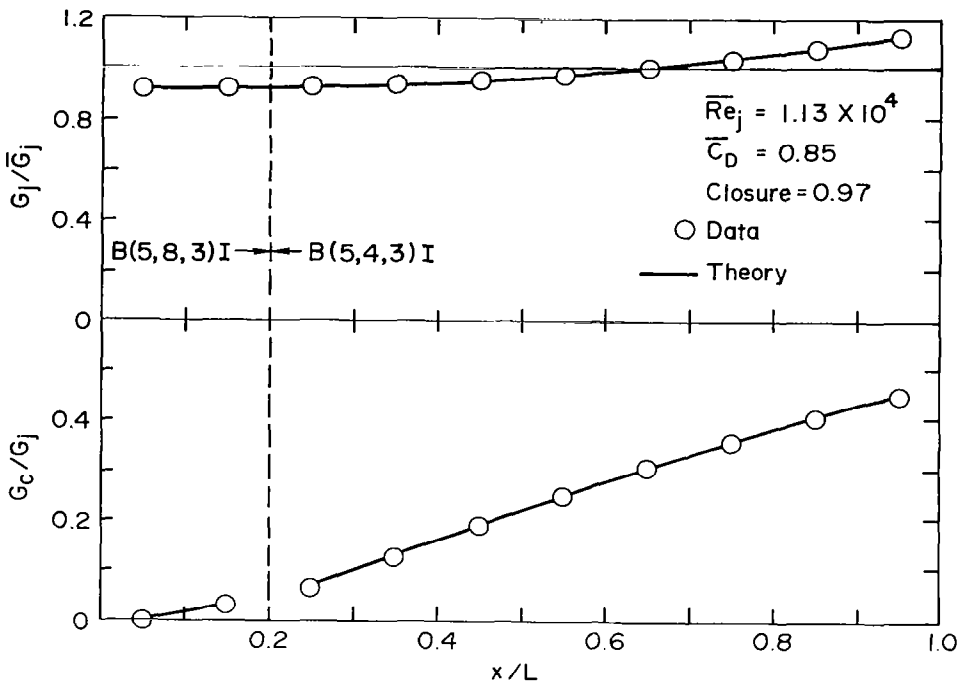

Fig. 9.3 Flow distribution data for nonuniform y_n array compared with theory. Test #4Y.

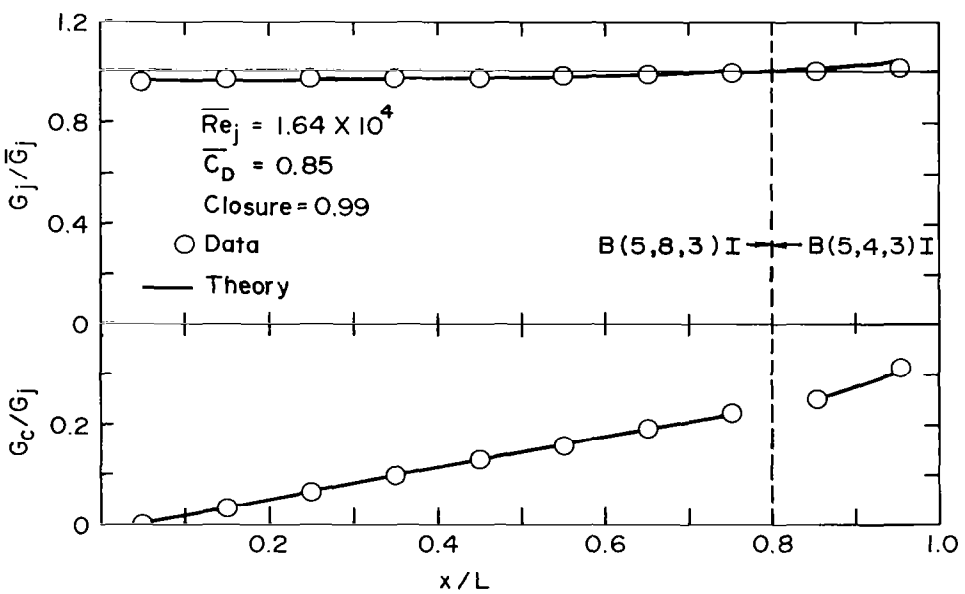

Fig. 9.4 Flow distribution data for nonuniform y_n array compared with theory. Test #2Y.

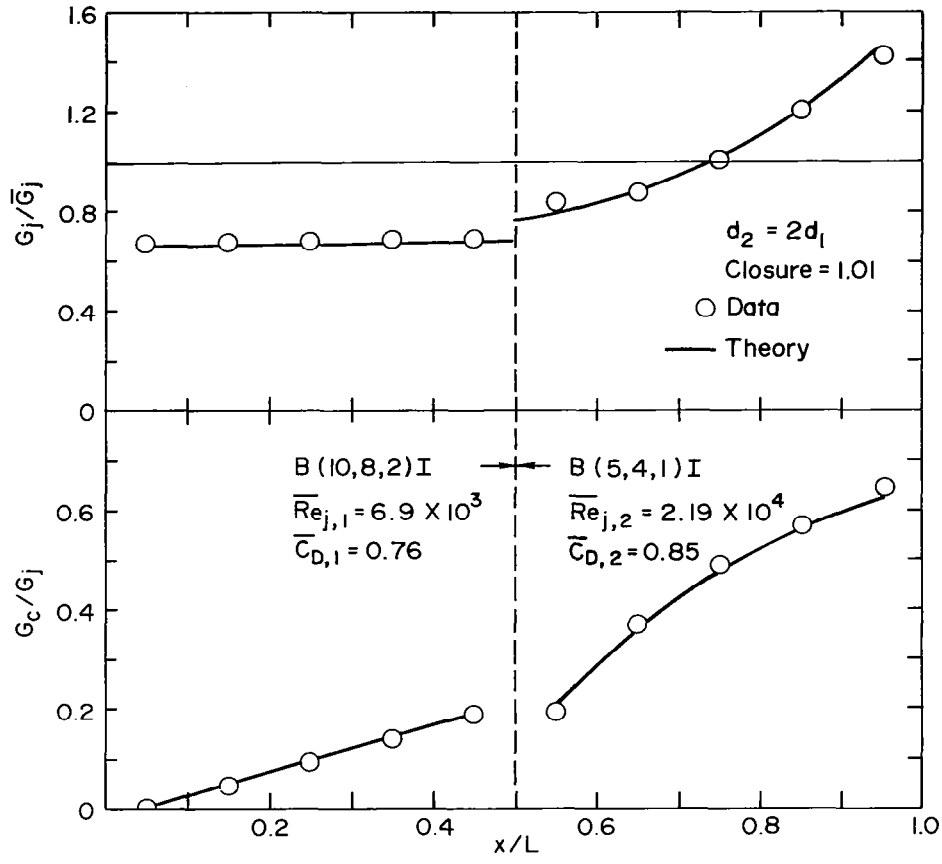

Fig. 9.5 Flow distribution data for nonuniform diameter array compared with theory. Test #1D.

jet hole diameter over the downstream half of the array is either double (Fig. 9.5) or one-half (Fig. 9.6) that over the upstream half. Since each of these cases involves a substantial region over which $y_n/d = 4$ and $z/d = 1$, the flow distributions are quite nonuniform; and the effect of the step change in hole diameter is quite apparent. These cases provide a more severe test of the model than those of Figs. 9.1 through 9.4, but the agreement is still excellent. It may be of interest to note that the first (i.e., upstream) region of a nonuniform array (without initial crossflow) may be thought of as a uniform array <u>without</u> initial crossflow, while a downstream region (e.g., the second region of a two-region array) may be thought of as a uniform array <u>with</u> ''initial'' crossflow (the ''initial'' crossflow arising from the upstream regions). Note also that for a uniform array the flow distribution

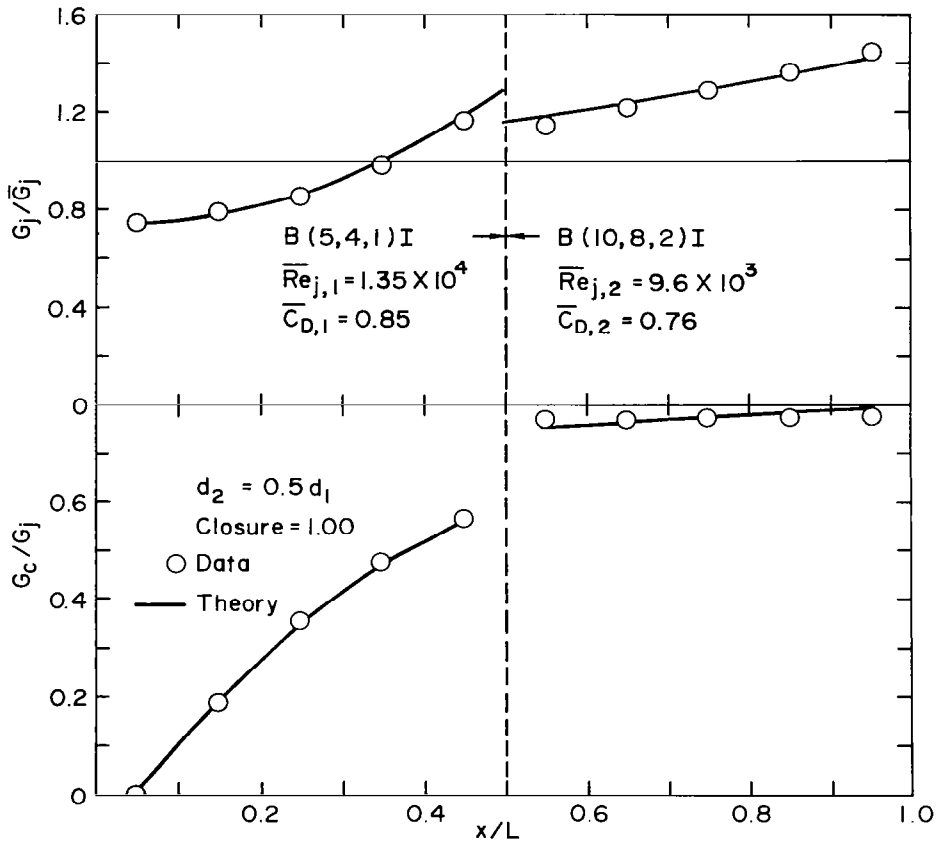

Fig. 9.6 Flow distribution data for nonuniform diameter array compared with theory. Test #2D.

becomes less uniform as $(y_n/d)(z/d)$ decreases and as the initial crossflow increases (Section 4.4).

With these ideas in mind the trends for $G_j/\bar{G}_j$ in Figs. 9.5 and 9.6 may be interpreted. In Fig. 9.5 the upstream region has both a large value of $(y_n/d)(z/d)$ and zero initial crossflow conditions leading to the essentially uniform observed and predicted flow distribution in that region. The downstream region has both a small value of $(y_n/d)(z/d)$ and a finite ''initial'' crossflow leading to the highly nonuniform observed and predicted flow distribution in that region. In Fig. 9.5, we have a case where the $(y_n/d)(z/d)$ and ''initial'' crossflow conditions for each region tend to oppose each other in their effects on the flow distribution. This results in the flow distributions of intermediate nonuniformity observed and predicted for each of the

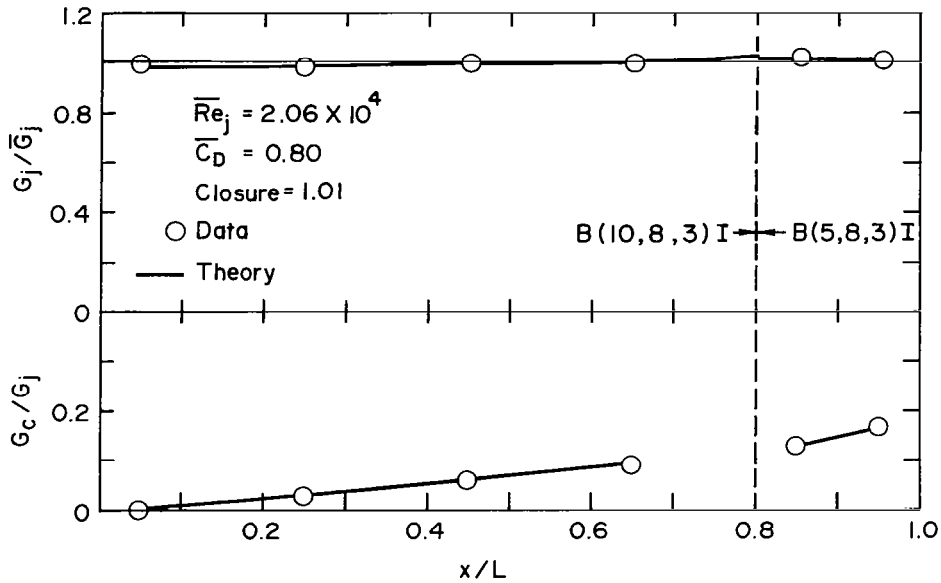

Fig. 9.7 Flow distribution data for nonuniform x_n array compared with theory. Test #1X.

two regions of this array.

One additional flow distribution test result is presented in Fig. 9.7 for a case in which the streamwise hole spacing x_n/d for the downstream region was one-half that for the upstream region.

Heat transfer test results, to be presented in the next section, were obtained for all of the nonuniform geometries for which flow distributions were measured, plus some additional geometries for which flow distributions were not measured. In making certain comparisons of the nonuniform geometry heat transfer coefficients with those from prior uniform geometry arrays and with a previously developed correlation, it was necessary to utilize a flow distribution for each nonuniform array. In those cases where the measured flow distribution was not available, the theoretical model (Section 9.2) was used. The comparisons presented in Figs. 9.1 through 9.7 provide good evidence that reliance on the model is well-justified.

10. NONUNIFORM ARRAY HEAT TRANSFER CHARACTERISTICS

10.1 Experimental Procedures and Data Reduction

Details of the experimental procedures and data reduction techniques were essentially as previously utilized for the noninitial uniform array tests as reported in [1] and for the initial crossflow configuration tests with zero initial crossflow as outlined in Part I, Section 5.2 of this report. For each array tested, three data sets (q, T_s) corresponding to steady-state conditions at three different segment heater power input levels were obtained for each active segment of the test plate. Linear least squares curve fits to an equation in the form $q = h(T_s - T_{aw})$ were then utilized to determine h and T_{aw} at each segment. As in the case of the prior noninitial crossflow tests the experimental uncertainty on the resulting Nusselt numbers is estimated to be about $\pm$ 5%. An attempt was made to select the total jet flow rate (mean jet Reynolds number) at which to test a given nonuniform array, such that the jet Reynolds number at each spanwise row in each of the two uniform regions of the array would fall within the range of jet Reynolds numbers at the row from the prior test of each matching uniform array which had the same ratio of crossflow-to-jet velocity. This, however, was not always possible to achieve.

10.2 Results and Comparisons with Uniform Geometries

In this section the experimentally determined streamwise profiles of heat transfer coefficients for the nonuniform arrays are presented. Results for arrays with nonuniform hole spacings are plotted as Nusselt number profiles ($Nu = hd/k$). Results for arrays with nonuniform hole diameters are plotted as Stanton numbers defined using the mean jet mass velocity over the entire array ($St = h/c_p\bar{G}_j$), so that the plots correctly represent the streamwise variation of the heat transfer coefficient itself. The heat transfer data for the nonuniform arrays is also included in tabular form, Appendix E, Table E.2.

In the following two subsections a series of plots is presented, all having the same basic format and all displaying the same types of comparisons (Figs. 10.1 to 10.12). The form of the plots, the types of comparisons, and the basis of the comparisons will now be explained. Each figure is for a

specific nonuniform array geometry, as indicated on the figure. The location of the interface between the two uniform regions comprising the nonuniform array is marked by the vertical dashed line. The primary result shown on each plot is the set of ten spanwise averaged, streamwise resolved, Nu (or St) values for the nonuniform array geometry indicated on the plot. These points are always represented by the upright solid triangles. Each point represents the average Nu (or St) value over the heat transfer surface increment x_n centered immediately opposite the corresponding spanwise row of jet holes in the array. As previously discussed [2,11], these Nu (or St) values may be considered as a function of the parameter set (Re_j, G_c/G_j, x_n/d, y_n/d, and z/d) where Re_j is the local jet Reynolds number and G_c/G_j is the cross-to-jet velocity ratio, both evaluated at the spanwise row in question.

A second set of points on each plot, always represented by inverted open triangles, is based on the previously reported data for uniform arrays [1,8] having corresponding values of the geometric parameters (x_n/d, y_n/d, z/d). Each point shown is for the same value of Re_j and G_c/G_j as existed for the nonuniform array data point to which it is compared. In order to carry out this comparison it was necessary to use the validated flow distribution models for both uniform arrays ([2,11], also Section 4, Part I of this report), and nonuniform arrays (Section 9). First the values of G_c/G_j and Re_j at the row in question for the nonuniform array were determined. Then, since G_c/G_j is independent of the total jet flow rate, the row from the corresponding uniform array having the same value of G_c/G_j was selected. Next, the value of $\overline{Re}_j$ which, for the selected row in the uniform array, would result in the needed value of Re_j, was calculated. Finally, the individual row interpolation formulas for the uniform array data, in the form $Nu = C\overline{Re}_j^{\,n}$ [1], were utilized to determine the appropriate value of Nu (or corresponding St) for comparison with the nonuniform array data point. These interpolation formulas were good to $\pm$ 3% for 95% confidence [1]. For Region 1 (the upstream region), G_c/G_j values for the geometry of that region match the corresponding uniform geometry values row by row. However, for Region 2 (the downstream region) this does not hold. Therefore, the uniform array row numbers utilized to match the G_c/G_j values are noted for Region 2 over the abscissa of the plot. In cases where it was necessary to interpolate between rows of the uniform array, Nu

values for each of the appropriate adjacent rows were calculated as outlined above, followed by a linear interpolation of Nu as a function of G_c/G_j. Normally the adjacent values were very close together so this interpolation was quite satisfactory. In these cases, the pairs of adjacent row numbers utilized are indicated for Region 2 over the abscissa of the plot.

Finally, it should be pointed out that in some cases the ranges of values of G_c/G_j did not completely overlap. Where possible, points for comparison were then calculated from the uniform array initial crossflow data from Part I of this report. The row numbers are again indicated and also marked by an asterisk.

Finally, included on each plot are the Nu (or St) values calculated from the correlation originally developed in [2,11]. This correlation was based entirely on the data from the prior comprehensive series of uniform array geometry tests. The correlation gives Nu = fcn(Re_j, G_c/G_j, x_n/d, y_n/d, z/d). The specific form used was Eq. (5.1) from [2], also given as Eq. (10) in [11]. The uncertainty interval for the correlatioin was $\pm$ 11% for a 95% confidence level. It was applied at each spanwise row of the nonuniform arrays tested. In Figs. 10.1 through 10.12 the position of the points so calculated is indicated by a solid line to facilitate comparison with the data points.

The nonuniform array data and the comparisons presented in these figures will now be discussed in more detail in two major categories: first, the effects of a nonuniform hole spacing with emphasis on the spanwise spacing, Figs. 10.1 through 10.8; and second, the effects of a nonuniform hole diameter, Figs. 10.9 through 10.12.

10.2.1 Nonuniform Hole Spacings

Examination of the nonuniform array data in Figs. 10.1 and 10.2 indicates that a doubling of y_n from Region 1 to Region 2 can cause a significant decrease in Nu across the transition line, the change being larger when it occurs upstream (Fig. 10.1) as compared to occurring further downstream (Fig. 10.2). Figs. 10.3, 10.4, and 10.5 indicate the reverse transition (reducing y_n by one-half) causes less significant changes across the transition line, especially when the transition occurs far downstream (Figs. 10.4 and 10.5). However, it is clear that reducing y_n from Region 1 to Region 2

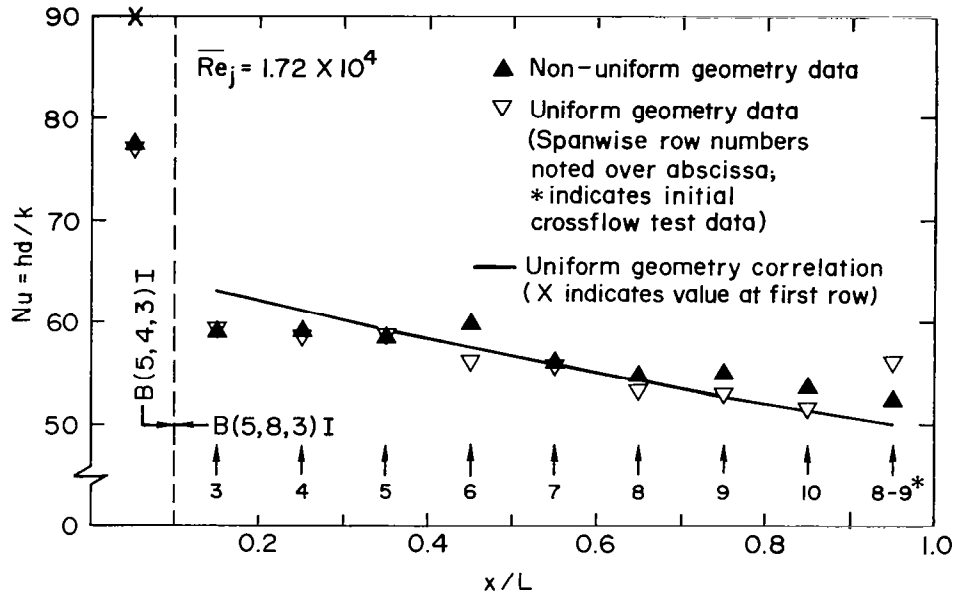

Fig. 10.1 Nusselt number data for nonuniform y_n array compared with uniform array data and correlation. Test #5Y.

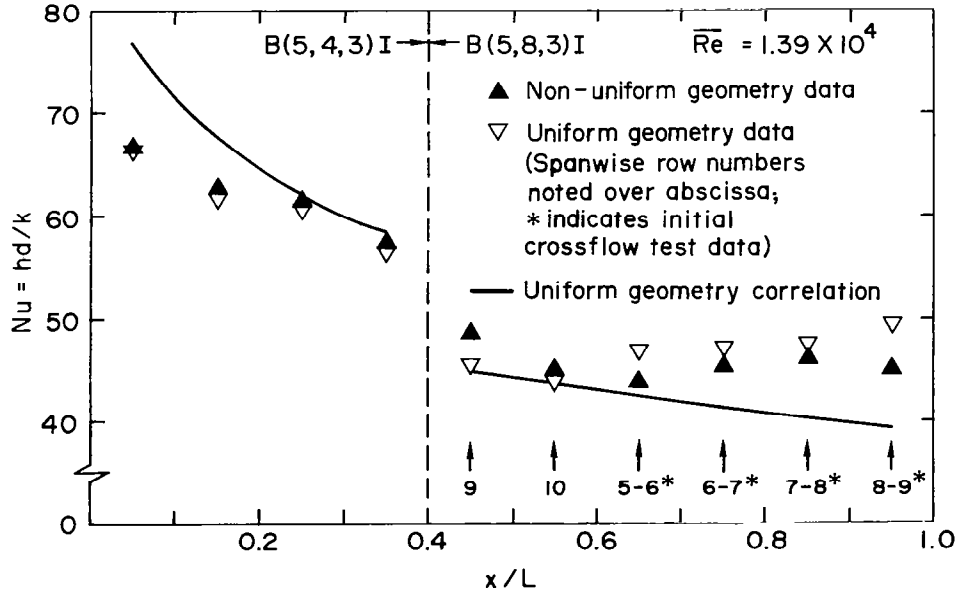

Fig. 10.2 Nusselt number data for nonuniform y_n array compared with uniform array data and correlation. Test #3Y.

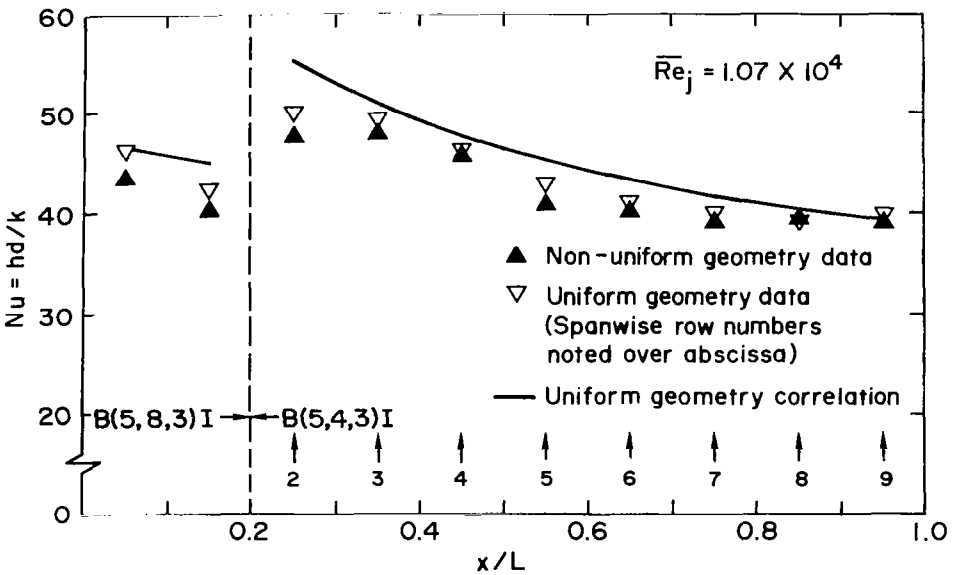

Fig. 10.3 Nusselt number data for nonuniform y_n array compared with uniform array data and correlation. Test #4Y.

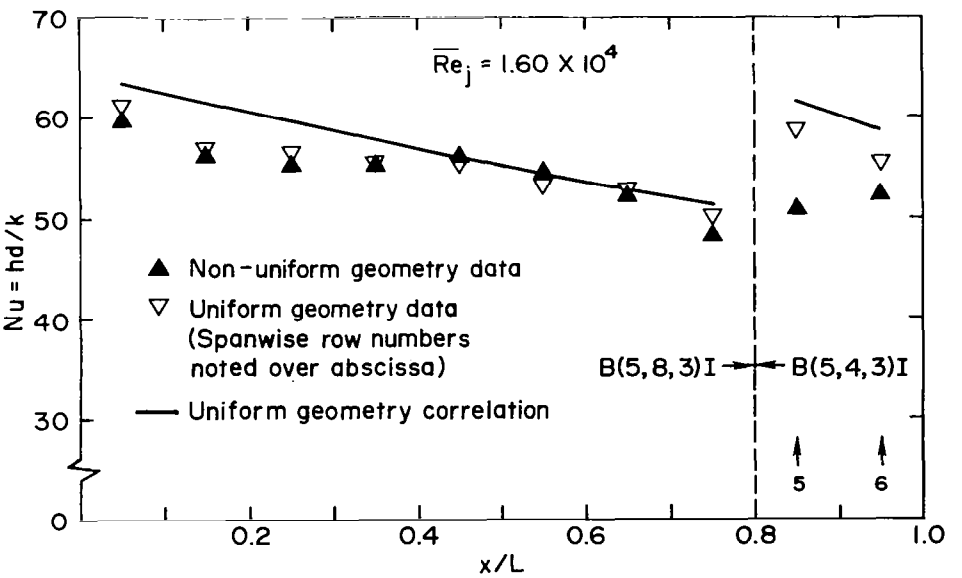

Fig. 10.4 Nusselt number data for nonuniform y_n array compared with uniform array data and correlation. Test #2Y.

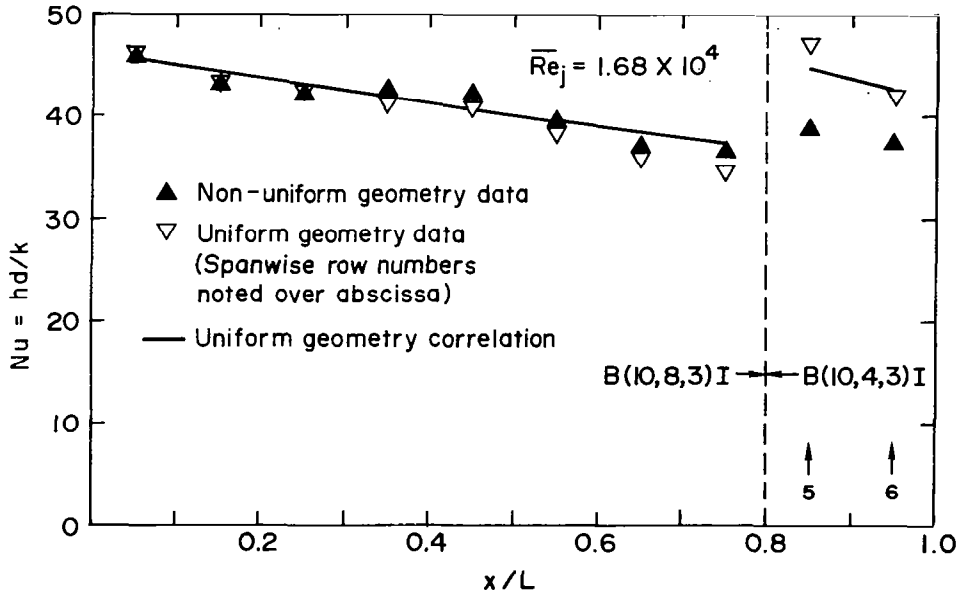

Fig. 10.5 Nusselt number data for nonuniform y_n array compared with uniform array data and correlation. Test #6Y.

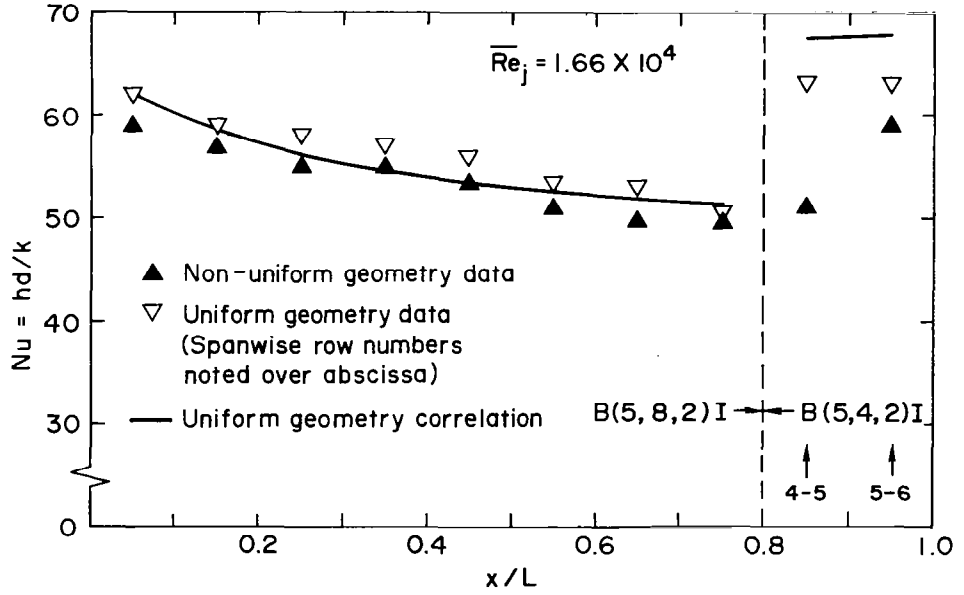

Fig. 10.6 Nusselt number data for nonuniform y_n array compared with uniform array data and correlation. Test #7Y.

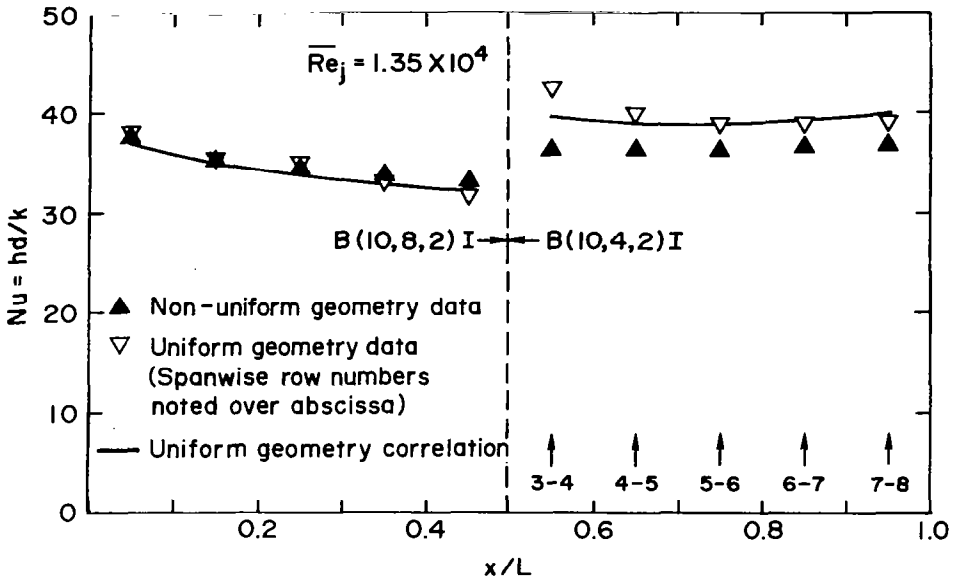

Fig. 10.7 Nusselt number data for nonuniform y_n array compared with uniform array data and correlation. Test #9Y.

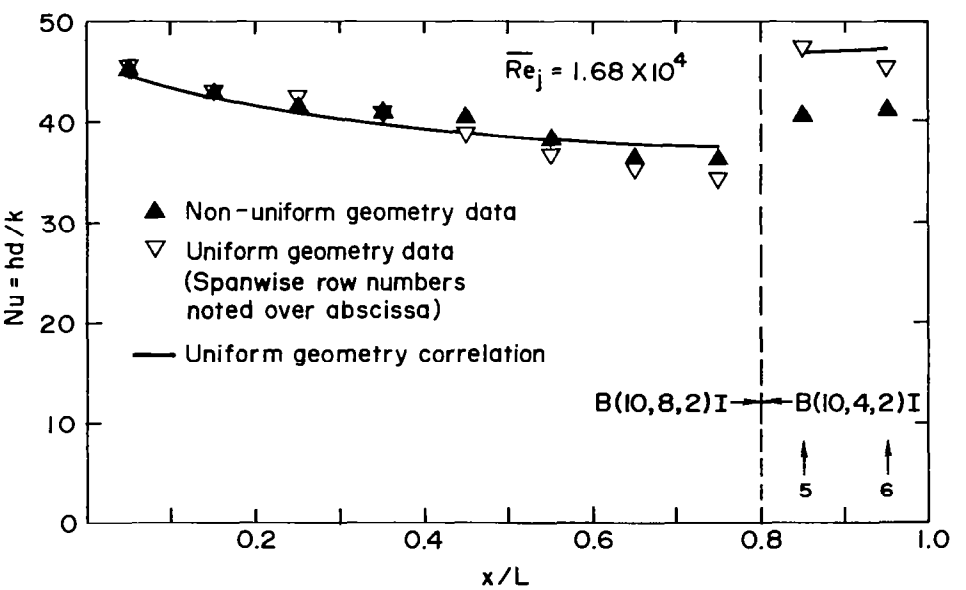

Fig. 10.8 Nusselt number data for nonuniform y_n array compared with uniform array data and correlation. Test #8Y.

(Figs. 10.3 through 10.8) always increases Nu across the transition line to some degree, and in a more pronounced fashion when z/d = 2 (Figs. 10.6 through 10.8) than when z/d = 3 (Figs. 10.3 through 10.5). In most of these cases the downward trend of Nu in Region 1 is halted in Region 2 and sometimes reversed.

Turning now to the uniform array data point and correlation comparisons, the results are seen to be quite consistent in an overall sense for Figs. 10.1 through 10.8 considered as a group. For Region 1 the data points from the nonuniform array tests are consistent with those from the uniform array in every case. Indeed, the largest difference (Region 1) is just 6.3% with an average difference of only 2.5%. With respect to any given row in Region 1 of the nonuniform array, details of the flow field history upstream of the row should be identical with the history for the corresponding row in the uniform array. Flow field conditions downstream of the transition line would not be expected to exert any significant influence on the flow field upstream of the transition line. Therefore, the uniform array heat transfer data would be expected to accurately represent the nonuniform array heat transfer characteristics in Region 1, as is well verified by the data point comparisons just discussed. It might also be emphasized that these nonuniform array jet plates were the same ones used for the uniform array tests, but with selected holes plugged as described in Section 8. Thus, it was possible to insure that the most minute details of the machined jet holes were the same in these two sets of tests. The good consistency of the data for Region 1 provides confidence that the differences sometimes observed in Region 2 immediately downstream of the transition line represent real effects. These effects will now be discussed.

There is little difference observed between the data points even at the first row following the transition line when y_n is doubled from Region 1 to Region 2 (Figs. 10.1 and 10.2). However, it does appear from Fig. 10.2 that at this row the nonuniform array data point indicates a somewhat larger Nu than existed for the uniform array (7%). Conversely when y_n is cut in half, the nonuniform array point at the first row in Region 2 always falls below the uniform array point (Figs. 10.3 through 10.8), by anywhere from 13 to 19%, except for Fig. 10.3 where it falls below by only 5%. Since the data points are being compared for the same G_j (which is based on jet hole area) and same

G_c (which is based on channel cross-sectional area), significant differences in Nu are undoubtedly related to local differences in the two flow fields. These differences arise due to differing histories of the crossflow approaching respective rows being compared, even though the crossflow rate magnitudes are the same. Qualitative explanations of the trends of these Nu data point comparisons may be attempted, but must remain tentative because of the great complexity of the interacting cross and jet flows within a two-dimensional array of jets. The explanations given below are related largely to tne consideration that the spanwise distribution of the crossflow is not uniform but rather periodic with a period equal to the spanwise hole spacing.

Each jet in the first row of Region 2 (call it Row n), it tne row is considered as part of a uniform array, has a jet immediately upstream in Row n-1. Each jet in Row n is ''protected'' somewhat from tne accumulated crossflow from rows upstream of Row n-1 because of the bifurcation of this crossflow by the jets of Row n-1. As part of a nonuniform array in which y_n is reduced by one-half for Region 2, only alternate jets in the Row n have a jet immediately upstream. Therefore, for the nonuniform array fewer jets in Row n are ''protected'' by jets in Row n-1. These jets are then more diffused and their heat transfer performance more degraded than it would be for Row n considered as part of a uniform array. The Nusselt numbers in Figs. 10.3 through 10.8 for the first row of Region 2 were already observed to be smaller than the corresponding value based on uniform array data.

When y_n is doubled (Figs. 10.1 and 10.2), the first row upstream of Region 2 (again call it Row n-1) has alternate jets without a jet immediately downstream in Row n. The crossflow from these jets, as well as accumulated crossflow from further upstream jets in the same line, can flow between adjacent jets in Row n. Each jet in Row n is thus directly subjected to a smaller crossflow than if it were part of the uniform array. The tendency would then be for the heat transfer coefficients at Row n in the nonuniform array to be larger. This tendency is reflected in Fig. 10.2, though tne difference is small. No difference whatever shows up in Fig. 10.1.

Comparing Fig. 10.1 to 10.2, and Fig. 10.3 to Figs. 10.4 through 10.8 it appears that data point differences immediately downstream of the transition line are larger when the transition line is farther downstream. For all of

the cases where a significant difference between the corresponding data points occurs in the first row after the transition line, the difference becomes noticeably smaller at the second row after the transition line and continues to decrease at succeeding rows. The use of the correlation appears to be as well-justified for nonuniform y_n arrays as it is for uniform arrays, except, in some cases, at the first one or two rows after the transition line.

Heat transfer data for the nonuniform x_n array tested (Test #1X, Table 8.1) is included in Appendix E, Table E.2. For this array x_n was reduced by one-half from Region 1 to Region 2. No plot is included because after plugging alternate rows in the original uniform array to form Region 1, the remaining rows did not match up with the test plate segments such that Nu values properly resolved over the x_n increments associated with each row could be calculated for comparison with the uniform array results. However, Nusselt numbers for the two rows in Region 2 could be compared with uniform array results and were found to be in excellent agreement, indicating no effect even at the first row downstream of the transition line.

10.2.2 Nonuniform Hole Diameters

Stanton number ($St = h/c_p\bar{G}_j$) profiles for four different arrays with nonuniform hole diameters are presented in Figs. 10.9 through 10.12. The general format and type of information contained in these figures were explained in detail at the outset of Section 10.2, and are similar to the figures in the preceding subsection 10.2.1. Each of the present figures, however, contains two plots, one for each of two different tests of a single nonuniform array. The conditions for each of the two tests were identical except for the magnitude of the total jet flow rate, which for the lower plot in each figure was from about 1.5 to 2.5 times the value for the upper plot. This difference in jet flow rates is reflected in the magnitudes of the mean jet Reynolds numbers indicated for each region of the nonuniform arrays. Since the Reynolds numbers are defined in terms of the jet hole diameter, mean values are specified for each of the two uniform sub-arrays (regions).

Based on the specific values of the geometric parameter sets (x_n/d, y_n/d, z/d) for which prior uniform array heat transfer tests were conducted, only two pairs of these parameter sets could be combined to form nonuniform arrays

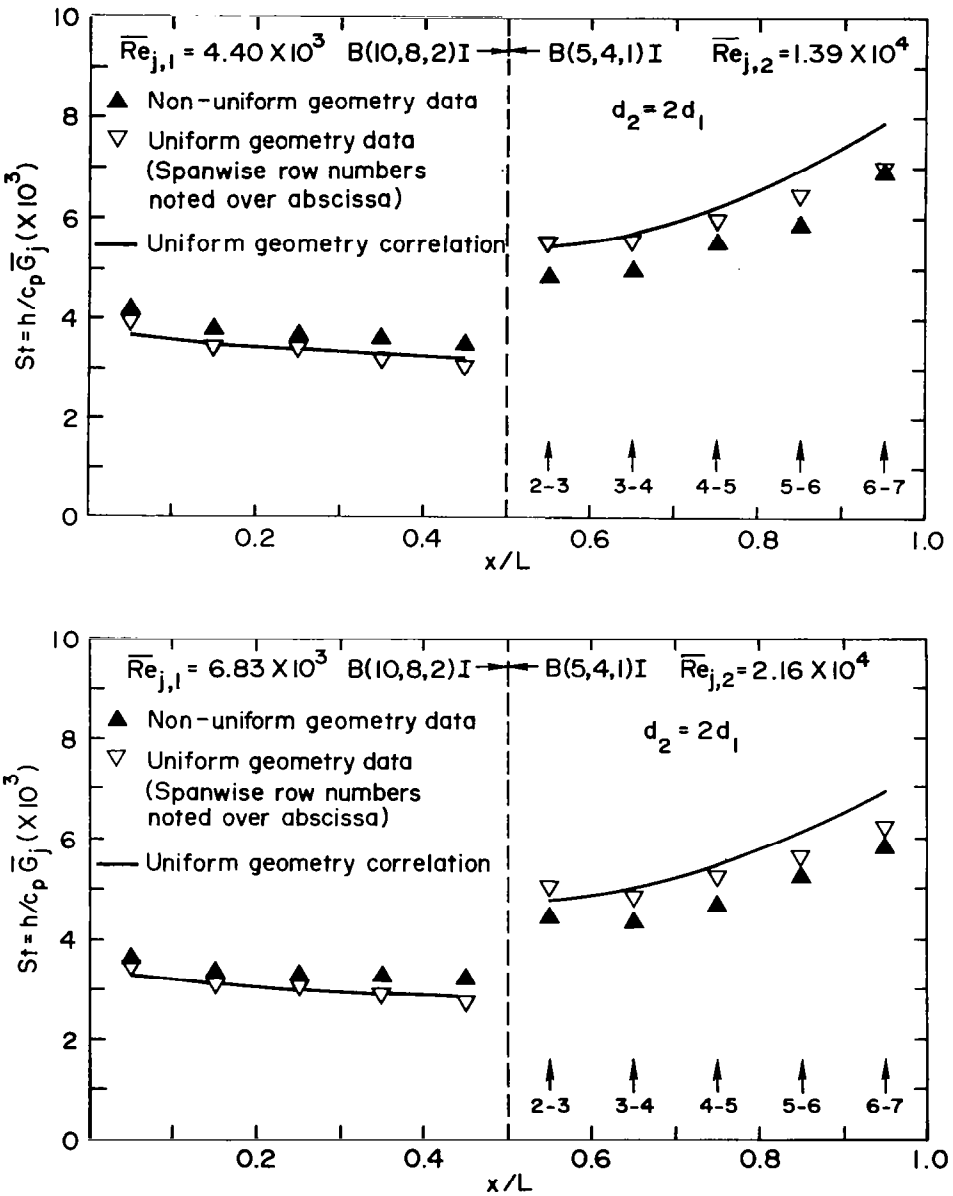

Fig. 10.9 Stanton number data for nonuniform diameter array compared with uniform array data and correlation. Test #1D.

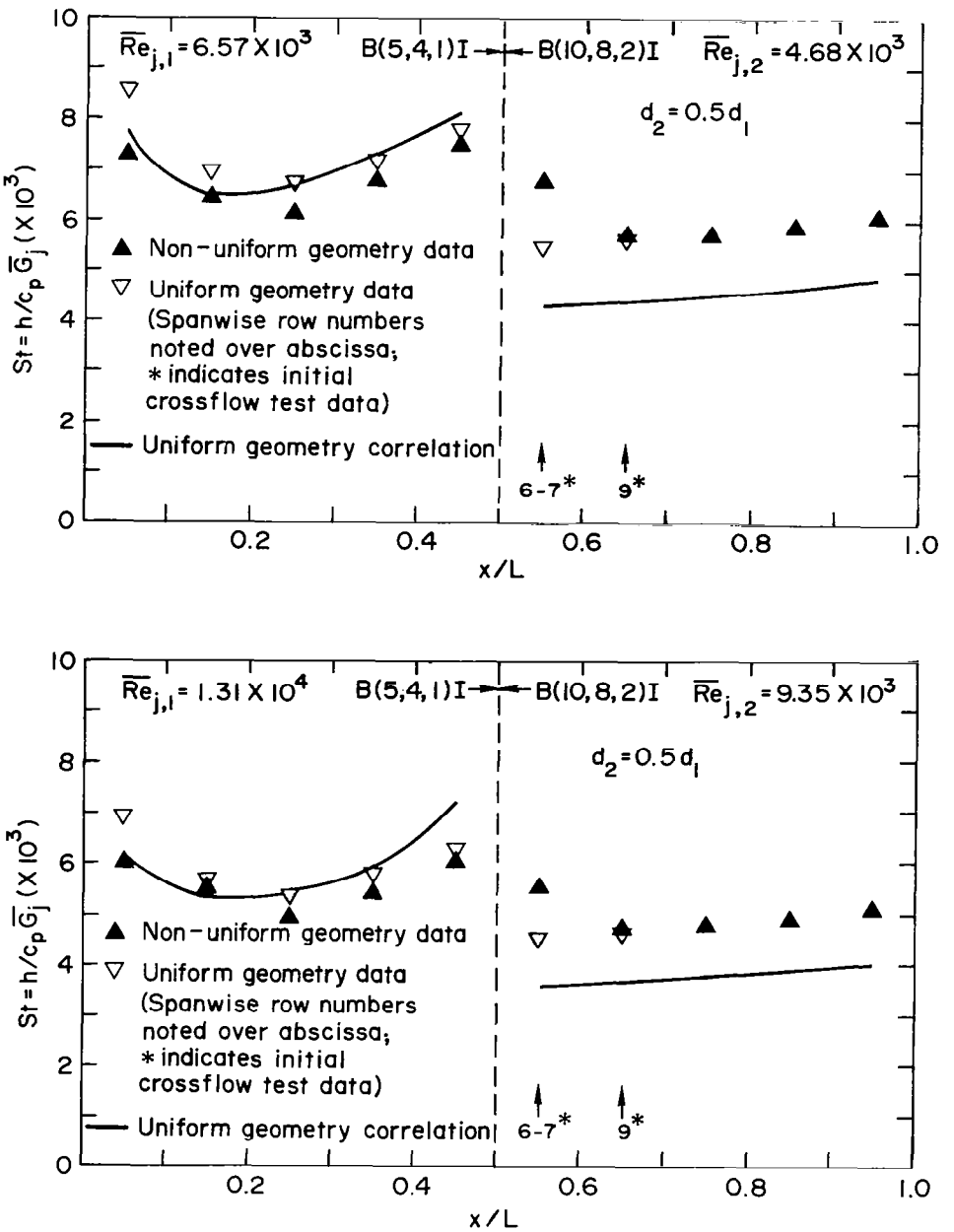

Fig. 10.10 Stanton number data for nonuniform diameter array compared with uniform array data and correlation. Test #2D.

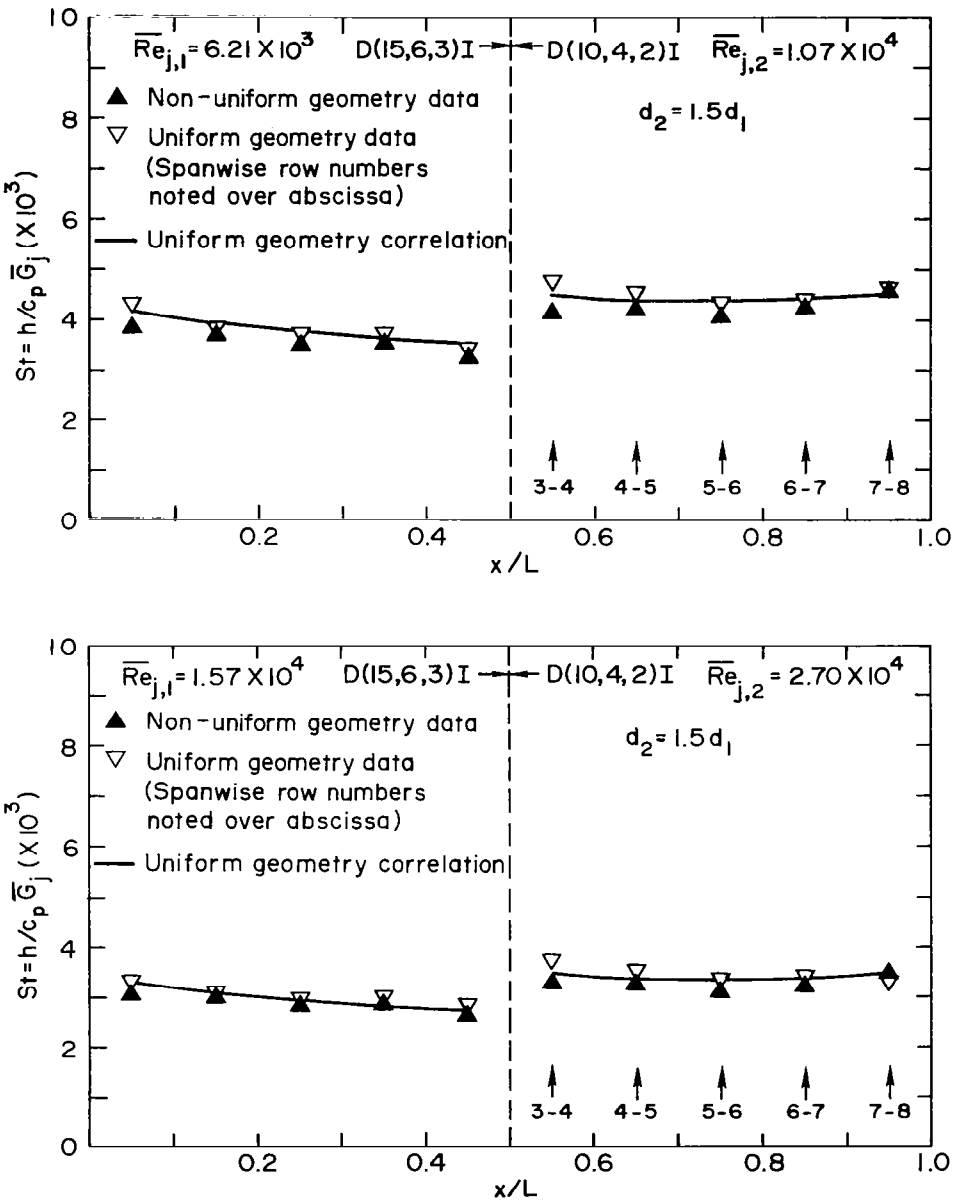

Fig. 10.11 Stanton number data for nonuniform diameter array compared with uniform array data and correlation. Test #3D.

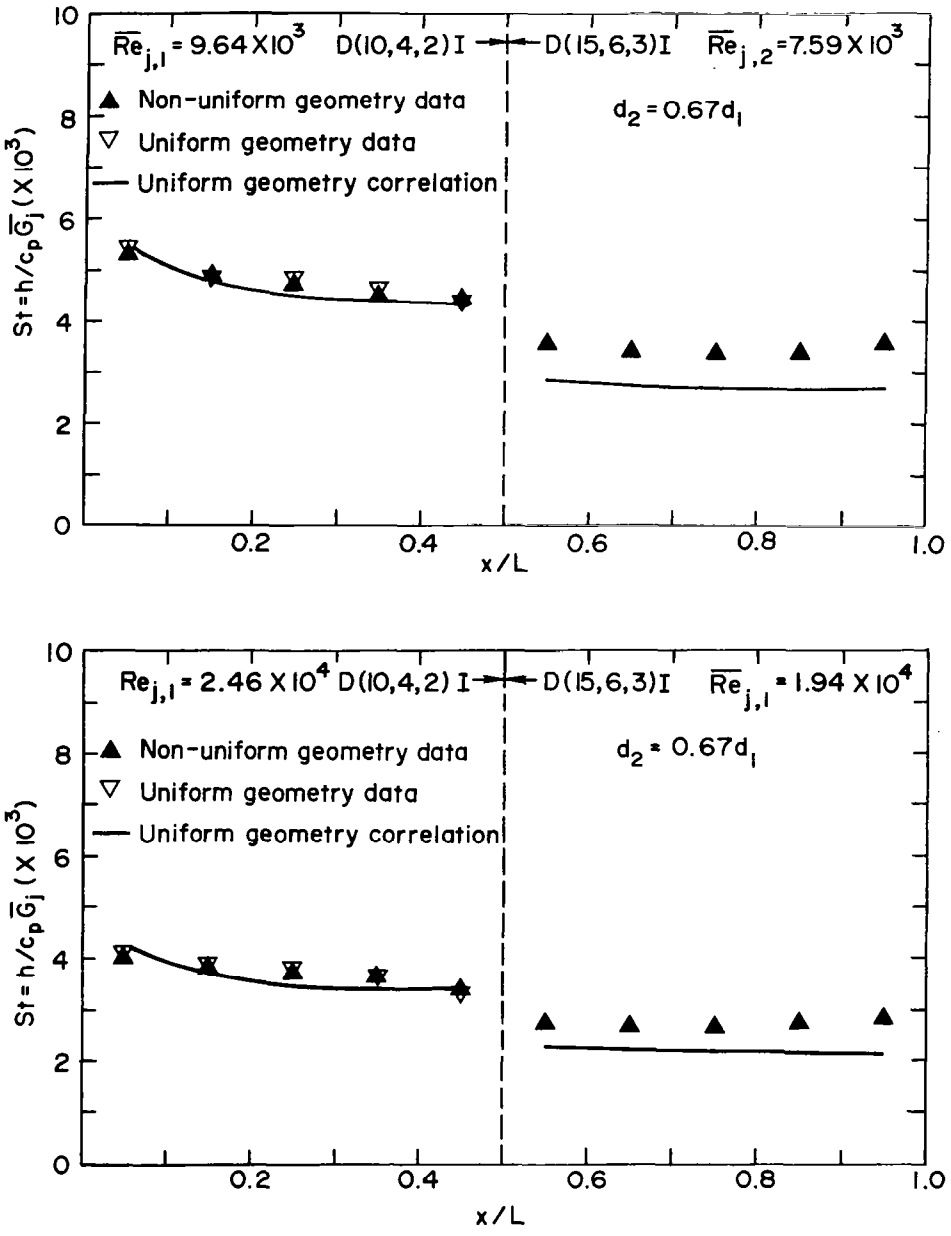

Fig. 10.12 Stanton number data for nonuniform diameter array compared with uniform array data and correlation. Test #4D.

in which the hole diameter was the only nonuniform geometric parameter. These pairs were [(10,8,2), (5,4,1)] and [(15,6,3), (10,4,2)]. Note that these represent significant changes in the hole area (and, therefore, open area ratio) by factors of 4 and 2.25, respectively. As already indicated in Section 8 two new jet plates each having five spanwise rows of holes at the smaller diameter and five at the larger diameter were machined. These could be mounted in the test rig with either the small holes or the large holes upstream. This resulted in the four nonuniform arrays for which data is presented in Figs. 10.9 through 10.12.

Tests were run at two different total jet flow rates because in some cases no single flow rate would result in local row jet Reynolds numbers for both regions of the array which were within the ranges covered by the uniform array tests for the corresponding geometries. Therefore, extrapolation of some of the uniform array data was necessary to complete these comparisons. However, the trends and comparisons appearing in the two plots of each figure are quite similar irrespective of the flow rate (i.e., Reynolds number) level, so that in discussing these results no further reference will be made to this distinction.

The nonuniform array Stanton number data points (upright solid triangles) in Figs. 10.9 and 10.11 show that increasing the hole diameter for Region 2 relative to Region 1 results in higher heat transfer coefficients in Region 2 than in Region 1; Figs. 10.10 and 10.12 show the reverse trend for a decrease in hole diameter. The overall changes across the transition line are more pronounced when the diameters in the respective regions differ by a factor of 2 (Figs. 10.9 and 10.10) than when they differ by a factor of 1.5 (Figs. 10.11 and 10.12).

When Region 2 has the larger diameter (e.g., Fig. 10.9), the ratio of hole area to heat transfer surface area is also larger so that even for the same jet velocities one might expect higher heat transfer coefficients. Examination of the corresponding flow distribution (Fig. 9.5) indicates Region 2 also has larger jet velocities for reasons already discussed in Section 9. Thus, two effects combine to result in higher heat transfer coefficients in Region 2 relative to Region 1.

When Region 2 has the smaller diameter (e.g., Fig. 10.10), the open area

ratio effect, assuming the same jet velocities, would tend to reduce the heat transfer coefficients. The corresponding flow distribution (Fig. 9.6) shows the jet velocities in Region 2 to be equal to or higher than those of Region 1 just as they were for the contrasting conditions of the preceding paragraph. However, here the counteracting open area ratio effect apparently dominates enough to cause lower heat transfer coefficients in Region 2 relative to Region 1.

The agreement of the nonuniform array data points for Region 1 with the uniform array data points is quite good for Figs. 10.11 and 10.12, as it was for the nonuniform y_n cases (Section 10.2.1). It is not as satisfactory for Figs. 10.9 and 10.10, particularly 10.10. This may be due, at least in part, to the fact that these were separately machined jet plates from those used for the uniform array tests; and, since Figs. 10.9 and 10.10 involve a z/d of unity, microscale differences in jet hole geometries may have a noticeable effect for this small standoff distance. In addition, the jet plate thickness, b, at the jet hole locations was not equal to one hole diameter in both regions of these jet plates (see Section 8), as it was for every hole in the uniform arrays, though this was also the case for the nonuniform jet plates of Figs. 10.11 and 10.12 where the Stanton number data point differences in Region 1 are insignificant.

Turning now to Region 2 it must first be pointed out that no uniform array data, with or without initial crossflow, had G_c/G_j values in the necessary range for comparisons at the last three rows of the array of Fig. 10.10 or for the entire Region 2 of the array of Fig. 10.12. These points were also, of course, outside the applicable range of the correlation as were those for the first two rows of Region 2, Fig. 10.10, where initial crossflow data had to be used for comparison. Otherwise the curves based on the correlation are consistent with the data for both regions in all of these figures.

What is apparently an effect of the upstream history of the flow field again shows up immediately downstream of the transition line when the corresponding uniform and nonuniform array heat transfer coefficients are compared, just as it did for the nonuniform y_n cases. The difference is most significant in Fig. 10.10, but disappears at the second row of Region 2, so here the significant ''entrance length'' is no more than one row. Though the

comparisons for these nonuniform diameter arrays are not as definitive in all cases as they were for the nonuniform y_n arrays, it appears that conclusions similar to those drawn at the close of Section 10.2.1 apply here as well.

10.2.3 Additional Comparisons

The previous two subsections have been concerned primarily with the nature of the nonuniform array heat transfer coefficient profiles and consideration of how well these streamwise resolved heat transfer coefficients may be predicted from uniform array data or from the correlation based on uniform array data. The predictions require knowledge of the parameter set (Re_j, G_c/G_j, x_n/d, y_n/d, z/d) at the spanwise row of interest in the nonuniform array coupled with knowledge of the dependence of Nu (or St) on the parameter set for a uniform array, either from the uniform array data itself or from the correlation based upon it.

Here an example of a direct comparison between a two-region nonuniform array and the two uniform arrays having the same geometric parameter sets (x_n/d, y_n/d, z/d) is provided. The array of Test # 3Y (Fig. 10.2) with a nonuniform y_n is used as the example. The basis of comparison must, however, be precisely defined. The heat transfer characteristics of the arrays are first compared for the same total jet flow rate per unit of heat transfer surface area (or equivalent jet plate surface area), $\overline{G}_j^*$. For jet plates of uniform hole diameter the comparison may be made for the same value of mean jet Reynolds number based on this superficial mass velocity, $\overline{Re}_j^*$. The comparison is presented in Fig. 10.13. The Nu profile for the nonuniform array is more highly nonuniform than either profile for the corresponding uniform arrays, and falls between these profiles. The nonuniform $\overline{Nu}$ falls about midway between the uniform array values in this example. It is interesting to observe that in both Regions 1 and 2 the nonuniform array Nusselt numbers lie closer to the values for the uniform array with the differing y_n/d than they do to the values for the uniform array with the same y_n/d.

The same cases are compared again in Fig. 10.14 on a different basis. Here the comparison is for the same pressure drop from jet plenum to jet array channel exit. This pressure drop is essentially that existing across the final downstream row of holes in the array (Row 10 for the present arrays).

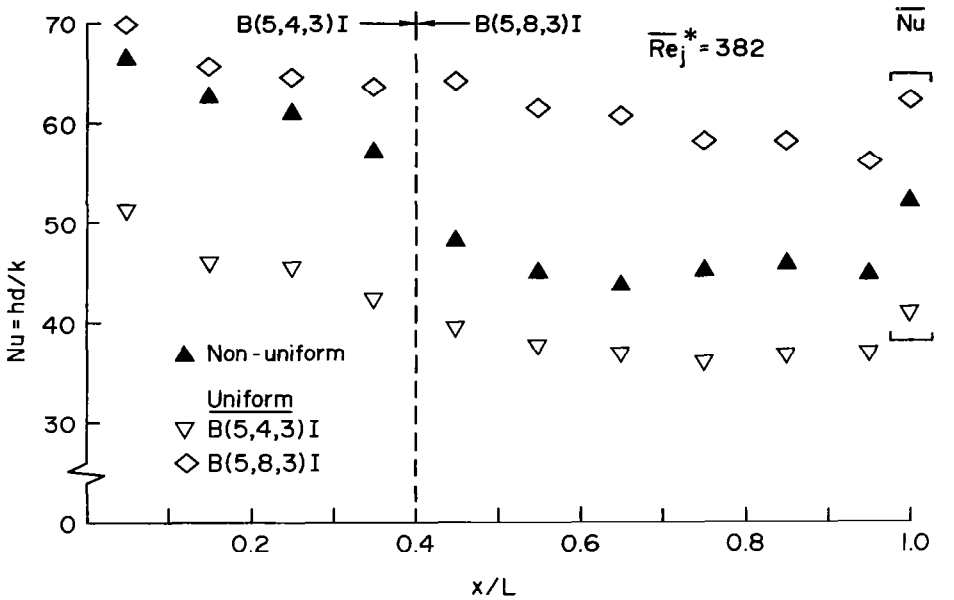

Fig. 10.13 Nusselt number profile for nonuniform y_n array compared with profiles for corresponding uniform array geometries for same total jet flow rate.

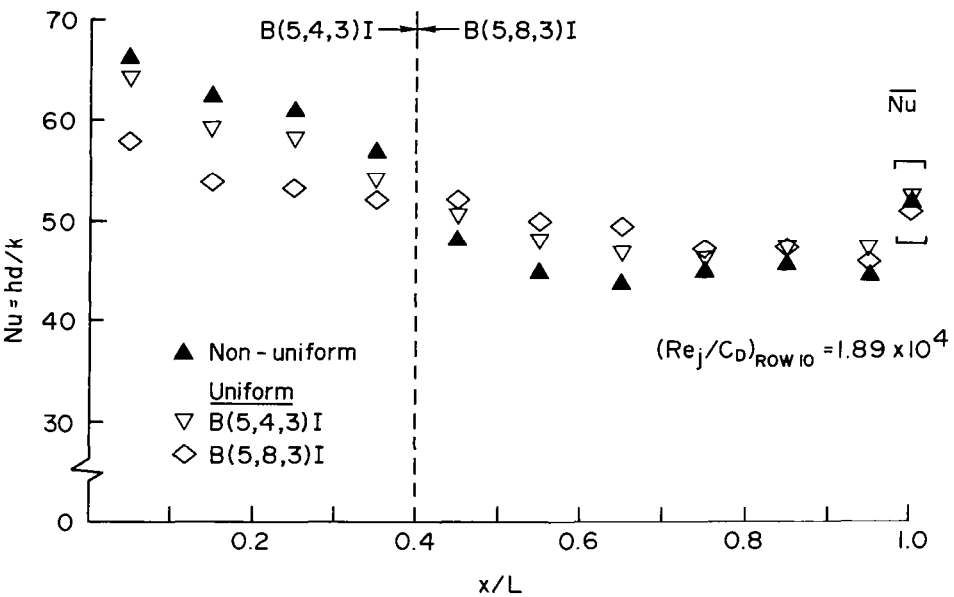

Fig. 10.14 Nusselt number profile for nonuniform y_n array compared with profiles for corresponding uniform array geometries for same pressure drop.

For incompressible flow the pressure drop will be the same if G_j (or Re_j) is the same, assuming the same discharge coefficient for each array. For the arrays compared here C_D differed slightly. Taking this into account the same pressure drop will exist for the same value of Re_j/C_D at Row 10. The value at which the comparison was made is specified on the figure. Compared on this basis the Nu profiles differ less than when compared for the same total jet flow rate. The mean values for this example are almost identical, but as before the mean for the nonuniform array lies between the uniform array values. Now, however, the nonuniform array has larger Nusselt numbers than either uniform array in Region 1 but smaller values than either in Region 2.

Both of these comparisons serve to illustrate that, depending on the designer's flow and pressure drop constraints, the use of nonuniform arrays can serve to adjust the level and distribution of the cooling provided by the array, providing the flexibility to better match the external heat load magnitude and distribution. Similar comparisons, as desired for other cases, may be made utilizing the flow distribution and heat transfer data tabulated in the Appendices of this report and in [1].

11. CONCLUDING REMARKS (PART II)

A midchord internal cooling scheme utilizing two-dimensional arrays of jets, in addition to the high heat transfer coefficients possible, provides the flexibility and potential for optimizing cooling performance by tailoring the array geometry to appropriately match the external thermal loading. This may often require the use of arrays having nonuniform geometric parameter values. Since it is not feasible to generate measurements or test results for every possible arrangement the designer may need to consider in his performance and trade-off analyses, it is important that he have available some means of calculating expected performance for various array geometries.

In Part II of this report, experimental results for flow distributions and streamwise resolved heat transfer coefficients for two-region nonuniform arrays in a noninitial crossflow configuration have been presented. A theoretically based flow distribution model for the nonuniform arrays was also developed and validated by comparison with the measured flow distributions. With the aid of the flow distribution model, the nonuniform array spanwise averaged heat transfer coefficients, resolved to one streamwise hole spacing, were compared in detail with prior uniform array data [1,8], and with a correlation based on the uniform array data [2,11].

Based on these comparisons it was verified that reliable uniform array heat transfer data can be used to determine heat transfer coefficients for the upstream region of a nonuniform array. In addition, it was found that for downstream regions accurate determinations can be made beyond the second row following the geometric transition line, and for many conditions at the first and/or second rows as well (put more concisely, the maximum significant ''entrance length'' following the geometric transition appears to be two rows). Heat transfer coefficients for ''entrance length'' rows based on uniform array data may be larger or smaller than the actual values for the nonuniform array depending on the type of geometric transition. If the spanwise spacing is increased downstream the uniform array based value may be somewhat low. If it is decreased the value will tend to be high. If the diameter is increased the uniform array based value will tend to be high, while for a decrease in diameter it will tend to be low. The largest

difference observed for any nonuniform array tested was about 20%. In particular cases, expected differences between an actual nonuniform array heat transfer coefficient for a row immediately downstream of a geometric transition and the uniform array based value may best be judged by referring to the specific comparisons presented in Section 10.2.

Finally, it was found that heat transfer coefficient predictions for nonuniform arrays based on the correlation originally presented in [2,11] may, in general, be made with the same confidence as for uniform arrays as long as the cross-to-jet velocity ratios are within the range of results on which the correlation was based. Exceptions occur, in some cases, for the first one or two rows immediately downstream of the geometric transition in the nonuniform array. At these rows the correlation may still be applied but with more caution because the confidence will not be as high.

REFERENCES

1. Florschuetz, L.W., Metzger, D.E., Takeuchi, D.I., and Berry, R. A., Multiple Jet Impingement Heat Transfer Characteristic - Experimental Investigation of Inline and Staggered Arrays with Cross-flow, NASA Contractor Report 3217, Department of Mechanical Engineering, Arizona State University, Tempe, January 1980.

2. Florschuetz, L.W., Metzger, D.E., and Truman, C.R., Jet Array Impingement with Crossflow--Correlation of Streamwise Resolved Flow and Heat Transfer Distributions, NASA Contractor Report 3373, Department of Mechanical Engineering, Arizona State University, Tempe, January 1981.

3. Kercher, D.M., and Tabakoff, W., ''Heat Transfer by a Square Array of Round Air Jets Impinging Perpendicular to a Flat Surface Including the Effect of Spent Air,'' ASME Journal of Engineering for Power, Vol. 92, No. 1, Jan. 1970, pp. 73-82.

4. Metzger, D.E. and Korstad, R.J., ''Effects of Cross Flow in Impingement Heat Transfer,'' ASME Journal of Engineering for Power, Vol. 94, 1972, pp. 35-41.

5. Gauntner, J.W., Gladden, H.J., Gauntner, D.J., and Yeh, F.C., ''Crossflow Effects on Impingement Cooling of a Turbine Vane,'' NASA TM X-3029, March 1974.

6. Bouchez, J.P. and Goldstein, R.J., ''Impingement cooling From a Circular Jet in a Crossflow,'' International Journal of Heat and Mass Transfer, Vol. 18, 1975, pp. 719-730.

7. Sparrow, E.M., Goldstein, R.J., and Rouf, M.A., ''Effect of Nozzle-Surface Separation Distance on Impingement Heat Transfer for a Jet in a Crossflow,'' ASME Journal of Heat Transfer, Vol. 97, 1975, pp. 528-533.

8. Metzger, D.E., Florschuetz, L.W., Takeuchi, D.I., Behee, R.D., and Berry, R.A.,''Heat Transfer Characteristics for Inline and Staggered Arrays of Circular Jets with Crossflow of Spent Air,'' ASME Journal of Heat Transfer, Vol. 101, 1979, pp. 526-531.

9. Florschuetz, L.W., Berry R.A., and Metzger, D.E., ''Periodic Streamwise Variations of Heat Transfer Coefficients for Inline and Staggered Arrays of Circular Jets with Crossflow of Spent Air,'' ASME Journal of Heat Transfer, Vol. 102, 1980, pp. 132-137.

10. Saad, N.R., Mujumdar, A.S., Abdel Messeh, W., and Douglas, W.J.M., ''Local Heat Transfer Characteristics for Staggered Arrays of Circular Impinging Jets with Crossflow of Spent Air,'' ASME Paper 80-HT-23, 1980.

11. Florschuetz, L.W., Truman C.R., and Metzger, D.E., ''Streamwise Flow and Heat Transfer Distributions for Jet Array Impingement with Crossflow ,'' ASME Journal of Heat Transfer, Vol. 103, 1981, pp. 337-342.

12. Fluid Meters: Their Theory and Application, Fifth Editions ASME, New York, 1959.

13. Kline, S.J. and McClintock, F., ''Describing Uncertainties in Single Sample Experiments,'' Mechanical Engineering, Vol. 75, January 1953, pp. 3-8.

14. Damerow, W.P., Murtaugh, J.C., and Burggraf, F., Experimental and Analytical Investigation of the Coolant Flow Characteristics in Cooled Turbine Airfoils, NASA Contractor Report 120883, General Electric Company, Cincinnati, Ohio, June 1972.

15. Meitner, P.L. and Hippensteele, S.A., Experimental Flow Coefficients of a Full-Coverage Film-Cooled Turbine Vane Chamber, NASA TP-1036, September 1977.

16. Dyban, E.P., Mazur, A.I., and Golovanov, V.P., ''Heat Transfer and Hydrodynamics of an Array of Round Impinging Jets with One-Sided Exhaust of the Spent Air,'' International Journal of Heat and Mass Transfer, Vol. 23, 1980, pp. 667-676.

17. Martin, H., ''Heat and Mass Transfer Between Impinging Gas Jets and Solid Surfaces,'' Advances in Heat Transfer, Vol. 13, Academic Press, New York, 1977, pp. 1-60.

18. Kays, W.M., Convective Heat and Mass Transfer, McGraw-Hill, New York, 1966, Chapter 6.

19. Goldstein, R.J., ''Film Cooling,'' Advances in Heat Transfer, Vol. 7, 1971, pp. 321-379.

20. Sparrow, E.M., Lloyd, J.R., and Hixon, C.W., ''Experiments on Turbulent Heat Transfer in an Asymmetrically Heated Rectangular Duct,'' ASME Journal of Heat Transfer, Vol. 88, 1966, pp. 170-174.

21. Tan, H.M. and Charters, W.W.S., ''An Experimental Investigation of Forced-Convective Heat Transfer for Fully-Developed Turbulent Flow in a Rectangular Duct with Asymmetric Heating,'' Solar Energy, Vol. 13, 1970, pp. 121-125.

22. McAdams, W.H., Nocolai, A.L., and Keenan, J.H., ''Measurements of Recovery Factors and Coefficients of Heat Transfer in a Tube for Subsonic Flow of Air,'' Transactions AIChE, Vol. 42, 1946, pp. 907-925.

APPENDIX A

DERIVATION OF FLOW DISTRIBUTION MODEL

The details of formulating the flow distribution model, Eq. (4.6), in terms of the dimensionless crossflow velocity $\tilde{G}_c$ are presented here. For constant P_o, the elimination of the channel pressure P from Eqs. (4.3) and (4.4) results in

$$\frac{G_j^*}{(A_o^* C_D)^2}\left(\frac{dG_j^*}{dx} - G_j^* \frac{1}{C_D}\frac{dC_D}{d(G_c/G_j)}\frac{d(G_c/G_j)}{dx}\right) = 2G_c\frac{dG_c}{dx} + \frac{f}{z}G_c^2 \qquad (A.1)$$

The elimination of G_j in $d(G_c/G_j)/dx$ may be achieved by use of the chain rule

$$\frac{d(G_c/G_j)}{dx} = \frac{1}{G_j}\frac{dG_c}{dx} + G_c\left(-\frac{1}{G_j^2}\right)\frac{dG_j}{dx} \qquad (A.2)$$

and with the aid of the relations $A_o^* G_j = G_j^*$ and Eq. (4.5)

$$\frac{d(G_c/G_j)}{dx} = \frac{A_o^*}{z} - \frac{G_c A_o^*}{z}\frac{1}{(dG_c/dx)^2}\frac{d^2G_c}{dx^2} \qquad (A.3)$$

The final dimensional form in terms of the crossflow velocity G_c is obtained by substitution of Eqs. (A.3) and (4.5) into Eq. (A.1):

$$\frac{z^2}{(A_o^* C_D)^2}\frac{dG_c}{dx}\left[\frac{d^2G_c}{dx^2} - \frac{1}{C_D}\frac{dC_D}{d(G_c/G_j)}\frac{dG_c}{dx}\frac{A_o^*}{z}\left(1 - \frac{G_c}{(dG_c/dx)^2}\frac{d^2G_c}{dx^2}\right)\right]$$

$$= 2G_c\frac{dG_c}{dx} + \frac{f}{z}G_c^2 \qquad (A.4)$$

Now rearranging this result to isolate d^2G_c/dx^2, and introducing the dimensionless parameters, $\tilde{G}_c = G_c/[(m_c + m_j)/wz]$ and $\tilde{x} = x/L$, yields Eq. (4.6).

APPENDIX B

FLOW DISTRIBUTION UNCERTAINTY AND SENSITIVITY ANALYSIS

Composite uncertainties for the experimental data and the sensitivities on the predictive model to uncertainties in input parameter values were estimated for both $G_j/\bar{G}_j$ and G_c/G_j according to the method of Kline and McClintock [13]. The resultant fractional uncertainty, on the basis of the uncertainties in the primary measurements, is computed by:

$$\frac{\omega_R}{R} = \left[\sum_{i=1}^{N} \left(\frac{\partial R}{\partial r_i} \frac{\omega_{r_i}}{R} \right)^2 \right]^{\frac{1}{2}} \tag{B.1}$$

where $R = R(r_1, r_2, \ldots, r_n)$, the dependent variable

ω_R = resultant or composite uncertainty in R

ω_{r_i} = uncertainty in r_i

Additional notations used in Appendix B which were not defined in the Nomenclature Section (p. v) are as follows:

Notation	Explanation
$( )^i$ or $( )^k$	Superscript i or k refers to a value at the i or k^{th} spanwise row of holes
$\omega( )$	Uncertainty or sensitivity in ( )
C	Used as a proportionality constant
A_o^i	Jet hole area of the i^{th} spanwise row
ΔP	Jet plenum-to-channel pressure difference (P_o-P)

B.1 Uncertainty Analysis on Experimental Results

The composite uncertainties on $G_j/\bar{G}_j$, G_c/G_j and C_D were computed by the use of Eq. (B.1). The forms of these equations, defined previously for the experimental results, were simplified to include only the independent variables of major uncertainty sources. These variables are the jet hole diameters, the channel height, the pressure readings P_o and ΔP, and the flowrates, m_j and m_c.

The mass velocity at row n with the assumption of incompressible flow and with constant C_D is

$$G_j^n = C\ C_D\ (P_o \cdot \Delta P)^{\frac{1}{2}} \tag{B.2}$$

Since P_o is the same across the rows, at row n of interest for Nc spanwise rows of holes $G_j/\bar{G}_j$ becomes

$$\frac{G_j^n}{\bar{G}_j} = \frac{Nc(\Delta P^n)^{\frac{1}{2}}}{(\Delta P^n)^{\frac{1}{2}} + \sum_{i=1}^{Nc}(\Delta P^i)^{\frac{1}{2}}} \tag{B.3}$$

There are Nc independent variables of ΔP^n and ΔP^i ($i = 1,2, \ldots, Nc;\ i \neq n$). Replacing by $R = G_j^n/\bar{G}_j$ in Eq. (B.3), the partial derivatives of $\partial R/\partial \Delta P^n$ and $\partial R/\partial \Delta P^k$ ($k = 1,2, \ldots, Nc;\ k \neq n$) were taken, and these were substituted into Eq. (B.1). The use of the approximation that assumes the magnitudes of ΔP^n and ΔP^i are the same yields

$$\frac{\omega_R}{R} = \left(\frac{1}{4}\,\frac{Nc - 1}{Nc}\right)^{\frac{1}{2}}\ \frac{\omega_{\Delta P}}{\Delta P} \tag{B.4}$$

where $R = G_j/\bar{G}_j$.

The two cases ($m_c/m_j = 0$ and $\neq 0$) of the uncertainty analysis were done

for G_c/G_j. For the $m_c/m_j = 0$ case the crossflow mass velocity at the n^{th} row, assuming incompressible flow, is

$$G_c^n = \left[C \sum_{i=1}^{n-1} C_D A_o^i (P_o \cdot \Delta P)^{\frac{1}{2}}\right] \quad /wz \tag{B.5}$$

The mass velocity ratio of crossflow, Eq. (B.5), to jetflow, Eq. (B.2), becomes

$$\left(\frac{G_c}{G_j}\right)^n = \frac{\pi}{4y_n} \frac{d^2}{z} \sum_{i=1}^{n-1} (\Delta P^i/\Delta P^n)^{\frac{1}{2}} \tag{B.6}$$

Then, the uncertainty in the ΔP parts may be obtained by the same method as $G_j/\bar{G}_j$:

$$\frac{\omega_R}{R} = \left(\frac{1}{4} \frac{n}{n-1}\right)^{\frac{1}{2}} \frac{\omega_{\Delta P}}{\Delta P} \tag{B.7}$$

where $R = \sum_{i=1}^{n-1} (\Delta P^i/\Delta P^n)^{\frac{1}{2}}$. Finally, the uncertainty in $(G_c/G_j)^n$ becomes

$$\frac{\omega_R}{R} = \left[\left(2 \frac{\omega_d}{d}\right)^2 + \left(\frac{\omega_z}{z}\right)^2 + \frac{1}{4} \frac{n}{n-1} \left(\frac{\omega_{\Delta P}}{\Delta P}\right)^2\right]^{\frac{1}{2}} \tag{B.8}$$

where $R = (G_c/G_j)^n$ with $m_c/m_j = 0$.

For the $m_c/m_j \neq 0$ case, the $(G_c/G_j)^n$ contains the additional term $[m_c/wzG_j^n = (MNc\pi d^2/4y_n z)(G_j^n/\bar{G}_j)]$ so that Eq. (B.6) is replaced by

$$\left(\frac{G_c}{G_j}\right)^n = \frac{\pi}{4} \frac{d^2}{y_n z} \left[\frac{MNc}{G_j^n/\bar{G}_j} + \sum_{i=1}^{n-1} (\Delta P^i/\Delta P^n)^{\frac{1}{2}}\right] \tag{B.9}$$

For the upstream row (n=1), the second term in the squared brackets drops and Eq. (B.9) becomes

$$\left(\frac{G_c}{G_j}\right)^1 = \frac{\pi}{4} \frac{d^2}{y_n z} \left(\frac{MNc}{G_j^1/\bar{G}_j}\right) \tag{B.10}$$

Therefore, the uncertainty in G_c/G_j at the first row is

$$\frac{\omega_R}{R} = \left[\left(2\,\frac{\omega_d}{d}\right)^2 + \left(\frac{\omega_z}{z}\right)^2 + \left(\frac{\omega_M}{M}\right)^2 + \left(\frac{\omega_{R1}}{R1}\right)^2\right]^{\frac{1}{2}} \qquad \text{(B.11)}$$

where $R = (G_c/G_j)^1$, and $R1 = G_j^1/\bar{G}_j$.

For the downstream rows, both terms in the squared brackets in Eq. (B.9) remain, and factoring the second term outside the brackets yields

$$\left(\frac{G_c}{G_j}\right)^n = \frac{\pi}{4}\,\frac{d^2}{y_n z}\left(\sum_{i=1}^{n-1}(\Delta P^i/\Delta P^n)^{\frac{1}{2}}\right)\left[\frac{MNc}{(G_j^n/\bar{G}_j)\sum_{i=1}^{n-1}(\Delta P^i/\Delta P^n)^{\frac{1}{2}}} + 1\right] \qquad \text{(B.12)}$$

By expressing $G_j^n/\bar{G}_j$ in terms of ΔP, the denominator of the first term in the squared brackets may be written as

$$\frac{Nc}{(\Delta P^{Nc})^{\frac{1}{2}}/\sum_{i=1}^{Nc-1}(\Delta P^i)^{\frac{1}{2}} + 1} \qquad \text{(B.13)}$$

evaluating n at the last row Nc. Since the uncertainty in ΔP contributes little to the uncertainty in the expression (B.13) (about 1/(Nc-1) of the uncertainty in ΔP^i itself if the magnitudes of all ΔP^i are assumed to be the same), the significant source of uncertainty inside the squared brackets in Eq. (B.12) is only the M. Finally, the uncertainty in G_c/G_j evaluated at the last row (n = Nc) becomes

$$\frac{\omega_R}{R} = \left[\left(\frac{\omega_{R2}}{R2}\right)^2 + \left(\frac{1}{1+A}\right)^2\left(\frac{\omega_M}{M}\right)^2\right]^{\frac{1}{2}} \qquad \text{(B.14)}$$

where $R = (G_c/G_j)^{Nc}$, $\omega_{R2}/R2$ is equal to the ω_R/R of Eq. (B.8), and $A = (G_j^{Nc}/\bar{G}_j)\sum_{i=1}^{Nc-1}(\Delta P^i/\Delta P^{Nc})^2/MNc$. For small M, the value of A becomes large and the magnitude of the second term in Eq. (B.14) becomes insignificant, which becomes identical to Eq. (B.8), the $m_c/m_j = 0$ case.

The discharge coefficient was previously defined as the ratio of $m_{j(actual)}$ to $m_{j,ideal}$. Then,

$$C_D = C\, m_j / [d^2 \sum_{i=1}^{Nc} (P_o \cdot \Delta P^i)^{\frac{1}{2}}] \tag{B.15}$$

The magnitudes of ΔP^i are assumed to be the same throughout the rows. Thus,

$$\frac{\omega_R}{R} = \left[\left(\frac{\omega_{m_j}}{m_j}\right)^2 + \left(2\,\frac{\omega_d}{d}\right)^2 + \left(\frac{1}{2}\,\frac{\omega_{P_o}}{P_o}\right)^2 + \left(\frac{1}{2}\,\frac{\omega_{\Delta P}}{\Delta P}\right)^2\right]^{\frac{1}{2}} \tag{B.16}$$

where $R = C_D$.

The uncertainties in the primary measurement were estimated to be $\pm$ 1% for d, $\pm$ 2% for z, $\pm$ 1 to 2% for P_o, $\pm$ 2 to 3% for ΔP, and $\pm$ 2% for m_c and m_j. Then the composite uncertainty on the flow rate ratio ($M = m_c/m_j$) is about $\pm$ 3%. The composite uncertainties in $G_j/\bar{G}_j$, G_c/G_j, and C_D were computed by substituting these into Eqs. (B.4), (B.8), (B.11), (B.14), and (B.16). The uncertainties were about $\pm$ 2% in $G_j/\bar{G}_j$ and $\pm$ 3% in C_D. The uncertainty in G_c/G_j ranged from about $\pm$ 2% for downstream rows, small M, and larger $(y_n/d)(z/d)$ to about $\pm$ 4% for upstream rows, larger M, and smaller $(y_n/d)(z/d)$.

B.2 Sensitivity Analysis on Predictive Model

The sensitivities of the simple predictive model to the experimentally determined parameter inputs were computed. The M, B and C_D, input parameters in Eqs. (4.10) and (4.11), were considered to be independent variables of $G_j/\bar{G}_j$ and G_c/G_j, and the uncertainties on M and C_D were computed to be about $\pm$ 3% by utilizing the uncertainties of the primary measurements. For computation of the uncertainty in B, the B was simplified to include only major uncertainty sources as $B = C\, m_j/[z(\Delta P)^{\frac{1}{2}}]$, and the uncertainty in B was

computed to be about ± 3%. The substitution of the closed form solutions and the uncertainties of the input parameters to Eq. (B.1) yielded the sensitivities of the predictive model.

For $G_j/\bar{G}_j$ in Eq. (4.10) replacing $G_j/\bar{G}_j$ by R, the partial derivatives of $\partial R/\partial M$ and $\partial R/\partial B$ were taken and substituted into Eq. (B.1). Then, the sensitivities in $G_j/\bar{G}_j$ becomes

$$\frac{\omega_R}{R} = \left[\left(\frac{\partial R}{\partial M}\frac{\omega_M}{R}\right)^2 + \left(\frac{\partial R}{\partial B}\frac{\omega_B}{R}\right)^2\right]^{\frac{1}{2}} \qquad \text{(B.17)}$$

Similarly for G_c/G_j in Eq. (4.11), the sensitivity in G_c/G_j (=R) becomes

$$\frac{\omega_R}{R} = \left[\left(\frac{\partial R}{\partial M}\frac{\omega_M}{R}\right)^2 + \left(\frac{\partial R}{\partial B}\frac{\omega_B}{R}\right)^2 + \left(\frac{\partial R}{\partial C_D}\frac{\omega_{C_D}}{R}\right)^2\right]^{\frac{1}{2}} \qquad \text{(B.18)}$$

The computation of these percentage sensitivites by the use of the computer covered the values at the ten spanwise rows for the parameter $(y_n/d)(z/d)$ from 4 to 24 and the flow rate ratio (M) from zero to 1. Some of the computation results of the sensitivities follow in Tables B.1 and B.2.

Table B.1 Percentage Sensitivities in $G_j/\bar{G}_j$ of Predictive Model (for C_D = 0.8)

$(y_n/d)(z/d)$	m_c/m_j	x/L	0.05	0.15	0.25	0.35	0.45	0.55	0.65	0.75	0.85	0.95
4	0.2		18.4	9.6	5.6	3.3	1.7	0.6	0.4	1.2	1.9	2.6
8	0.2		2.1	1.7	1.4	0.9	0.5	0.1	0.4	0.8	1.2	1.6
	1.0		12.2	7.0	4.0	2.1	0.8	0.2	1.0	1.6	2.1	2.6
12	0.2	$\omega_R/R(\%)$	0.9	0.8	0.6	0.4	0.2	0.0	0.2	0.4	0.7	1.0
	1.0		2.9	2.1	1.5	0.9	0.4	0.1	0.5	1.0	1.3	1.7
24	0.2		0.2	0.2	0.2	0.1	0.0	0.0	0.1	0.1	0.2	0.3
	1.0		0.6	0.5	0.3	0.2	0.1	0.0	0.2	0.3	0.4	0.6

Table B.2 Percentage Sensitivities in G_c/G_j of Predictive Model (for C_D = 0.8)

$(y_n/d)(z/d)$	m_c/m_j	x/L	0.05	0.15	0.25	0.35	0.45	0.55	0.65	0.75	0.85	0.95
4	0.2		22.4	12.2	7.4	4.9	3.7	3.2	3.1	3.0	3.0	3.0
8	0.2		6.8	5.7	5.0	4.5	4.1	3.8	3.6	3.5	3.3	3.2
	1.0		16.5	11.0	7.9	6.0	4.8	4.1	3.6	3.3	3.2	3.1
12	0.2	$\omega_R/R(\%)$	5.8	5.1	4.7	4.4	4.2	4.1	3.9	3.8	3.7	3.6
	1.0		7.6	6.7	5.9	5.3	4.8	4.4	4.0	3.8	3.6	3.4
24	0.2		5.3	4.8	4.6	4.4	4.3	4.3	4.2	4.2	4.1	4.1
	1.0		5.6	5.4	5.1	4.9	4.8	4.6	4.5	4.3	4.2	4.1

APPENDIX C

TABULAR DATA: SPECIAL DISCHARGE COEFFICIENT TESTS

Experimental results for the special discharge coefficient tests are summarized in the following Tables C.1 and C.2.

Table C.1 Results of Special Discharge Coefficient Test - Effect of G_c/G_j and z/d (These values are plotted in Fig. 4.3)

G_c/G_j	$Re_j(10^3)$	C_D	G_c/G_j	$Re_j(10^3)$	C_D
B(5,4,1)			B(5,4,3)		
0.0	11.0	0.84	0.0	10.8	0.83
0.37	10.9	0.88	0.79	10.7	0.85
0.58	11.0	0.84	0.99	10.6	0.82
0.77	11.1	0.80	1.47	10.7	0.72
0.95	11.1	0.76	1.97	8.1	0.64
1.15	11.2	0.71	3.08	5.2	0.53
1.33	11.3	0.68	4.03	4.0	0.46
1.52	11.4	0.65			
1.94	11.1	0.58	B(5,8,1)		
2.45	10.7	0.53	0.0	10.8	0.79
2.75	10.7	0.50	0.19	10.8	0.82
3.56	8.3	0.44	0.39	10.8	0.82
3.91	7.5	0.41	0.60	10.7	0.79
4.77	6.2	0.37	0.79	10.5	0.76
5.93	5.0	0.32	1.02	10.4	0.72
7.83	3.8	0.27	1.31	10.6	0.67
B(5,4,2)			1.50	10.5	0.64
0.79	10.7	0.83	1.95	10.6	0.57
0.99	10.7	0.80	2.87	10.9	0.47
2.0	10.7	0.63	3.80	10.8	0.40
3.9	6.1	0.46			

Table C.2 Results of Special Discharge Coefficient Test with Jet Plate B(5,4,1) - Effect of Re_j
(These values are plotted in Fig. 4.4)

$G_c/G_j \approx 0$		$G_c/G_j \simeq 1$		$G_c/G_j \simeq 3$	
$Re_j(10^3)$	C_D	$Re_j(10^3)$	C_D	$Re_j(10^3)$	C_D
1.8	0.82	2.1	0.85	2.1	0.50
2.2	0.79	2.6	0.82	3.2	0.50
3.5	0.83	3.4	0.83	4.3	0.50
4.6	0.85	4.2	0.82	6.4	0.50
6.3	0.84	6.4	0.79	8.3	0.48
8.2	0.84	8.5	0.77	10.5	0.49
10.5	0.84	12.8	0.75	12.7	0.48
15.1	0.83	15.2	0.75		
19.6	0.81	17.4	0.75		
22.5	0.80	19.9	0.75		
		20.9	0.75		
		22.1	0.75		
		30.1	0.75		
		42.0	0.76		
		44.6	0.77		

APPENDIX D

TABULAR DATA: INITIAL CROSSFLOW TESTS

The following is a presentation in tabular form of the experimental results for the initial crossflow tests. The flow distribution and pressure profile data are given in Table D.1 (pp. 137-148). The heat transfer data, η and Nu profiles, are given in Table D.2 (pp. 149-161). The notations used in the tables of Appendices D and E have the meanings specified below.

Notation used in the Appendix	Corresponding Nomenclature or Meaning
ETA	η
GJ/$\overline{\text{GJ}}$	$G_j/\overline{G}_j$
GC/GJ	G_c/G_j
MC/MJ	m_c/m_j
M.C.	Mass Closure
NU, $\overline{\text{NU}}$†	Nu, $\overline{\text{Nu}}$
PO	P_o
P/PO	P/P_o
$\overline{\text{REJ}}$(K)	$\overline{\text{Re}}_j(10^3)$
$\overline{\text{REJ1}}$(K)	$\overline{\text{Re}}_{j,1}(10^3)$
$\overline{\text{REJ2}}$(K)	$\overline{\text{Re}}_{j,2}(10^3)$
ST, $\overline{\text{ST}}$†	St, $\overline{\text{St}}$
TO	T_o
X/L	x/L

†Mean values of Nusselt number and Stanton number listed are the mean values over the heat transfer surface opposite the jet array ($0 \leq x/L \leq 1$).

TABLE D.1 FLOW DISTRIBUTIONS AND PRESSURE PROFILES
(pp. 138 - 148)

B(5,4,1)I

MC/MJ	$\overline{REJ}$(K)	X/L	0.05	0.15	0.25	0.35	0.45	0.55	0.65	0.75	0.85	0.95	T0 (K)	P0 (KPA)	M.C.
		P/P0	0.99	0.99	0.99	0.99	0.98	0.98	0.96	0.95	0.91	0.87			
0.0	10.4	GJ/$\overline{GJ}$	0.49	0.51	0.55	0.64	0.77	0.93	1.12	1.36	1.64	1.98	306.	118.	1.00
		GC/GJ	0.0	0.19	0.36	0.47	0.56	0.62	0.68	0.72	0.76	0.79			
		P/P0	1.00	1.00	0.99	0.99	0.98	0.97	0.96	0.93	0.90	0.83			
0.20	10.6	GJ/$\overline{GJ}$	0.14	0.26	0.41	0.57	0.75	0.97	1.23	1.52	1.87	2.28	304.	126.	0.99
		GC/GJ	2.71	1.60	1.15	0.96	0.88	0.83	0.81	0.81	0.82	0.84			
		P/P0	1.00	1.00	1.00	0.99	0.99	0.98	0.96	0.93	0.88	0.80			
0.51	10.2	GJ/$\overline{GJ}$	0.02	0.06	0.15	0.31	0.58	0.93	1.29	1.72	2.19	2.74	306.	138.	0.97
		GC/GJ	51.38	16.43	6.83	3.44	1.96	1.36	1.11	0.98	0.93	0.90			
		P/P0	1.00	1.00	1.00	1.00	0.99	0.98	0.96	0.92	0.87	0.76			
0.99	10.5	GJ/$\overline{GJ}$	0.0	0.02	0.07	0.16	0.35	0.71	1.22	1.83	2.46	3.19	305.	166.	0.99
		GC/GJ	******	124.62	29.41	12.12	5.66	2.93	1.81	1.33	1.14	1.03			

B(5,4,2)1

MC/MJ	$\overline{REJ}$(K)	X/L	0.05	0.15	0.25	0.35	0.45	0.55	0.65	0.75	0.85	0.95	T0 (K)	P0 (KPA)	M.C.
		P/P0	0.98	0.98	0.97	0.97	0.97	0.97	0.96	0.95	0.95	0.93			
0.0	10.7	GJ/$\overline{GJ}$	0.81	0.82	0.87	0.86	0.90	0.97	1.05	1.14	1.24	1.35	307.	106.	0.98
		GC/GJ	0.0	0.10	0.18	0.29	0.37	0.43	0.49	0.54	0.59	0.63			
		P/P0	0.98	0.98	0.98	0.98	0.97	0.97	0.96	0.95	0.94	0.92			
0.18	10.9	GJ/$\overline{GJ}$	0.68	0.72	0.78	0.84	0.91	0.99	1.09	1.20	1.32	1.46	306.	107.	0.98
		GC/GJ	0.27	0.35	0.41	0.47	0.53	0.57	0.61	0.64	0.67	0.70			
		P/P0	0.99	0.99	0.98	0.98	0.97	0.96	0.95	0.94	0.93	0.91			
0.49	10.8	GJ/$\overline{GJ}$	0.54	0.62	0.71	0.80	0.90	1.01	1.13	1.27	1.42	1.59	307.	109.	1.01
		GC/GJ	0.89	0.84	0.83	0.82	0.82	0.81	0.81	0.81	0.81	0.82			
		P/P0	0.99	0.99	0.99	0.98	0.97	0.96	0.95	0.93	0.90	0.87			
1.01	10.2	GJ/$\overline{GJ}$	0.21	0.34	0.49	0.66	0.84	1.05	1.25	1.47	1.70	1.98	313.	114.	0.98
		GC/GJ	4.73	3.04	2.16	1.67	1.40	1.20	1.09	1.00	0.95	0.91			

B(5,4,3)I

MC/MJ	$\overline{REJ}$(K)	X/L	0.05	0.15	0.25	0.35	0.45	0.55	0.65	0.75	0.85	0.95	T0 (K)	P0 (KPA)	M.C.
		P/P0	0.97	0.97	0.97	0.97	0.97	0.97	0.96	0.96	0.96	0.95			
0.0	10.5	GJ/$\overline{GJ}$	0.91	0.92	0.93	0.96	0.96	0.98	1.02	1.05	1.10	1.16	306.	103.	0.97
		GC/GJ	0.0	0.06	0.13	0.19	0.25	0.31	0.37	0.42	0.46	0.50			
		P/P0	0.98	0.98	0.97	0.97	0.97	0.97	0.96	0.96	0.96	0.95			
0.19	10.5	GJ/$\overline{GJ}$	0.87	0.88	0.89	0.91	0.95	0.99	1.04	1.09	1.16	1.22	307.	103.	0.95
		GC/GJ	0.15	0.21	0.28	0.33	0.38	0.43	0.47	0.51	0.54	0.58			
		P/P0	0.98	0.98	0.98	0.97	0.97	0.97	0.96	0.96	0.95	0.94			
0.49	10.5	GJ/$\overline{GJ}$	0.77	0.81	0.85	0.90	0.95	1.00	1.07	1.14	1.21	1.30	309.	104.	0.95
		GC/GJ	0.44	0.48	0.52	0.55	0.58	0.62	0.64	0.66	0.68	0.70			
		P/P0	0.99	0.98	0.98	0.97	0.97	0.96	0.96	0.95	0.94	0.93			
0.99	10.6	GJ/$\overline{GJ}$	0.62	0.70	0.78	0.86	0.94	1.03	1.11	1.21	1.32	1.43	307.	106.	0.99
		GC/GJ	1.05	0.99	0.95	0.92	0.90	0.88	0.88	0.86	0.86	0.85			

B(5,8,1)I

MC/MJ	$\overline{REJ}$(K)	X/L	0.05	0.15	0.25	0.35	0.45	0.55	0.65	0.75	0.85	0.95	TO (K)	PO (KPA)	M.C.
		P/PO	0.98	0.98	0.98	0.98	0.97	0.97	0.96	0.96	0.95	0.93			
0.0	10.4	GJ/$\overline{GJ}$	0.79	0.80	0.82	0.86	0.91	0.97	1.05	1.15	1.26	1.38	303.	105.	0.94
		GC/GJ	0.0	0.10	0.19	0.28	0.35	0.42	0.48	0.53	0.57	0.61			
		P/PO	0.99	0.99	0.98	0.98	0.98	0.97	0.96	0.95	0.94	0.92			
0.20	10.2	GJ/$\overline{GJ}$	0.67	0.71	0.77	0.83	0.90	0.98	1.08	1.19	1.36	1.53	303.	106.	0.93
		GC/GJ	0.32	0.39	0.45	0.51	0.56	0.60	0.64	0.67	0.67	0.68			
		P/PO	0.99	0.99	0.99	0.98	0.98	0.97	0.96	0.95	0.93	0.90			
0.52	9.8	GJ/$\overline{GJ}$	0.48	0.59	0.65	0.75	0.86	0.98	1.13	1.30	1.49	1.78	303.	108.	0.91
		GC/GJ	1.18	1.03	1.02	0.97	0.93	0.90	0.87	0.84	0.82	0.77			
		P/PO	0.99	0.99	0.99	0.98	0.97	0.96	0.95	0.93	0.90	0.85			
0.99	10.4	GJ/$\overline{GJ}$	0.26	0.38	0.47	0.65	0.83	1.01	1.22	1.44	1.72	2.03	303.	116.	0.94
		GC/GJ	4.00	2.78	2.35	1.77	1.46	1.27	1.14	1.04	0.96	0.89			

B(5,8,2)I

MC/MJ	$\overline{REJ}$(K)	X/L	0.05	0.15	0.25	0.35	0.45	0.55	0.65	0.75	0.85	0.95	T0 (K)	P0 (KPA)	M.C.
		P/P0	0.96	0.96	0.96	0.96	0.96	0.96	0.96	0.96	0.96	0.95			
0.0	10.5	GJ/$\overline{GJ}$	0.95	0.95	0.96	0.96	0.98	0.99	1.01	1.04	1.07	1.10	304.	102.	0.98
		GC/GJ	0.0	0.05	0.10	0.15	0.19	0.24	0.28	0.32	0.36	0.40			
		P/P0	0.97	0.97	0.97	0.97	0.96	0.96	0.96	0.96	0.96	0.95			
0.20	10.3	GJ/$\overline{GJ}$	0.93	0.92	0.93	0.95	0.97	1.00	1.03	1.06	1.09	1.13	306.	102.	0.97
		GC/GJ	0.11	0.16	0.21	0.25	0.29	0.33	0.37	0.41	0.44	0.48			
		P/P0	0.97	0.97	0.97	0.97	0.97	0.96	0.96	0.96	0.95	0.95			
0.50	10.0	GJ/$\overline{GJ}$	0.86	0.88	0.91	0.94	0.95	1.00	1.04	1.09	1.14	1.19	306.	100.	0.97
		GC/GJ	0.30	0.34	0.37	0.41	0.46	0.48	0.50	0.53	0.56	0.58			
		P/P0	0.98	0.98	0.97	0.97	0.97	0.96	0.96	0.95	0.95	0.94			
1.04	10.1	GJ/$\overline{GJ}$	0.78	0.82	0.86	0.90	0.96	1.01	1.07	1.13	1.20	1.26	307.	103.	0.98
		GC/GJ	0.66	0.68	0.69	0.71	0.71	0.72	0.73	0.74	0.74	0.75			

B(5,8,3)I

MC/MJ	$\overline{REJ}$(K)	X/L	0.05	0.15	0.25	0.35	0.45	0.55	0.65	0.75	0.85	0.95	T0 (K)	P0 (KPA)	M.C.
		P/P0	0.96	0.96	0.96	0.96	0.96	0.96	0.96	0.96	0.96	0.96			
0.0	10.5	GJ/$\overline{GJ}$	0.97	0.98	0.98	0.99	1.00	1.00	1.01	1.01	1.02	1.03	300.	102.	0.99
		GC/GJ	0.0	0.03	0.06	0.10	0.13	0.16	0.19	0.22	0.25	0.28			
		P/P0	0.96	0.96	0.96	0.96	0.96	0.96	0.96	0.96	0.96	0.96			
0.21	10.4	GJ/$\overline{GJ}$	0.96	0.98	0.98	0.98	0.98	0.99	1.01	1.02	1.04	1.05	302.	102.	0.99
		GC/GJ	0.07	0.10	0.14	0.17	0.20	0.23	0.26	0.29	0.32	0.35			
		P/P0	0.97	0.97	0.97	0.96	0.96	0.96	0.96	0.96	0.96	0.96			
0.50	10.4	GJ/$\overline{GJ}$	0.95	0.95	0.96	0.98	0.99	1.00	1.02	1.04	1.05	1.07	303.	101.	0.96
		GC/GJ	0.18	0.21	0.24	0.27	0.30	0.33	0.36	0.38	0.41	0.43			
		P/P0	0.97	0.97	0.97	0.97	0.97	0.97	0.96	0.96	0.96	0.96			
1.00	10.3	GJ/$\overline{GJ}$	0.90	0.92	0.94	0.96	0.98	1.00	1.03	1.06	1.09	1.12	303.	102.	0.93
		GC/GJ	0.39	0.42	0.44	0.46	0.48	0.50	0.53	0.54	0.56	0.57			

B(10,4,1)I

MC/MJ	$\overline{REJ}$(K)	X/L	0.05	0.15	0.25	0.35	0.45	0.55	0.65	0.75	0.85	0.95	T0 (K)	P0 (KPA)	M.C.
		P/P0	0.98	0.98	0.98	0.98	0.97	0.96	0.94	0.90	0.84	0.72			
0.0	11.2	GJ/$\overline{GJ}$	0.56	0.58	0.63	0.67	0.77	0.90	1.08	1.30	1.58	1.92	308.	207.	0.98
		GC/GJ	0.0	0.19	0.36	0.52	0.62	0.70	0.75	0.78	0.81	0.82			
		P/P0	1.00	1.00	1.00	0.99	0.98	0.97	0.95	0.92	0.86	0.76			
0.49	10.3	GJ/$\overline{GJ}$	0.02	0.11	0.25	0.44	0.69	0.96	1.27	1.61	2.08	2.57	307.	272.	0.98
		GC/GJ	53.79	9.16	4.11	2.41	1.66	1.34	1.16	1.07	0.98	0.95			

B(10,4,3)I

MC/MJ	$\overline{REJ}$(K)	X/L	0.05	0.15	0.25	0.35	0.45	0.55	0.65	0.75	0.85	0.95	T0 (K)	P0 (KPA)	M.C.
		P/P0	0.88	0.88	0.88	0.87	0.87	0.86	0.86	0.85	0.83	0.82			
0.0	10.6	GJ/$\overline{GJ}$	0.93	0.94	0.95	0.96	0.97	1.00	1.01	1.04	1.08	1.11	303.	121.	0.97
		GC/GJ	0.0	0.06	0.13	0.19	0.26	0.31	0.37	0.43	0.47	0.52			
		P/P0	0.90	0.90	0.89	0.89	0.88	0.87	0.86	0.85	0.83	0.81			
0.20	10.5	GJ/$\overline{GJ}$	0.89	0.90	0.92	0.94	0.96	0.99	1.03	1.07	1.12	1.16	305.	122.	0.95
		GC/GJ	0.15	0.21	0.27	0.33	0.39	0.44	0.49	0.53	0.57	0.61			
		P/P0	0.93	0.92	0.91	0.90	0.89	0.88	0.87	0.85	0.83	0.80			
0.51	10.5	GJ/$\overline{GJ}$	0.80	0.84	0.88	0.92	0.96	1.01	1.06	1.11	1.17	1.24	304.	125.	0.94
		GC/GJ	0.44	0.49	0.53	0.57	0.60	0.64	0.67	0.70	0.73	0.75			
		P/P0	0.95	0.94	0.93	0.91	0.90	0.88	0.86	0.83	0.80	0.76			
1.00	10.4	GJ/$\overline{GJ}$	0.71	0.76	0.82	0.88	0.95	1.02	1.09	1.17	1.25	1.34	307.	134.	0.98
		GC/GJ	0.94	0.93	0.92	0.92	0.92	0.92	0.92	0.92	0.92	0.92			

B(10,8,1)I

MC/MJ	$\overline{REJ}$(K)	X/L	0.05	0.15	0.25	0.35	0.45	0.55	0.65	0.75	0.85	0.95	T0 (K)	P0 (KPA)	M.C.
		P/P0	0.93	0.93	0.92	0.92	0.91	0.90	0.88	0.86	0.82	0.78			
0.0	10.4	GJ/$\overline{GJ}$	0.84	0.84	0.86	0.88	0.93	0.98	1.05	1.12	1.21	1.30	303.	133.	0.98
		GC/GJ	0.0	0.10	0.19	0.28	0.36	0.43	0.50	0.56	0.61	0.66			
		P/P0	0.96	0.95	0.95	0.94	0.93	0.91	0.89	0.86	0.83	0.77			
0.23	9.8	GJ/$\overline{GJ}$	0.71	0.74	0.79	0.85	0.92	0.99	1.08	1.19	1.30	1.42	303.	136.	0.96
		GC/GJ	0.33	0.41	0.47	0.53	0.58	0.63	0.67	0.70	0.73	0.76			
		P/P0	0.97	0.97	0.96	0.95	0.93	0.91	0.89	0.85	0.81	0.74			
0.46	10.2	GJ/$\overline{GJ}$	0.58	0.65	0.73	0.81	0.91	1.01	1.12	1.26	1.40	1.54	302.	148.	0.96
		GC/GJ	0.80	0.81	0.81	0.82	0.82	0.83	0.83	0.83	0.83	0.85			
		P/P0	0.99	0.98	0.97	0.96	0.94	0.92	0.89	0.85	0.79	0.70			
1.01	10.1	GJ/$\overline{GJ}$	0.26	0.40	0.56	0.73	0.89	1.06	1.23	1.43	1.63	1.81	302.	176.	0.99
		GC/GJ	3.86	2.55	1.88	1.52	1.33	1.20	1.12	1.05	1.01	0.99			

B(10,8,2)I

MC/MJ	$\overline{REJ}$(K)	X/L	0.05	0.15	0.25	0.35	0.45	0.55	0.65	0.75	0.85	0.95	T0 (K)	P0 (KPA)	M.C.
		P/P0	0.87	0.87	0.87	0.86	0.86	0.86	0.85	0.85	0.84	0.82			
0.0	10.2	GJ/$\overline{GJ}$	0.96	0.96	0.97	0.98	0.98	0.99	1.01	1.03	1.05	1.08	303.	119.	1.00
		GC/GJ	0.0	0.05	0.10	0.14	0.19	0.24	0.28	0.33	0.37	0.41			
		P/P0	0.89	0.88	0.88	0.88	0.87	0.87	0.86	0.85	0.84	0.82			
0.19	10.0	GJ/$\overline{GJ}$	0.93	0.94	0.95	0.96	0.98	0.99	1.02	1.05	1.08	1.11	304.	119.	0.99
		GC/GJ	0.10	0.15	0.19	0.24	0.28	0.33	0.37	0.41	0.44	0.48			
		P/P0	0.90	0.90	0.89	0.89	0.88	0.87	0.86	0.85	0.83	0.81			
0.50	10.1	GJ/$\overline{GJ}$	0.89	0.91	0.92	0.95	0.97	1.00	1.03	1.07	1.11	1.16	307.	121.	0.98
		GC/GJ	0.28	0.33	0.37	0.41	0.45	0.48	0.51	0.54	0.57	0.59			
		P/P0	0.93	0.93	0.92	0.91	0.90	0.89	0.87	0.86	0.83	0.80			
1.07	9.5	GJ/$\overline{GJ}$	0.80	0.84	0.87	0.91	0.96	1.00	1.06	1.12	1.18	1.26	307.	122.	0.97
		GC/GJ	0.68	0.69	0.71	0.73	0.74	0.75	0.76	0.77	0.77	0.77			

B(10,8,3)I

MC/MJ	$\overline{REJ}$(K)	X/L	0.05	0.15	0.25	0.35	0.45	0.55	0.65	0.75	0.85	0.95	T0 (K)	P0 (KPA)	M.C.
		P/P0	0.85	0.85	0.85	0.85	0.84	0.84	0.84	0.84	0.83	0.83			
0.0	10.4	GJ/$\overline{GJ}$	0.98	0.98	0.99	0.99	0.99	1.00	1.01	1.01	1.02	1.03	301.	118.	1.02
		GC/GJ	0.0	0.03	0.07	0.10	0.13	0.16	0.19	0.22	0.26	0.28			
		P/P0	0.86	0.86	0.86	0.85	0.85	0.85	0.85	0.84	0.84	0.83			
0.22	10.2	GJ/$\overline{GJ}$	0.97	0.97	0.98	0.98	0.99	1.00	1.01	1.02	1.03	1.04	303.	117.	1.01
		GC/GJ	0.07	0.10	0.14	0.17	0.20	0.23	0.26	0.29	0.32	0.35			
		P/P0	0.87	0.87	0.87	0.86	0.86	0.86	0.85	0.84	0.84	0.83			
0.51	10.2	GJ/$\overline{GJ}$	0.95	0.96	0.97	0.98	0.99	1.00	1.02	1.03	1.04	1.06	303.	117.	0.99
		GC/GJ	0.18	0.21	0.24	0.27	0.30	0.33	0.35	0.38	0.41	0.43			
		P/P0	0.89	0.89	0.88	0.88	0.87	0.87	0.86	0.85	0.84	0.83			
1.04	10.2	GJ/$\overline{GJ}$	0.92	0.94	0.95	0.97	0.98	1.00	1.03	1.05	1.07	1.10	303.	118.	0.97
		GC/GJ	0.38	0.41	0.43	0.46	0.48	0.50	0.52	0.54	0.57	0.59			

TABLE D.2 HEAT TRANSFER DATA (pp. 150 - 161)

B(5,4,1)I

$\overline{REJ}$(K) MC/MJ	$\overline{NU}$	X/L	-0.25	-0.15	-0.05	0.05	0.15	0.25	0.35	0.45	0.55	0.65	0.75	0.85	0.95	1.05
10.3	42.4	NU	**********			35.1	31.3	31.0	32.4	34.4	38.5	42.9	51.2	59.4	67.7	70.5
0.0		ETA	**********													
10.4	39.6	NU	12.3	11.8	12.3	12.1	15.3	21.3	27.8	33.4	40.2	46.9	56.5	66.1	76.0	78.9
0.19		ETA	1.00	1.00	1.00	0.89	0.81	0.49	0.34	0.25	0.20	0.18	0.13	0.09	0.07	0.03
10.0	42.1	NU	25.9	24.9	24.7	23.8	23.7	23.2	23.7	26.9	37.5	47.1	60.0	72.7	82.4	89.2
0.50		ETA	1.00	1.00	1.00	0.97	0.95	0.94	0.94	0.88	0.64	0.42	0.26	0.17	0.09	0.05
10.2	52.5	NU	42.9	40.9	40.2	40.4	39.4	38.9	37.2	38.1	41.4	48.9	65.2	82.7	92.9	105.1
1.01		ETA	1.00	1.00	1.00	0.96	0.94	0.94	0.94	0.91	0.89	0.79	0.55	0.31	0.10	-0.01

B(5,4,2)I

$\overline{REJ(K)}$ MC/MJ	$\overline{NU}$	X/L	-0.25	-0.15	-0.05	0.05	0.15	0.25	0.35	0.45	0.55	0.65	0.75	0.85	0.95	1.05
9.7	40.8	NU	**********			45.2	42.8	40.4	37.8	37.5	37.8	38.3	40.7	43.4	44.6	45.8
0.0		ETA	**********													
10.6	40.6	NU	7.6	7.2	7.1	29.7	38.9	39.1	38.0	38.2	39.7	40.9	44.6	47.1	49.5	52.2
0.19		ETA	1.00	1.00	1.00	0.43	0.34	0.29	0.24	0.19	0.16	0.13	0.12	0.08	0.07	0.05
9.5	29.9	NU	15.2	14.8	14.8	14.9	15.9	20.8	25.5	28.4	31.6	34.5	38.2	43.1	45.8	49.5
0.56		ETA	1.00	1.00	1.00	1.02	1.00	0.84	0.70	0.56	0.48	0.42	0.35	0.30	0.25	0.23
10.2	33.4	NU	24.1	23.2	23.1	23.0	23.1	24.0	25.1	27.9	32.8	36.4	41.7	48.0	51.8	57.0
0.97		ETA	1.00	1.00	1.00	0.98	0.93	0.92	0.91	0.84	0.73	0.61	0.47	0.35	0.24	0.18

B(5,4,3)I

$\overline{REJ}$(K) MC/MJ	$\overline{NU}$	X/L	-0.25	-0.15	-0.05	0.05	0.15	0.25	0.35	0.45	0.55	0.65	0.75	0.85	0.95	1.05
10.5	42.0	NU	**********			50.3	47.9	47.8	43.7	39.7	38.3	37.0	37.5	39.5	38.7	39.5
0.0		ETA	**********													
10.3	37.4	NU	6.0	5.9	4.8	36.4	40.9	39.8	36.7	35.2	35.4	35.9	37.1	38.9	38.1	39.3
0.20		ETA	1.00	1.00	1.00	0.50	0.40	0.37	0.32	0.28	0.25	0.23	0.20	0.17	0.15	0.15
9.8	29.4	NU	10.3	9.7	9.7	11.0	21.6	31.3	32.2	31.4	31.2	31.6	33.0	35.1	35.0	35.9
0.47		ETA	1.00	1.00	1.00	1.00	0.81	0.56	0.53	0.49	0.46	0.42	0.38	0.34	0.31	0.29
10.3	25.2	NU	18.0	17.3	17.2	17.8	17.3	18.3	20.5	23.4	26.0	28.3	30.7	34.4	35.1	38.3
1.00		ETA	1.00	1.00	1.00	0.98	0.96	0.95	0.92	0.85	0.79	0.71	0.64	0.58	0.52	0.48

B(5,8,1)I

$\overline{REJ}$(K) MC/MJ	$\overline{NU}$	X/L	-0.25	-0.15	-0.05	0.05	0.15	0.25	0.35	0.45	0.55	0.65	0.75	0.85	0.95	1.05
10.3	36.0	NU	**********			37.8	36.8	34.6	32.5	32.4	33.4	34.4	36.3	40.2	41.3	32.8
0.0		ETA	**********													
10.0	34.4	NU	7.9	8.1	7.1	22.6	28.0	29.4	30.8	32.1	34.2	36.7	39.4	44.5	46.1	40.2
0.20		ETA	1.00	1.00	1.00	0.46	0.37	0.31	0.28	0.25	0.22	0.19	0.17	0.14	0.13	0.14
10.3	36.3	NU	14.5	14.1	13.7	16.4	26.1	28.6	31.5	33.8	37.1	40.9	44.5	50.6	53.0	49.1
0.49		ETA	1.00	1.00	1.00	0.97	0.66	0.50	0.44	0.37	0.34	0.31	0.26	0.22	0.21	0.22
10.1	38.9	NU	23.3	22.6	23.2	23.4	24.4	26.9	31.3	34.9	39.4	43.5	49.1	56.7	59.8	57.8
0.97		ETA	1.00	1.00	1.00	0.98	0.98	0.90	0.76	0.63	0.53	0.45	0.37	0.31	0.26	0.27

B(5,8,2)I

$\overline{REJ(K)}$ MC/MJ	$\overline{NU}$	X/L	-0.25	-0.15	-0.05	0.05	0.15	0.25	0.35	0.45	0.55	0.65	0.75	0.85	0.95	1.05
10.4	39.6	NU	**********			42.0	42.8	42.3	40.4	39.1	37.8	37.4	37.3	38.9	37.7	29.2
0.0		ETA	**********													
10.2	38.8	NU	5.7	5.5	7.0	43.1	41.6	40.3	38.2	36.8	36.7	36.6	37.2	39.6	38.1	32.8
0.19		ETA	1.00	1.00	1.00	0.33	0.29	0.22	0.20	0.17	0.15	0.15	0.14	0.12	0.11	0.12
10.0	35.3	NU	9.0	8.7	8.2	26.0	34.7	35.1	35.3	35.3	35.2	35.9	36.9	39.8	39.1	36.0
0.50		ETA	1.00	1.00	1.00	0.60	0.44	0.43	0.43	0.41	0.35	0.34	0.32	0.29	0.27	0.26
9.9	31.6	NU	14.9	14.4	14.3	15.5	24.3	29.8	31.4	31.8	33.4	34.5	36.1	39.2	39.7	38.9
1.02		ETA	1.00	1.00	1.00	0.99	0.77	0.58	0.54	0.50	0.48	0.46	0.44	0.41	0.38	0.37

B(5,8,3)I

$\overline{REJ}$(K)	$\overline{NU}$	X/L	-0.25	-0.15	-0.05	0.05	0.15	0.25	0.35	0.45	0.55	0.65	0.75	0.85	0.95	1.05
MC/MJ																
10.3	40.2	NU	**********			42.3	42.3	42.7	41.4	40.6	39.3	39.2	38.0	39.1	37.3	26.6
0.0		ETA	**********													
10.2	40.0	NU	5.0	4.6	11.9	46.2	43.3	42.9	39.8	39.3	37.8	37.3	37.4	38.5	37.2	30.0
0.20		ETA	1.00	1.00	1.00	0.38	0.29	0.22	0.21	0.18	0.17	0.15	0.15	0.13	0.13	0.16
10.2	37.1	NU	7.1	6.7	5.7	35.0	38.2	38.5	37.8	36.1	36.4	36.5	37.0	38.5	37.1	33.9
0.50		ETA	1.00	1.00	1.00	0.57	0.47	0.44	0.41	0.38	0.36	0.33	0.31	0.28	0.27	0.29
9.8	30.9	NU	10.8	10.3	10.5	13.4	28.4	31.5	32.2	32.1	32.8	32.6	34.1	35.7	36.1	35.8
1.02		ETA	1.00	1.00	1.00	0.89	0.61	0.52	0.52	0.51	0.51	0.48	0.43	0.39	0.39	0.38

B(10,4,2)I

$\overline{REJ}$(K)	$\overline{NU}$	X/L	-0.25	-0.15	-0.05	0.05	0.15	0.25	0.35	0.45	0.55	0.65	0.75	0.85	0.95	1.05
MC/MJ																
10.1	32.9	NU	**********			38.0	35.3	34.7	31.9	30.4	29.9	29.7	31.6	33.5	34.0	32.8
0.0		ETA	**********													
9.8	31.5	NU	7.0	7.0	6.2	27.8	31.4	30.6	30.1	30.1	30.8	31.2	32.8	34.7	35.7	36.6
0.20		ETA	1.00	1.00	1.00	0.53	0.46	0.40	0.33	0.26	0.23	0.20	0.16	0.12	0.10	0.08
9.9	28.2	NU	13.0	12.8	13.3	14.5	22.0	25.4	26.5	27.1	28.9	30.5	32.9	36.3	37.5	40.6
0.50		ETA	1.00	1.00	1.00	0.98	0.81	0.61	0.54	0.47	0.42	0.37	0.32	0.26	0.20	0.15
9.8	29.9	NU	20.9	20.3	21.4	20.7	21.8	23.1	25.2	27.1	30.2	32.5	35.9	40.4	41.9	46.9
0.98		ETA	1.00	1.00	1.00	0.94	0.93	0.91	0.87	0.78	0.69	0.60	0.51	0.42	0.31	0.23

B(10,4,3)I

$\overline{REJ}$(K)	$\overline{NU}$	X/L	-0.25	-0.15	-0.05	0.05	0.15	0.25	0.35	0.45	0.55	0.65	0.75	0.85	0.95	1.05
MC/MJ																
10.6	30.4	NU	**********			40.3	37.5	35.7	32.6	29.9	27.6	25.2	25.0	25.8	24.6	23.8
0.0		ETA	**********													
10.4	27.5	NU	4.7	4.7	4.1	31.7	34.4	31.3	27.9	25.8	25.0	24.3	24.6	25.4	24.6	24.6
0.19		ETA	1.00	1.00	1.00	0.51	0.42	0.34	0.29	0.25	0.22	0.21	0.19	0.15	0.14	0.12
10.1	22.7	NU	9.2	8.8	8.7	14.3	24.9	25.2	24.1	23.2	23.1	22.7	22.8	23.7	23.3	24.2
0.51		ETA	1.00	1.00	1.00	0.88	0.70	0.61	0.56	0.49	0.45	0.41	0.38	0.35	0.32	0.29
10.2	20.8	NU	15.1	14.4	14.7	14.8	15.6	18.9	20.6	20.9	21.6	22.1	23.3	25.3	25.2	27.2
0.99		ETA	1.00	1.00	1.00	0.98	0.96	0.87	0.79	0.71	0.66	0.62	0.57	0.53	0.48	0.45

B(10,8,1)I

$\overline{REJ}$(K)	$\overline{NU}$	X/L	-0.25	-0.15	-0.05	0.05	0.15	0.25	0.35	0.45	0.55	0.65	0.75	0.85	0.95	1.05
MC/MJ																
10.3	25.6	NU	**********			27.4	25.0	25.0	23.9	22.8	23.2	23.7	26.3	28.6	29.7	23.8
0.0		ETA	**********													
10.1	25.5	NU	6.4	6.7	6.0	18.3	21.4	22.3	23.0	23.8	25.2	26.8	28.9	32.4	33.4	28.9
0.20		ETA	1.00	1.00	1.00	0.48	0.40	0.31	0.26	0.21	0.18	0.16	0.15	0.10	0.08	0.08
10.1	28.5	NU	11.9	11.9	12.2	16.2	21.6	24.2	26.6	27.6	29.3	30.9	33.1	37.6	38.0	34.8
0.50		ETA	1.00	1.00	1.00	0.89	0.67	0.54	0.48	0.40	0.35	0.31	0.27	0.21	0.17	0.16
10.0	33.1	NU	20.0	20.0	22.2	22.4	23.0	25.5	28.7	31.3	33.8	36.1	39.2	44.9	46.0	44.1
0.99		ETA	1.00	1.00	1.00	0.97	0.96	0.88	0.76	0.65	0.55	0.48	0.42	0.35	0.29	0.28

B(10,8,2)I

$\overline{REJ}$(K)	$\overline{NU}$	X/L	-0.25	-0.15	-0.05	0.05	0.15	0.25	0.35	0.45	0.55	0.65	0.75	0.85	0.95	1.05
MC/MJ																
10.3	28.1	NU	**********			31.5	30.9	30.9	29.8	27.8	26.9	25.7	25.3	26.7	25.8	17.1
0.0		ETA	**********													
10.0	27.6	NU	4.0	4.0	3.3	30.3	31.8	30.1	28.4	26.4	25.4	24.9	25.1	26.9	26.2	20.1
0.19		ETA	1.00	1.00	1.00	0.40	0.31	0.25	0.22	0.19	0.16	0.16	0.14	0.11	0.10	0.12
10.0	26.3	NU	7.0	7.1	6.6	22.8	27.1	27.4	26.6	25.6	25.8	25.8	26.0	28.1	27.4	24.1
0.50		ETA	1.00	1.00	1.00	0.60	0.51	0.48	0.45	0.41	0.37	0.33	0.29	0.25	0.23	0.24
9.9	24.6	NU	11.7	11.4	11.6	14.6	22.1	24.1	24.5	24.6	25.5	26.0	26.8	29.0	28.6	28.2
1.01		ETA	1.00	1.00	1.00	0.93	0.72	0.63	0.59	0.55	0.50	0.47	0.42	0.38	0.33	0.32

B(10,8,3)I

$\overline{REJ}$(K)	$\overline{NU}$	X/L	-0.25	-0.15	-0.05	0.05	0.15	0.25	0.35	0.45	0.55	0.65	0.75	0.85	0.95	1.05
MC/MJ																
10.4	28.6	NU	**********			31.9	31.2	31.3	30.7	29.1	27.9	26.5	25.6	26.5	25.4	14.9
0.0		ETA	**********													
10.0	28.2	NU	3.0	3.0	2.5	32.6	33.2	31.7	29.7	27.3	26.2	25.0	24.8	26.0	25.1	17.3
0.21		ETA	1.00	1.00	1.00	0.46	0.31	0.26	0.23	0.22	0.20	0.17	0.15	0.13	0.13	0.14
10.0	26.4	NU	5.5	5.4	4.9	25.9	28.9	29.3	27.1	26.0	25.6	24.8	24.8	26.4	25.3	20.6
0.51		ETA	1.00	1.00	1.00	0.61	0.55	0.48	0.45	0.41	0.37	0.35	0.31	0.28	0.26	0.28
10.1	24.4	NU	8.9	8.7	8.8	16.0	25.2	26.0	25.4	24.7	24.7	24.6	25.0	26.7	25.7	24.8
1.00		ETA	1.00	1.00	1.00	0.83	0.68	0.64	0.64	0.58	0.53	0.50	0.46	0.42	0.39	0.38

B(5,4,3)S

$\overline{REJ}$(K)	$\overline{NU}$	X/L	-0.25	-0.15	-0.05	0.05	0.15	0.25	0.35	0.45	0.55	0.65	0.75	0.85	0.95	1.05
MC/MJ																
10.5	36.2	NU	**********			49.6	46.5	45.1	41.4	35.2	31.8	30.2	28.9	27.5	26.0	25.4
0.0		ETA	**********													
10.2	29.0	NU	5.8	5.7	4.7	37.2	38.6	32.6	30.0	27.4	25.8	24.6	24.2	25.1	24.5	25.1
0.20		ETA	1.00	1.00	1.00	0.49	0.40	0.37	0.32	0.28	0.26	0.24	0.22	0.20	0.19	0.18
9.7	20.7	NU	9.8	9.4	9.2	11.0	22.2	20.5	20.3	20.2	20.4	21.3	22.1	24.4	24.6	26.4
0.47		ETA	1.00	1.00	1.00	0.99	0.78	0.74	0.69	0.63	0.60	0.56	0.51	0.47	0.44	0.40
10.3	22.5	NU	17.9	17.0	17.1	17.7	16.9	17.5	18.5	20.3	22.5	24.7	26.5	29.9	30.5	33.6
1.00		ETA	1.00	1.00	1.00	0.98	0.96	0.96	0.95	0.93	0.90	0.87	0.83	0.78	0.73	0.68

APPENDIX E

TABULAR DATA: NONUNIFORM ARRAY TESTS

The following is a presentation in tabular form of the experimental results for the nonuniform array tests. The flow distribution and pressure profile data are given in Table E.1 (pp. 163 - 166). The Nusselt (or Stanton) number profiles are given in Table E.2 (pp. 167 - 170). The meanings of the notations used in these tables are explained in Appendix D (p. 136).

TABLE E.1 FLOW DISTRIBUTIONS AND PRESSURE PROFILES
(pp. 164 - 166)

TEST#	$\overline{REJ}$(K)	X/L	0.05	0.15	0.25	0.35	0.45	0.55	0.65	0.75	0.85	0.95	T0 (K)	P0 (KPA)	M.C.
			B(10,8,3)I →								B(5,8,3)I				
		P/P0	0.86	****	0.86	****	0.86	****	0.86	****	0.86	0.86			
1X	20.6	GJ/$\overline{GJ}$	1.00	****	1.00	****	1.00	****	0.99	****	1.00	1.00	300.	114.	1.01
		GC/GJ	0.0	****	0.03	****	0.07	****	0.10	****	0.13	0.16			

TEST#	$\overline{REJ}$(K)	X/L	0.05	0.15	0.25	0.35	0.45	0.55	0.65	0.75	0.85	0.95	T0 (K)	P0 (KPA)	M.C.
			B(5,8,3)I ——→									B(5,4,3)I			
		P/P0	0.92	0.92	0.92	0.92	0.92	0.92	0.92	0.91	0.91	0.91			
2Y	16.4	GJ/$\overline{GJ}$	0.97	0.98	0.98	0.98	0.99	1.00	1.00	1.01	1.02	1.03	306.	108.	0.99
		GC/GJ	0.0	0.03	0.06	0.10	0.13	0.16	0.19	0.22	0.25	0.31			
			B(5,4,3)I ——→				←——					B(5,8,3)I			
		P/P0	0.94	0.94	0.94	0.94	0.94	0.93	0.93	0.93	0.93	0.92			
3Y	14.6	GJ/$\overline{GJ}$	0.96	0.97	0.97	0.98	1.00	1.02	1.03	1.04	1.06	1.08	301.	105.	0.99
		GC/GJ	0.0	0.06	0.13	0.19	0.25	0.28	0.31	0.34	0.37	0.39			
			B(5,8,3)I ←——									B(5,4,3)I			
		P/P0	0.97	0.97	0.97	0.97	0.97	0.96	0.96	0.96	0.95	0.95			
4Y	11.3	GJ/$\overline{GJ}$	0.93	0.93	0.93	0.94	0.96	0.98	1.01	1.04	1.09	1.13	301.	103.	0.97
		GC/GJ	0.0	0.03	0.06	0.13	0.19	0.25	0.31	0.36	0.41	0.46			
			B(5,4,3)I ←——									B(5,8,3)I			
		P/P0	0.90	0.90	0.90	0.90	0.90	0.90	0.90	0.89	0.89	0.89			
5Y	17.8	GJ/$\overline{GJ}$	0.98	0.98	0.98	0.99	0.99	1.00	1.00	1.02	1.03	1.05	306.	109.	1.01
		GC/GJ	0.0	0.06	0.10	0.13	0.16	0.19	0.23	0.25	0.28	0.31			

TEST#	$\overline{REJ1}$(K) $\overline{REJ2}$(K)	X/L	0.05	0.15	0.25	0.35	0.45	0.55	0.65	0.75	0.85	0.95	T0 (K)	P0 (KPA)	M.C.
			B(10,8,2)I →					← B(5,4,1)I							
1D	6.9	P/P0	0.96	0.96	0.95	0.95	0.95	0.94	0.94	0.92	0.87	0.81			
	21.9														
		GJ/$\overline{GJ}$	0.67	0.68	0.68	0.69	0.70	0.84	0.88	1.02	1.22	1.44	295.	133.	1.01
		GC/GJ	0.0	0.05	0.10	0.14	0.19	0.20	0.38	0.50	0.58	0.66			
			B(5,4,1)I →					← B(10,8,2)I							
2D	13.5	P/P0	0.97	0.97	0.96	0.95	0.93	0.91	0.90	0.88	0.86	0.84			
	9.6														
		GJ/$\overline{GJ}$	0.76	0.80	0.87	1.00	1.18	1.16	1.24	1.31	1.39	1.47	296.	117.	1.00
		GC/GJ	0.0	0.19	0.35	0.48	0.57	0.78	0.78	0.78	0.78	0.79			

TABLE E.2 HEAT TRANSFER DATA (pp. 168 - 170)

TEST#	$\overline{REJ}$(K)	$\overline{NU}$	X/L	0.05	0.15	0.25	0.35	0.45	0.55	0.65	0.75	0.85	0.95	T0 (K)	P0 (KPA)
				B(10,8,3)I ⟶								B(5,8,3)I			
1X	20.1	56.8	NU	74.3	38.5	69.7	37.0	72.0	36.1	70.0	35.8	68.4	65.9	303.	103.

TEST#	$\overline{REJ}$(K)	$\overline{NU}$	X/L	0.05	0.15	0.25	0.35	0.45	0.55	0.65	0.75	0.85	0.95	T0 (K)	P0 (KPA)
				B(5,8,3)I									B(5,4,3)I		
2Y	16.0	54.4	NU	59.4	56.1	55.2	55.3	56.2	54.4	51.9	52.1	50.9	54.4	311.	108.
				B(5,4,3)I									B(5,8,3)I		
3Y	13.9	52.1	NU	66.4	62.6	61.2	57.1	48.3	45.1	43.9	45.2	45.9	44.9	311.	105.
				B(5,8,3)I									B(5,4,3)I		
4Y	10.7	42.1	NU	43.1	40.2	47.4	47.7	45.5	40.7	39.9	38.8	39.0	38.9	313.	102.
				B(5,4,3)I									B(5,8,3)I		
5Y	17.2	58.7	NU	77.0	62.0	58.8	58.4	59.6	55.8	54.8	55.0	53.5	52.1	312.	109.
				B(10,8,3)I									B(10,4,3)I		
6Y	16.8	40.5	NU	45.7	43.3	42.2	42.5	42.0	39.3	37.0	36.5	38.7	37.5	296.	148.
				B(5,8,2)I									B(5,4,2)I		
7Y	16.6	54.0	NU	59.1	56.8	55.1	55.0	53.5	51.2	49.8	49.3	51.0	59.2	295.	108.
				B(10,8,2)I									B(10,4,2)I		
8Y	16.8	40.3	NU	45.2	42.9	41.6	41.0	40.1	38.0	36.3	36.1	40.4	40.9	296.	152.
				B(10,8,2)I									B(10,4,2)I		
9Y	13.5	35.8	NU	37.8	35.6	34.6	34.0	33.1	36.3	36.1	36.3	36.7	37.1	295.	138.

TEST#	$\overline{REJ1}$(K) $\overline{REJ2}$(K)	$\overline{ST}*10^3$	X/L	0.05	0.15	0.25	0.35	0.45	0.55	0.65	0.75	0.85	0.95	T0 (K)	P0 (KPA)
				B(10,8,2)I ←					→				B(5,4,1)I		
1D	4.4	4.68	ST	4.15	3.78	3.67	3.59	3.46	4.84	4.97	5.53	5.88	6.91	296.	113.
	13.9														
	6.8	4.15	ST	3.62	3.40	3.31	3.28	3.20	4.47	4.37	4.70	5.26	5.86	296.	132.
	21.6														
				B(5,4,1)I ←					→				B(10,8,2)I		
2D	6.6	6.44	ST	7.28	6.43	6.17	6.77	7.50	6.77	5.74	5.74	5.89	6.09	296.	102.
	4.7														
	13.1	5.30	ST	6.06	5.51	4.96	5.43	6.03	5.53	4.74	4.78	4.88	5.08	296.	116.
	9.3														
				D(15,6,3)I ←					→				D(10,4,2)I		
3D	6.2	3.92	ST	3.88	3.71	3.55	3.57	3.26	4.15	4.21	4.08	4.25	4.58	296.	99.
	10.7														
	15.7	3.08	ST	3.02	3.00	2.84	2.89	2.65	3.29	3.25	3.12	3.22	3.50	294.	116.
	27.0														
				D(10,4,2)I ←					→				D(15,6,3)I		
4D	9.6	4.14	ST	5.29	4.92	4.76	4.53	4.47	3.58	3.42	3.40	3.44	3.60	296.	99.
	7.6														
	24.6	3.25	ST	4.02	3.83	3.74	3.64	3.44	2.78	2.70	2.70	2.78	2.88	294.	112.
	19.4														

1. Report No.	2. Government Accession No.	3. Recipient's Catalog No.
NASA CR-3630		

4. Title and Subtitle	5. Report Date
JET ARRAY IMPINGEMENT FLOW DISTRIBUTIONS AND HEAT TRANSFER CHARACTERISTICS - EFFECTS OF INITIAL CROSSFLOW AND NONUNIFORM ARRAY GEOMETRY	November 1982
	6. Performing Organization Code
7. Author(s) L. W. Florschuetz, D. E. Metzger, C. C. Su, Y. Isoda, and H. H. Tseng	8. Performing Organization Report No. ERC-R-82038
	10. Work Unit No.
9. Performing Organization Name and Address Arizona State University Dept. of Mechanical and Aerospace Engineering Tempe, Arizona 85287	11. Contract or Grant No. NSG-3075
	13. Type of Report and Period Covered Contractor Report
12. Sponsoring Agency Name and Address National Aeronautics and Space Administration Washington, D. C. 20546	14. Sponsoring Agency Code 510-57-12 (E-1385)

15. Supplementary Notes

Final report. Project Manager, Steven A. Hippensteele, Aerothermodynamics and Fuels Division, NASA Lewis Research Center, Cleveland, Ohio 44135.

16. Abstract

Two-dimensional arrays of circular air jets impinging on a heat transfer surface parallel to the jet orifice plate are considered. The jet flow, after impingement, is constrained to exit in a single direction along the channel formed by the jet orifice plate and the heat transfer surface. The configurations considered are intended to model those of interest in current and contemplated gas turbine airfoil midchord cooling applications. In Part I, the effects of an initial crossflow which approaches the array through an upstream extension of the channel are considered. Flow distributions as well as heat transfer coefficients and adiabatic wall temperatures resolved to one streamwise hole spacing were measured as a function of the initial crossflow rate and temperature relative to the jet flow rate and temperature. Both Nusselt number profiles and dimensionless adiabatic wall temperature ("effectiveness") profiles are presented and discussed. Special test results which show a significant reduction of jet orifice discharge coefficients owing to the effect of a confined crossflow are also presented, along with a flow distribution model which incorporates those effects. In Part II, a nonuniform array flow distribution model is developed and validated. It is then employed to compare newly obtained nonuniform array streamwise resolved heat transfer coefficient data with previously reported uniform array data (NASA CR-3217) and with the previously developed correlation (NASA CR-3373) based on the uniform array data. It was found that the uniform array results can, in general, serve as a satisfactory basis from which to determine heat transfer coefficients at individual rows of nonuniform arrays.

17. Key Words (Suggested by Author(s))	18. Distribution Statement
Jet impingement; Jet array; Heat transfer; Gas turbine; Crossflow; Initial crossflow; Impingement cooling; Flow distribution; Discharge coefficient	Unclassified - unlimited STAR Category 34

19. Security Classif. (of this report)	20. Security Classif. (of this page)	21. No. of Pages	22. Price*
Unclassified	Unclassified	177	A09

* For sale by the National Technical Information Service, Springfield, Virginia 22161

NASA-Langley, 1982